刚性折纸以及球面机构网格

Rigid Origami and Networks of Spherical Mechanisms

一级学科：机械工程
学科专业：机械工程
作者姓名：吕玮琳
指导教师：陈焱　　　　　　教授

天津大学机械工程学院
二〇二一年三月

摘要

刚性折纸可被视为球面机构的装配体，其被广泛应用于工程领域。本文系统地探讨了基于球面机构构建一维、二维、及三维可动网格的方法，通过分析球面机构网格的运动协调条件，设计了可切换手性以及具有层级手性的螺旋结构，研究了基于球面机构的可变形曲面，并且提出了一类新的刚性折纸管状结构以及折纸管状结构的厚板折叠方案。本文的主要研究内容如下：

首先，受刚性折纸图案的启发，设计了一种由球面四杆机构构成的一维螺旋结构。基于 eggbox 折纸图案得到了两种手性折叠单元，通过串联上述折叠单元可以得到不同的手性结构，并且发现通过调节手性折叠单元的几何参数可以调整上述手性结构的手性。进一步的研究表明，通过机构分岔原理可以实现该结构的左-右手的手性转换。此外，通过球面四杆机构连接上述手性折叠单元，得到了一种手性可以从构成单元层次向整体结构层次传递的层级螺旋结构，该结构在解螺旋运动过程中具有两个零长度状态。

其次，研究了基于刚性折纸图案的平面可动网格。提出了一种由球面四杆机构构成的二维单自由度网格系统，在该网格系统中，通过使用四面体来代替 eggbox 折纸图案中的平面单元。并且通过引入球面六杆和八杆机构，该网格结构可被扩展成一个可变形曲面，通过采用适合的设计参数，其可以在两个不同的目标曲面之间进行变形。

再次，提出了一类新的三维刚性折纸管状结构。受 Goldberg 五杆和六杆机构的启发，发现已有的管状结构可以作为构建模块，组成新的单自由度刚性折纸管状结构。通过将已有管状结构进行组合以及向已有的管状结构中加入新的平面单元的方式，得到了两种新的折纸管状结构。该方法可以应用于不同的直管或弯管的单层以及多层结构中。

最后，为了实现零厚度折纸管状结构的实际工程应用，提出了一种构造厚板折纸管状结构的方法。通过将零厚度刚性折纸管状结构中的球面四杆机构替换为 Bennett 机构和 Bricard 机构，获得了厚板折纸管状结构，其能够实现与零厚度折纸管状结构等效的运动。

本文的研究为折纸结构、机器人以及超材料的设计提供了理论基础。

关键词：球面四杆机构，可展结构，刚性折纸，厚板折纸

ABSTRACT

Rigid origami, which can be regarded as assembly of spherical linkages, are widely used in space technologies, architecture and metamaterials. In this thesis, the possibilities of constructing mobile networks based on spherical linkages are explored, 1D and 2D mobile networks based on rigid origami are analyzed, the family of origami tubes is enlarged and a method to construct thick-panel origami tubes is proposed.

First, an 1D open-loop helical structure of spherical 4*R* linkages is obtained, inspired by a rigid origami pattern. Eggbox-based chiral units are developed to construct homogeneous and heterogeneous chiral structures and demonstrate a theoretical approach to tune the chirality of these structures by modulating their geometrical parameters to realize the chirality switching through a mechanism bifurcation. Furthermore, by introducing a helical tessellation between the chiral units, hierarchical helical structures with a chirality transfer from the construction elements to the morphological level are designed and a novel helix with two zero-height configurations during the unwinding process is presented.

Next, the 2D planar mobile networks based on rigid origami patterns are explored. A one-DOF network system of spherical 4*R* linkages is developed by replacing the unit facets of the planar eggbox pattern with volumetric tetrahedrons. The 4*R* configuration can be expanded to an arbitrary surface profile by inserting 6*R* and 8*R* linkages in the original network system. The above-mentioned surface is known as a morphing surface, and it can transform between two target surfaces through the implementation of suitable design parameters.

Subsequently, an extended family of rigid origami tubes is presented. Using a mechanism construction process, I demonstrate that the existing origami tubes can be used as building blocks to form new tubes that are rigidly foldable with a single degree-of-freedom. A combination process is introduced, along with the option of inserting new facets in an existing tube. The approach can be applied to both single and multi-layered tubes with a straight or curved profile.

Finally, a method of constructing thick-panel origami tubes is proposed. Origami patterns are commonly created using a zero-thickness sheet; however, the panel thickness cannot be disregarded in real engineering applications. By replacing the spherical 4*R* linkages in the original rigid origami tube with overconstrained linkages such as Bennett and Bricard linkages, origami tubes of thick panels are obtained, which can be used to reproduce kinematic motions equivalent to those realized using zero-thickness origami.

This thesis provides theoretical basis for origami structures, robots and metamaterials.

KEYWORDS: Spherical 4*R* linkage, Deployable structures, Rigid origami, Thick-panel origami

Contents

List of Figures

List of Tables

Notation

Parameters

x_i, y_i, z_i	x, y, z coordinate axis of system i
$a_{i(i+1)}$	Link length $i(i+1)$
$\alpha_{i(i+1)}$	Twist from z_i to z_{i+1}, positively about axis x_{i+1}
θ_i	Joint angle from the x_{i-1}-axis to the x_i-axis, positively about z_i-axis
R_i	Offset of joint i
$\boldsymbol{T}_{(i+1)i}$	4×4 transformation matrix from the ith coordinate system to the $(i+1)$th coordinate system
$\boldsymbol{Q}_{(i+1)i}$	3×3 rotation matrix from the ith coordinate system to the $(i+1)$th coordinate system
$\boldsymbol{I}_i$	$i\times i$ identity matrix
$\varepsilon_{m(m+1)}$	Rotation from intersection plane m to $(m+1)$ in an origami tube
d_i	Number of DOFs for the ith kinematic pair
j	Number of kinematic pairs in a linkage
m	Number of DOFs in a linkage
k	Number of links in a linkage
A, B, C, D, E F, G, H, I, J, K L, M, N, O, P	Origami vertexes and their corresponding spherical linkages; vertexes in morphing surfaces and their corresponding spherical linkages
γ_1	Angle between crease lines OA and OC in chiral units
γ	Angle between the two horizontal alternative creases in chiral units
h	Distance between the bottom and top faces in chiral units
ϕ	Dihedral angle between the two lower facets connecting two eggboxes in RH or LH chiral units
p	Pitch of the helix in a chiral structure
κ	Helical angle of the helix in a chiral structure
r	Radius of the minor helix
F_i	Coordinate frame of the ith unit of a hierarchically chiral structure
f_{ij}	jth frame in the ith unit of a hierarchically chiral structure
K	Helical angle of the major helix
P	Pitch of the major helix
R	Radius of the major helix

L	Length of the major helix
Γ	Twist angle of a chiral structure
H	Height of a chiral structure
N	Number of units in a chiral structure
ΔH	Displacement in the tensile experiment
$\Delta\Gamma$	Structural twist angle increment in the tensile experiment
$\boldsymbol{D}_z(s)$	Translation along axis z with a distance of s
O_i	Points in the major helix
$\mathbf{p}_{i,i}$	Position vector of point O_i in frame F_i
$\boldsymbol{T}$	Transformation matrix that transforms the expression in frame F_{i+1} to F_i
$\mathbf{B}_i\mathbf{O}_i$, $\mathbf{A}_i\mathbf{B}_i$, $\mathbf{A}_i\mathbf{O}_i$, $\mathbf{O}_i\mathbf{D}_i$, $\mathbf{D}_i\mathbf{O}_i$, $\mathbf{E}_i\mathbf{A}_i$, $\mathbf{A}_i\mathbf{E}_i$, $\mathbf{E}_i\mathbf{B}_{i+1}$, $\mathbf{B}_{i+1}\mathbf{E}_i$, $\mathbf{E}_i\mathbf{C}_{i+1}$, $\mathbf{E}_i\mathbf{B}_{i+1}$	Vectors in the ith and (i+1)th units of a hierarchically chiral structure
$\mathbf{s}$	Normalized direction vector of the helical axis in the major helix
$\mathbf{s}(i,1)$	Element of vector $\mathbf{s}$ in the ith row
l	Distance between O_i and O_{i+1}
$\alpha_{i(i+1)}^{\mathrm{X}}$	Sector angle at an arbitrary vertex X or twist angle in an arbitrary spherical linkage X in the morphing surface.
θ_i^{X}	Joint angle in an arbitrary spherical linkage X in morphing surfaces
$\mathbf{a}_i^{\mathrm{X}}$	Direction vector of the ith crease line at an arbitrary vertex X
$\mathbf{n}_i^{\mathrm{X}}$	Direction vector of $\mathbf{a}_i^{\mathrm{X}} \times \mathbf{a}_{i+1}^{\mathrm{X}}$
$\mathbf{p}_{\mathrm{X}}$	The coordinates of vertex X
H_1 to H_4	Vertexes in the H-line
V_1 to V_4	Vertexes in the V-line
ε	Accuracy error in morphing surfaces
α^{T1}, β^{T1}, γ^{T1}, δ^{T1}	Sector angles in Tube 1
α^{T2}, β^{T2}, γ^{T2}, δ^{T2}	Sector angles in Tube 2
γ_i	Sector angles in facets T1 in a shifted tube
η_L, η_R	Dihedral angels between facets in a curved shifted tube.
T1	Adding part in a shifted tube
P1, P2	Two parts of the original tube in a shifted tube
θ_1^{T1}, θ_3^{T1}	Joint angles in Tube 1
θ_1^{T2}, θ_3^{T2}	Joint angles in Tube 2

$\varepsilon^{\mathrm{T1}}, \nu^{\mathrm{T1}}$	Rotation between two intersection plane in Tube 1
$\varepsilon^{\mathrm{T2}}, \nu^{\mathrm{T2}}$	Rotation between two intersection plane in Tube 2
$\alpha_{i(i+1)}^{Be}$	Twist angles in a Bennett linkage
ω_i^{Be}	Dihedral angles between links in a Bennett linkage
$\alpha_{i(i+1)}^{Br}$	Twist angles in a Bricard linkage
ω_i^{Br}	Dihedral angles between links in a Bricard linkage

Symbolic Variables

$\alpha, \beta, \gamma, \delta, \alpha_i$	Value of the twists in linkages or sector angles in origami patterns
a, b	Value of link lengths or edge lengths
R	Value of offset in Chapter 5
ω_i,	Value of dihedral angle between facets (i-1) and i in an origami pattern or a morphing surface.
θ	Value of winding angle of the helix in chiral structures in Chapter 2; value of joint angles in Chapter 4
θ_{s}	Value of winding angle of the minor helix
θ_{m}	Value of winding angle of the major helix
ρ_1, ρ_2	Value of two dihedral angles in the connection part between two units of a hierarchically chiral structure
L	Length of the sides of triangle units in Chapter 3

Abbreviations

Be	Bennett linkage
Br	Plane-symmetric Bricard linkage
D-H notation	Denavit-Hartenberg notation
DOF	Degree of freedom
RH	Right-handed
LH	Left-handed

Chapter 1 Introduction

1.1 Background and Significance

Deployable structures are mobile assemblies aimed not at realizing motion but at attaining different configurations depending on the service requirements [1]. Specifically, such structures have a compact form in modes such as transportation or storage but can be expanded for final use. These structures are mainly used either for transportation purposes or in applications in which adaptability of the shape or function is necessary. In particular, deployable structures are widely used in space technologies, such as solar arrays and antennas on spacecraft [2, 3]. Moreover, deployable structures are used to develop temporary residences [4, 5], stents and metamaterials to absorb energy [6, 7]. Thus, such structures are of interest to architectural engineers, mechanical scientists and other researchers in different fields.

Deployable structures must exhibit a large deploy-fold ratio and complex shapes to achievement higher functionalities. Spherical linkages and overconstrained spatial linkages can be used to construct deployable structures, although the compatible conditions of tilling these linkages to constitute large mobile structures must be examined.

A spherical linkage is a kinematic closed-loop of revolute joints whose axes must intersect at a single point [8]. Spherical linkages are widely used in the automobile industry, for instance, in developing universal and double universal joints. However, the compatible conditions of networks based on spherical linkages are complex because they represent overconstrained systems.

Based on rigid origami techniques, the conceptual design of spherical linkages can be reliably realized using folding origami. Origami is the traditional art of paper folding, and rigid origami represents a unique form of origami in which the surfaces surrounded by the crease lines are not stretched or bent during folding. Each facet of the structure is rigid and rotates only around the crease. Considering the characteristics of rigid origami, such structures can be analysed using a kinematic approach in which the facets and crease lines can be replaced by rigid panels and hinges. Hence, rigid origami patterns represent networks of spherical linkages.

1.2 Literature Review

1.2.1 Kinematic theories

The science of kinematics pertains to the geometric and time properties of motion [9]. Chiang analysed spherical mechanisms [10]. Moreover, methods to analyse the kinematics of spatial linkages have been presented. Gogu systematically described the structural synthesis of various spatial parallel mechanisms based on the theory of linear transformation [11]. Dai comprehensively presented the kinematics of various mechanisms based on the screw theory [12], which was proposed by Ball [13] and developed by Hunt [14].

The mechanisms discussed in this thesis are formed by a set of rigid parts assembled end to end to form a single closed chain. This single closed chain is known as a linkage, each individual rigid part of this structure is known as a link and the connection of two adjacent links is a joint, which can be spherical, planar, cylindrical, screw, revolute or prismatic. In this work, I focus on the mechanisms involving only revolute joints, which allow only one-DOF rotation about their axes.

Denavit and Hartenberg developed an approach to normalize the kinematic study of mechanisms by using a symbolic language known as D-H notation [15]. Figure 1-1 shows the coordinate system in a linkage. The z_i-axis (i = 1, 2, 3 and 4) lies along the joint axis of joint i; the x_i-axis is normal to the plane formed by the z_{i-1} and z_i axes, such that $x_i = z_{i-1} \times z_i$; the y_i-axis can be determined using the right-hand rule. $a_{i(i+1)}$ is the shortest distance between the z_i and z_{i+1} axes, also referred to as the link length $i(i+1)$. R_i is the distance from link $(i-1)i$ to link $i(i+1)$ positively along the z_i-axis, referred to as the offset of joint i. The kinematic variable angle θ_i is defined as the joint angle from the x_i-axis to the x_{i+1}-axis, positively about the z_i-axis; and the twist $\alpha_{i(i+1)}$ refers to the twist angle from z_i to z_{i+1}, positively about axis x_i.

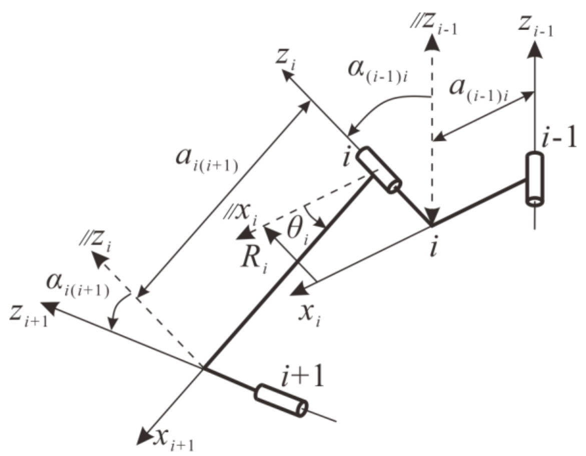

Fig. 1-1 Coordinate systems, parameters and variables for two adjacent links connected by revolute joints.

Based on these definitions and the D-H convention, the transformation matrix $\boldsymbol{T}_{(i+1)i}$ that transforms an expression in the $(i+1)$th coordinate system to the ith coordinate system can be expressed as

$$\boldsymbol{T}_{(i+1)i}=\begin{bmatrix}\cos\theta_i & -\sin\theta_i\cos\alpha_{i(i+1)} & \sin\theta_i\sin\alpha_{i(i+1)} & a_{i(i+1)}\cos\theta_i\\ \sin\theta_i & \cos\theta_i\cos\alpha_{i(i+1)} & -\cos\theta_i\sin\alpha_{i(i+1)} & a_{i(i+1)}\sin\theta_i\\ 0 & \sin\alpha_{i(i+1)} & \cos\alpha_{i(i+1)} & R_i\\ 0 & 0 & 0 & 1\end{bmatrix}. \tag{1-1}$$

The necessary condition for a single-loop linkage of *n* links is that the successive product of the transformation matrices must be preserved as a unit matrix, i.e.,

$$\boldsymbol{T}_{21}\boldsymbol{T}_{32}\cdots\boldsymbol{T}_{1n}=\boldsymbol{I}_4, \tag{1-2}$$

in which $\boldsymbol{I}_4$ is a 4×4 unit matrix.

The inverse transformation $\boldsymbol{T}_{i(i+1)}$ has the following property.

$$\boldsymbol{T}_{i(i+1)}=\boldsymbol{T}^{-1}{}_{(i+1)i}=\begin{bmatrix}\cos\theta_i & \sin\theta_i & 0 & -a_{i(i+1)}\\ -\sin\theta_i\cos\alpha_{i(i+1)} & \cos\theta_i\cos\alpha_{i(i+1)} & \sin\alpha_{i(i+1)} & -\sin\alpha_{i(i+1)}R_i\\ \sin\theta_i\sin\alpha_{i(i+1)} & -\cos\theta_i\sin\alpha_{i(i+1)} & \cos\alpha_{i(i+1)} & -\cos\alpha_{i(i+1)}R_i\\ 0 & 0 & 0 & 1\end{bmatrix}. \tag{1-3}$$

For spherical linkages, the axes intersect at one point, as shown in Fig. 1-2, owing to which, the lengths and offsets of each link are zero, and Eqn. (2-1) reduces to

$$\boldsymbol{Q}_{21}\boldsymbol{Q}_{32}\cdots\boldsymbol{Q}_{1n}=\boldsymbol{I}_3, \tag{1-4}$$

where

$$\boldsymbol{Q}_{(i+1)i}=\begin{bmatrix}\cos\theta_i & -\sin\theta_i\cos\alpha_{i(i+1)} & \sin\theta_i\sin\alpha_{i(i+1)}\\ \sin\theta_i & \cos\theta_i\cos\alpha_{i(i+1)} & -\cos\theta_i\sin\alpha_{i(i+1)}\\ 0 & \sin\alpha_{i(i+1)} & \cos\alpha_{i(i+1)}\end{bmatrix}, \tag{1-5}$$

and the inverse transformation is

$$\boldsymbol{Q}_{i(i+1)}=\boldsymbol{Q}^{-1}{}_{(i+1)i}=\begin{bmatrix}\cos\theta_i & \sin\theta_i & 0\\ -\sin\theta_i\cos\alpha_{i(i+1)} & \cos\theta_i\cos\alpha_{i(i+1)} & \sin\alpha_{i(i+1)}\\ \sin\theta_i\sin\alpha_{i(i+1)} & -\cos\theta_i\sin\alpha_{i(i+1)} & \cos\alpha_{i(i+1)}\end{bmatrix}. \tag{1-6}$$

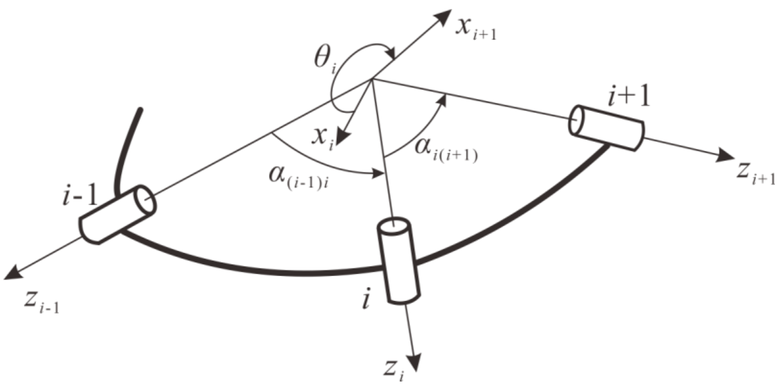

Fig. 1-2 D-H notation of a part of a spherical linkage.

Therefore, the kinematics and motion behaviour of spatial and spherical linkages can be analysed based on the solutions of Eqn. (1-2) or Eqn. (1-4).

The Lie algebra of a Lie group plays a key role in modern physics, with the Lie group typically representing the symmetry of a physical system [16]. Murray et al. used the Lie group theory to analyse the kinematics of robotic manipulators [17]. Hervé proposed the Lie group method to derive the motion of a parallel platform and provided detailed examples of 3-DOF robotic manipulators [18].

The Bond theory was proposed as a mathematical technique to study the mobility of linkages by Hegedüs et al. [19-23]. Based on this theory, the authors analysed the kinematics of closed 5*R* [19] and 6*R* linkages [23].

1.2.2 Spherical linkages

As in planar kinematics, in which a link is characterized by the length between the joints, in spherical kinematics, a link is characterized by the great circle arc subtended by two joints at the sphere centre [24]. Spherical linkages are widely used in robotic arms [25, 26]. Many researchers have examined spherical linkages. The kinematics of spherical 4*R* linkages were analysed by Chiang through a mathematical approach [24]. Ruth and McCarthy proposed a computer-aided design software system for spherical 4*R* linkages [27] based on Burmester's planar theory [28]. McCarthy and Bodduluri extended the generalization of the planar rectification theory to spherical 4*R* linkages and presented a method to ensure that the result of a finite position synthesis was a linkage that did not exhibit a 'branching problem' [29]. Soh and McCarthy developed a procedure in which two constraining links were added to a three-DOF spherical parallel manipulator to transform the system to a one-DOF spherical 8-bar linkage that could guide the end-effector through five task poses [30], as illustrated in Fig. 1-3. Wei and Dai presented two integrated planar-spherical overconstrained mechanisms based on spherical linkages [31] and recently, Liu and Chen designed a double-spherical 6*R* linkage with spatial crank-rocker characteristics and derived the corresponding overconstrained geometric conditions and explicit closure equations [32], as shown in Fig. 1-4.

1.2.2.1 Rigid origami

Origami is the traditional art of folding paper into sculptures, with a history of more than one hundred years [33]. The form of origami in which each surface surrounded with the crease lines is not stretched and bent during folding is known as rigid origami [34], and it can be regarded as an assembly of spherical linkages. In origami, there exist two kinds of creases, i.e., mountain and valley creases. The crease pattern refers to a mapping of all the creases in an origami form [35].

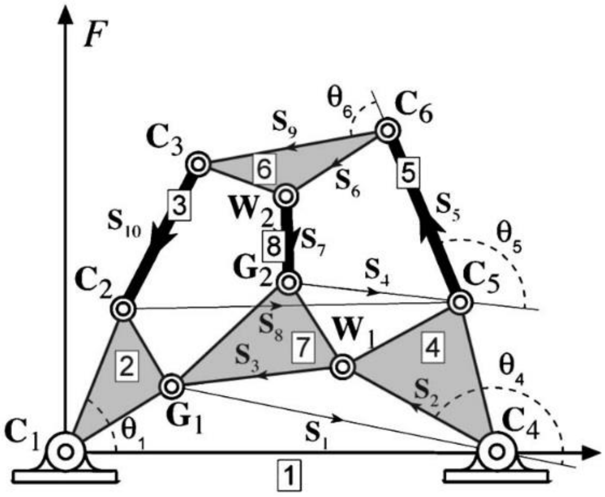

Fig. 1-3 Spherical 8-bar linkage presented by Soh and McCarthy [30].

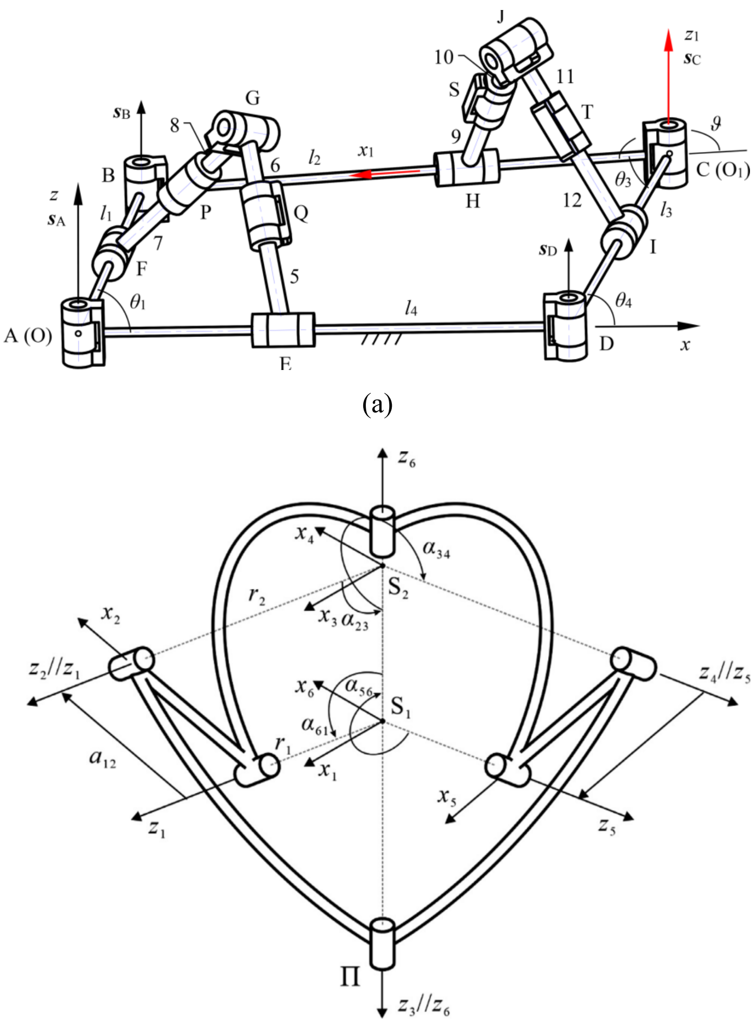

(a)

(b)

Fig. 1-4 Mechanisms based on spherical linkages: (a) integrated planar-spherical overconstrained mechanism [31] and (b) double-spherical 6*R* linkage [32].

Because of the large deployable ratio and low cost, rigid origami patterns can be applied in various applications such as robotic systems [36, 37], deployable arrays for space applications [38], and self-deployment structures [39].

This section reviews the typical rigid origami patterns, with a focus on patterns with degree-4 vertexes. Evans et al. reviewed origami patterns in which the summation of the sector angles at a single vertex equaled 2π [40]. Huffman presented a pattern known as the Huffman grid [41], which can be constructed by a single degree-4 vertex rotated and repeated continuously through the tessellation, as shown in Fig. 1-5(a) in which the solid and dashed lines represent the mountain and valley crease lines, respectively. Another pattern, known as the chicken wire tessellation (also known as the hexagonal pattern [42]) can be constructed using a single vertex with mirror symmetry (see Fig. 1-5(b)). The 'Mars' pattern (see Fig. 1-5(c)), which was presented by Paulo Barreto [43], includes a single degree-4 vertex and its inversion. The famous Miura-ori pattern, presented by Miura [44], is formed entirely of parallelograms, as shown in Fig. 1-5(d). Quadrilateral mesh origami and the associated conditions for rigid foldability were analysed by Tachi [45], and the pattern is shown in Fig. 1-5(e).

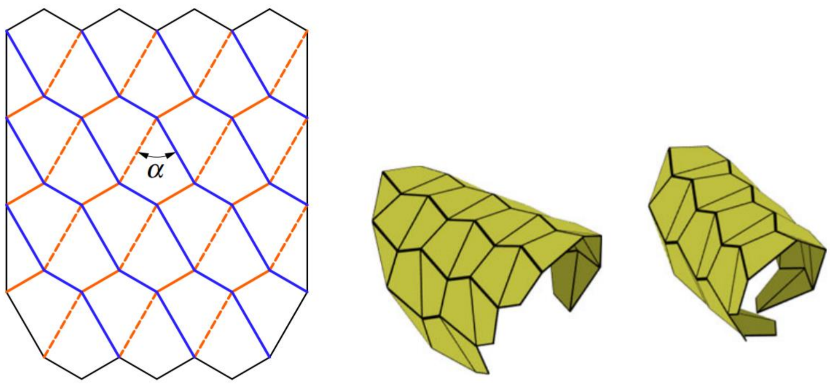

(a)

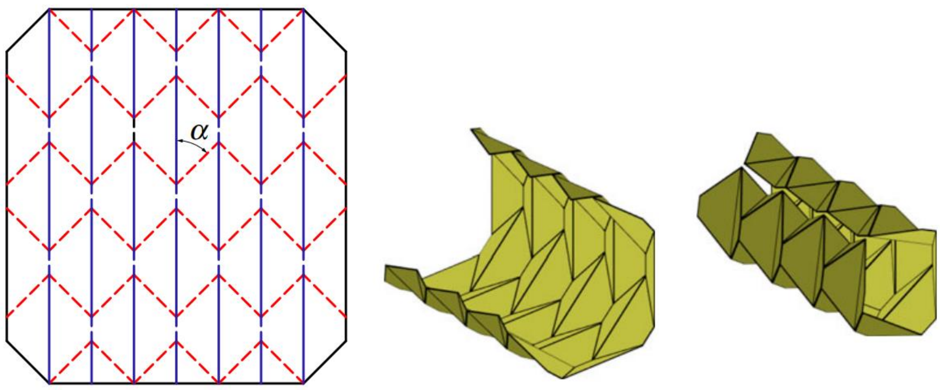

(b)

Fig. 1-5 Origami patterns and folding process of (a) Huffman grid, (b) chicken wire, (c) Mars, (d) Miura-ori and (e) quadrilateral mesh [40].

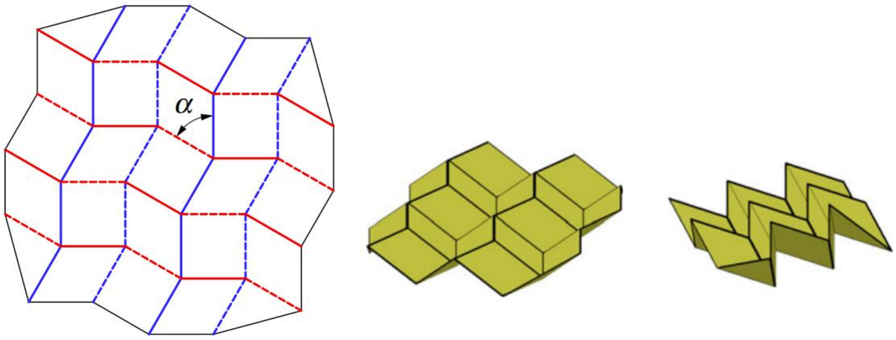

(c)

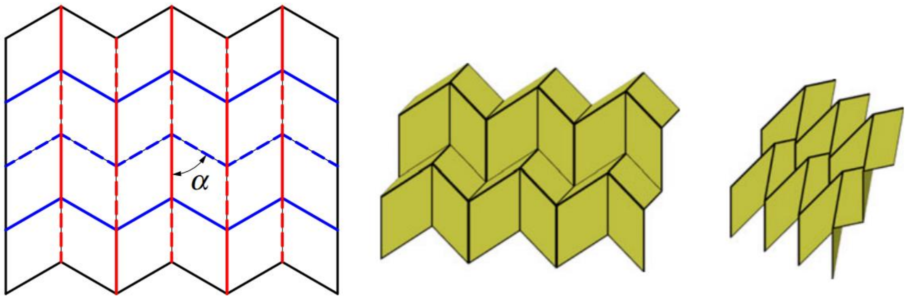

(d)

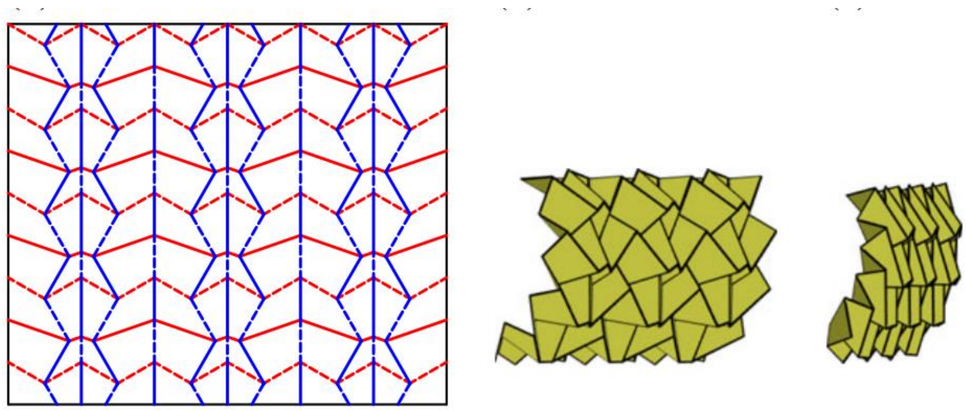

(e)

Fig. 1-5 Origami patterns and folding process of (a) Huffman grid, (b) chicken wire, (c) Mars, (d) Miura-ori and (e) quadrilateral mesh [40]. (continued)

1.2.2.2 Method to investigate rigid origami patterns

For a rigid origami pattern, the rigid foldability is a key property that allows the pattern to fold along the crease lines without twisting or stretching the component panels. To achieve rigid foldability, the motions around each vertex must be compatible with those around the adjacent vertex, and this condition can be attained only under specific pattern geometries. Extensive research has been performed to identify the geometry conditions that render an origami pattern rigid-foldable.

Rigid origami has been researched from the viewpoint of geometry. Miura [46] presented a proposition of the intrinsic geometry of origami based on an arbitrary point on the surface of origami structures. Watanabe and Kawaguchi [33] proposed two methods to evaluate the rigid foldability of origami patters from the compatibility matrix. Based on the separation of each crease of an origami pattern into two parallel creases, Hull and Tachi [47] presented the double line method to obtain new origami patterns. He and Guest [48] studied the configuration space of four-crease origami patterns and generated two families of rigid-foldable origami patterns with four-crease vertexes. Wu and You [49] proposed a new crease pattern that allowed a tall box-shaped bag with a rectangular base to be rigidly folded flat.

Furthermore, rigid origami can be analysed using a kinematic approach, which is a focus in this work. Since the research of Cundy [50], it has been widely acknowledged that for every rigid origami structure, there exists an equivalent linkage [51, 52]. The left part of Fig. 1-6 shows a degree-4 origami vertex containing four panels or sectors 1 to 4, and four creases AO, BO, CO and DO; the four creases intersect at a common point O. The four sector angles between the adjacent creases are α_{12}, α_{23}, α_{34} and α_{41}; and the four dihedral angles between the adjacent sectors are ω_1, ω_2, ω_3 and ω_4. From the mechanism viewpoint, by considering the sectors and creases as links and revolute joints, respectively, an equivalent spherical 4*R* linkage can be obtained, as shown in the right part of Fig. 1-6. In this case, sectors 1 to 4 become links 1 to 4, creases A to D become joints A to D, and sector angels α_{12}, α_{23}, α_{34} and α_{41} become the twist angles of the linkage.

Substituting Eqn. (1-5) in (1-4) yields the general relationship between two adjacent and opposite joint angles

$$\begin{aligned}
&\sin\alpha_{i(i+1)}\cos\alpha_{(i+1)(i+2)}\sin\alpha_{(i+3)(i+4)}\cos\theta_i \\
&+\sin\alpha_{i(i+1)}\sin\alpha_{(i+1)(i+2)}\cos\alpha_{(i+3)(i+4)}\cos\theta_{i+1} \\
&+\cos\alpha_{i(i+1)}\sin\alpha_{(i+1)(i+2)}\sin\alpha_{(i+3)(i+4)}\cos\theta_i\cos\theta_{i+1} \\
&-\sin\alpha_{(i+1)(i+2)}\sin\alpha_{(i+3)(i+4)}\sin\theta_i\sin\theta_{i+1} \\
&-\cos\alpha_{i(i+1)}\cos\alpha_{(i+1)(i+2)}\cos\alpha_{(i+3)(i+4)}+\cos\alpha_{(i+2)(i+3)}=0;
\end{aligned} \tag{1-7a}$$

$$\begin{aligned}
&\cos\alpha_{i(i+1)}\cos\alpha_{(i+3)(i+4)}-\sin\alpha_{i(i+1)}\sin\alpha_{(i+3)(i+4)}\cos\theta_i= \\
&\cos\alpha_{(i+1)(i+2)}\cos\alpha_{(i+2)(i+3)}-\sin\alpha_{(i+1)(i+2)}\sin\alpha_{(i+2)(i+3)}\cos\theta_{i+2};
\end{aligned} \tag{1-7b}$$

in which i=1, 2, 3 and 4; if $i+j$>4, the term is replaced by ($i+j$-4).

The typical origami crease patterns and their corresponding equivalent closed-loop linkage were investigated by Zhang and Dai [53]. Wei and Dai [54] analysed an origami carton by representing it with one planar four-bar loop and two spherical 4*R* linkage loops. Using the tessellation method for the mobile assemblies of spatial linkages [55-57], Wang and Chen [58] developed a mobile assembly of spherical 4*R* linkages to study the Kokotsakis type of rigid origami patterns. Liu [59] used the assemblies of spherical 4R linkages to analyse the rigid origami patterns and presented several new patterns. Recently, Gu and Chen present a new method to design origami cubes with rigid foldability, flat foldability and one-DOF [60].

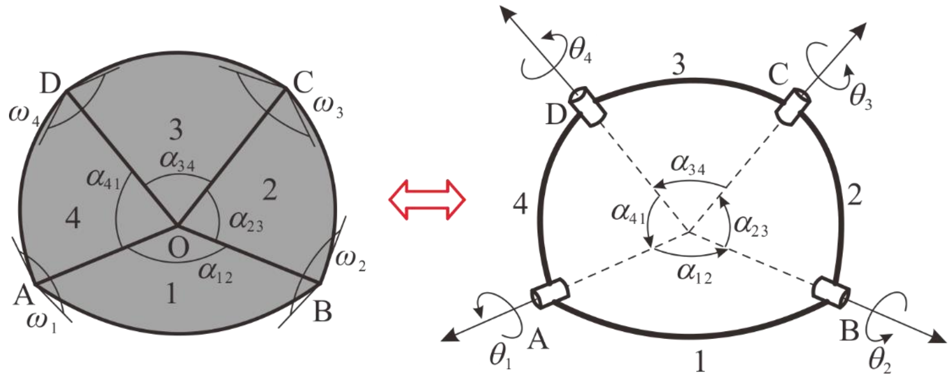

Fig. 1-6 Four-crease origami pattern and its corresponding spherical 4R linkage.

1.2.2.3 Rigid origami tubes

Origami tubes have been used in various applications ranging from medical devices [61] to worm robots [35]. Considerable efforts have been implemented to effectively fold these tubular structures without distorting their surfaces. Guest and Pellegrino [62] proposed a method wherein the cylindrical surface of a tube was dissected into a set of triangular facets to enable packaging. However, the authors proved that such tubes could only be folded if the facets were allowed to deform; in other words, these tubes were not rigidly foldable. Moreover, many patterns for both tubes and cones were devised by Nojima [63, 64], who examined whether the folding patterns could be generated from a flat piece of paper, and the tube could be folded flat eventually. It was later observed that none of the tubes and cones could be rigidly folded longitudinally. It has been proven that a tube with closed ends cannot be folded rigidly without distorting its facets [65].

Consequently, the effort was redirected to tubes with open ends. Using a geometrical method, Tachi [66, 67] devised a set of tubes with parallelogram facets that are rigidly foldable and can be extended longitudinally to form multi-layered tubes by repeating the same foldable unit (Fig. 1-7(a)). In addition, a set of rigidly foldable tubes with parallelogram cross-sections was placed side by side, thereby forming the Tachi-Miura polyhedron bellows [68, 69] (Fig. 1-7(b)).

Liu et al. [70] demonstrated this aspect through a kinematic approach. As shown in Fig. 1-8, to form the deployable prismatic structures, N spherical 4R linkages are assembled as a closed chain. The dihedral angles between the intersections of each layer of the tube are independent, as shown in Fig. 1-9(a). The dihedral angle $\varepsilon_{m(m+1)}$ represents the rotation from the intersection plane m to (m+1), positively in the counterclockwise direction. The two dihedral angles $\varepsilon_{m(m+1)}$ and $\varepsilon_{(m-1)m}$ may be different. Depending on the arrangements of the dihedral angles, curvy tubular structures having various configurations can be achieved, as illustrated in Fig. 1-9(b). The cross-sections of these straight and curvy tubes, defined by a loop of lateral crease lines, are commonly even-sided plane- or line-symmetric polygons, such as a kite or parallelogram.

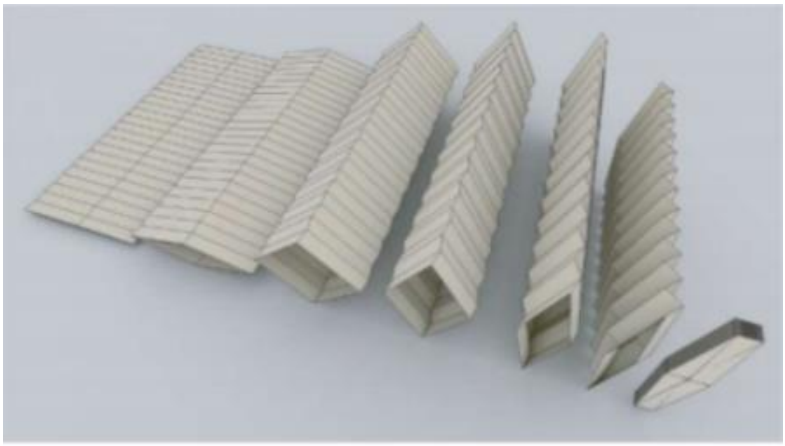

(a)

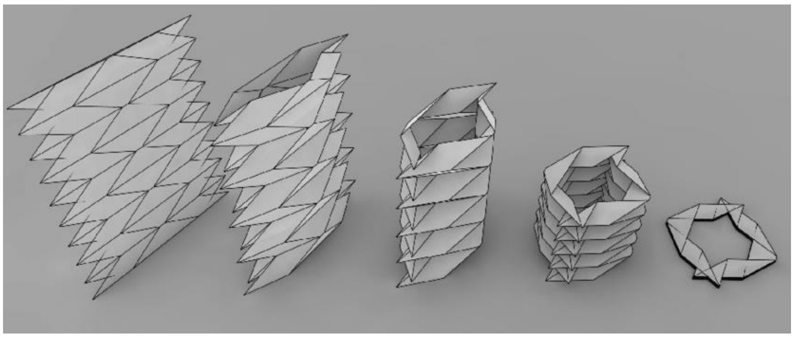

(b)

Fig. 1-7 Rigid origami tubes: (a) A tube of tubes with parallelogram facets [66] and (b) a Tachi-Miura polyhedron bellow [69].

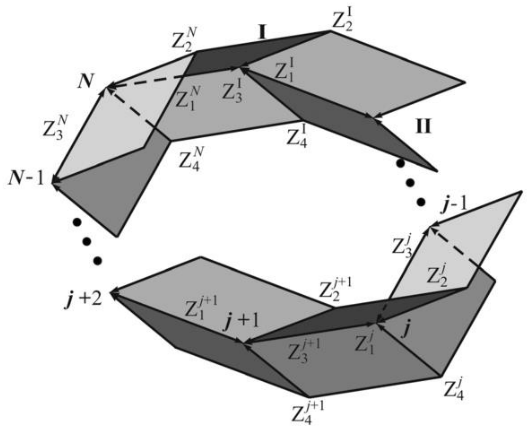

Fig. 1-8 Assembly of spherical 4R linkages in a rigid origami tube [70].

Schenk and Guest [71] investigated the geometry of metamaterial based on a stack of Miura-ori patterns, which can be considered as a unique case of polyhedron bellows. Filipov et al. [72, 73] developed tubes with reconfigurable parallelogram cross-sections, as shown in Fig. 1-10.

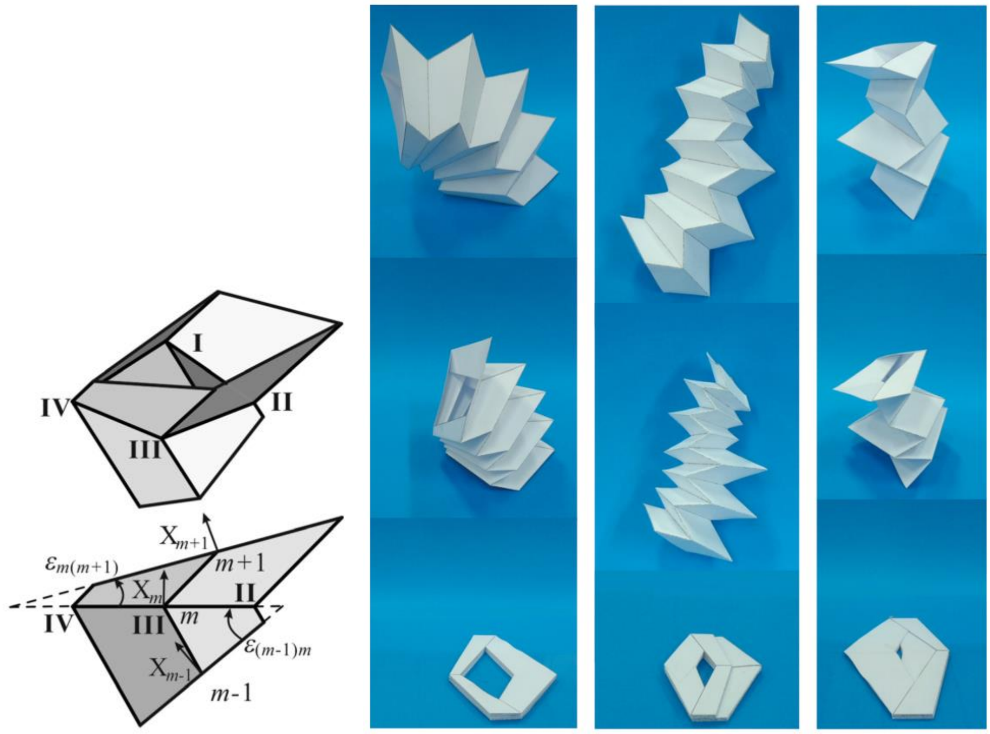

(a) (b)

Fig. 1-9 Curvy tubes [70]: (a) a tube with different dihedral angles between the intersections of each layer and (b) the model of curvy tubes.

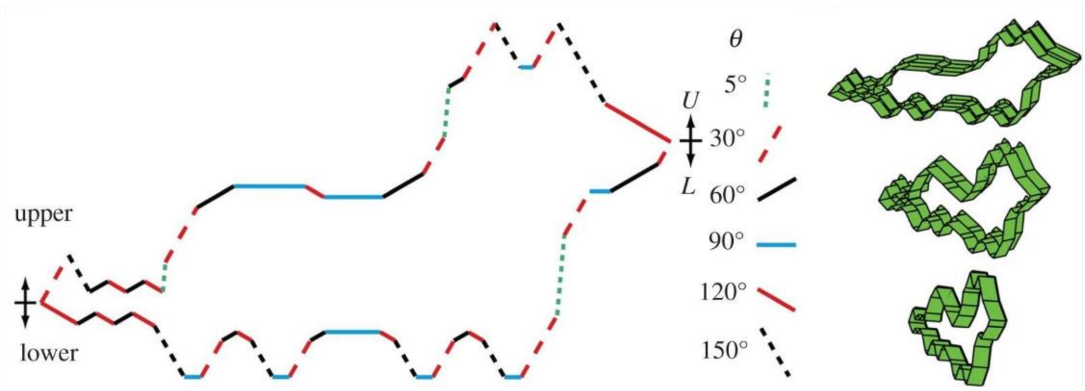

Fig. 1-10 Tube with a reconfigurable parallelogram cross-section [73].

1.2.2.4 Thick-panel origami

When the thickness of the panels is considered, the intersection problem cannot be avoided. Researchers have presented various thick folding techniques. As shown in Fig. 1-11(a), tapered surfaces were used to fold a Miura-ori pattern [74]. Offsets were introduced at the edge of the panels to fold a square-twist pattern with a thick-panel (Fig. 1-11(b)) [75]. A study showed that replacing a fold with two parallel folds can help in the folding of an origami pattern with a thick-panel (Fig. 1-11(c)) [76].

However, these methods often result in surfaces that are either not entirely flat or have openings to accommodate the thickness. In contrast to the above-mentioned methods, Hoberman introduced a technique to fold the Miura-ori pattern [77]; moreover, De Temmerman proposed a method to fold the diamond origami pattern [78] and Chen et al. presented an approach to reproduce the motions identical to those achievable using zero-thickness origami [79, 80] (as shown in Fig. 1-12). In this approach, the spherical linkage assembly for a zero-thickness sheet is replaced by an assembly of spatial linkages.

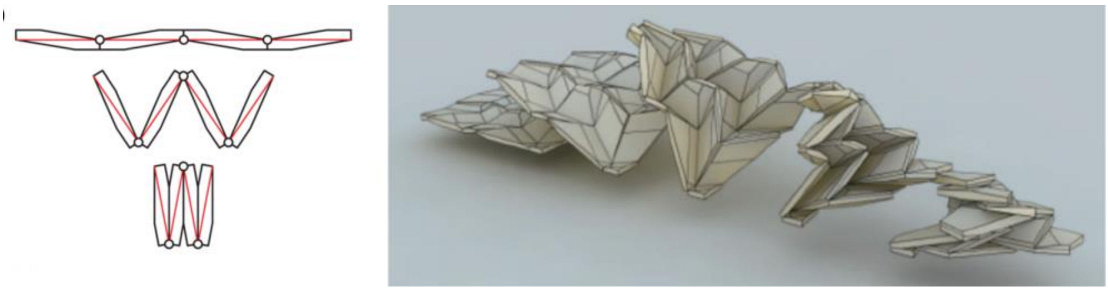

(a)

(b)

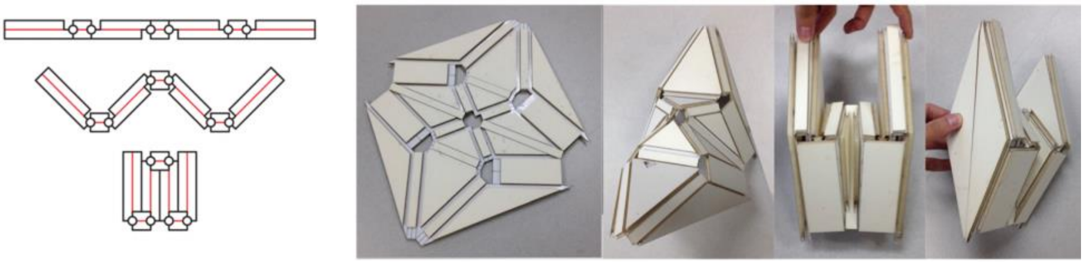

(c)

Fig. 1-11 Thickness accommodation methods: (a) tapered panel technique [74], (b) offset panel technique [75], (c) offset crease technique [76].

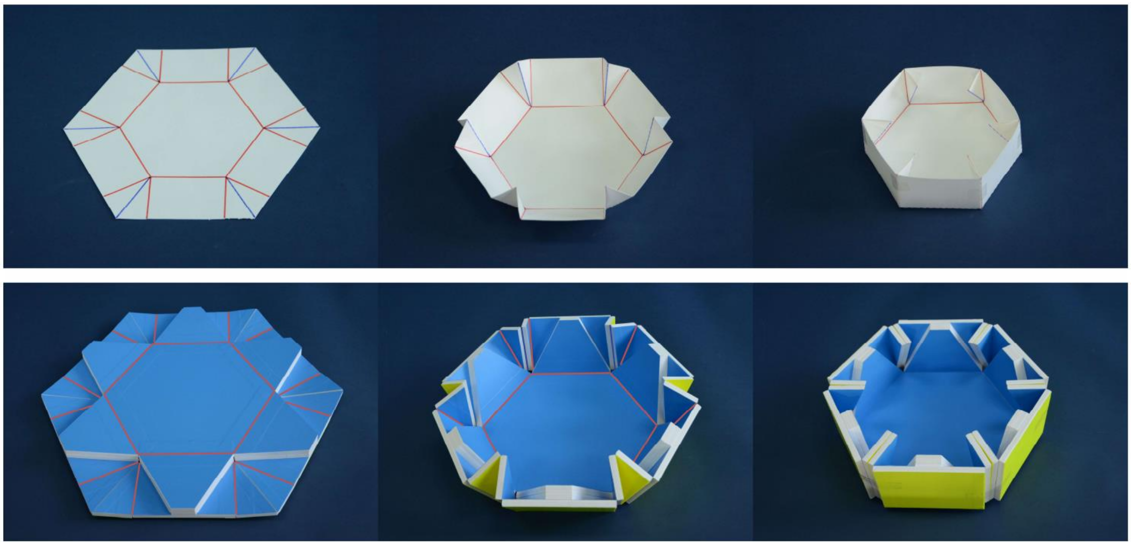

Fig. 1-12 A thick-panel origami model in which the spherical linkage assembly for the origami of a zero-thickness sheet is replaced by an assembly of spatial linkages [80].

1.2.2.5 Applications of Origami

Origami can be applied in the fields of space technology and robotics. Space missions require ultra-low-mass and large space plate forms or structures, such as antennas and solar panel arrays. Miura proposed a novel concept for the packing and deployment of large membranes in space by using the origami technique [81]. A solar panel array based on the Miura-ori pattern has been launched and tested in orbit [82]. Moreover, Miura proposed a foldable solar panel [83], a deployable antenna was presented by Morgan et al. [84], and a foldable telescopic lens was introduced by Debnath et al. [85]. These structures are illustrated in Fig. 1-13. The deployable structures are obtained based on the rigid origami technology, which is introduced in the next section. Structures developed using origami have large fold-deploy ratios. Furthermore, a deployable solar array for space application was designed in [86].

The origami technique can be used to fold planar material into complex 3D shapes, thereby facilitating the design of robotic systems. A self-folding robot with embedded electronics is illustrated in Fig. 1-14(a) [87], and a similar robot controlled using an alternating external magnetic field is shown in Fig. 1-14(b) [88]. The famous waterbomb pattern has been used to design parallel robots [89], worm-like robots [90, 91], floating equipment of aerial vehicles [92], and deformable wheels of a robot [93].

Moreover, origami techniques can also be used to design new metamaterials. Specifically, metamaterials with tuneable chirality have been designed [94-95] based on the deformation kinematics of certain existing origami patterns, such as the Miura-ori [94] and Kresling patterns [95]. By stacking many layers of the famous Miura-ori pattern, a metamaterial was proposed in [94]. This metamaterial helps achieve a negative Poisson’s ratio for both in-plane and out-of-plane deformations and can be

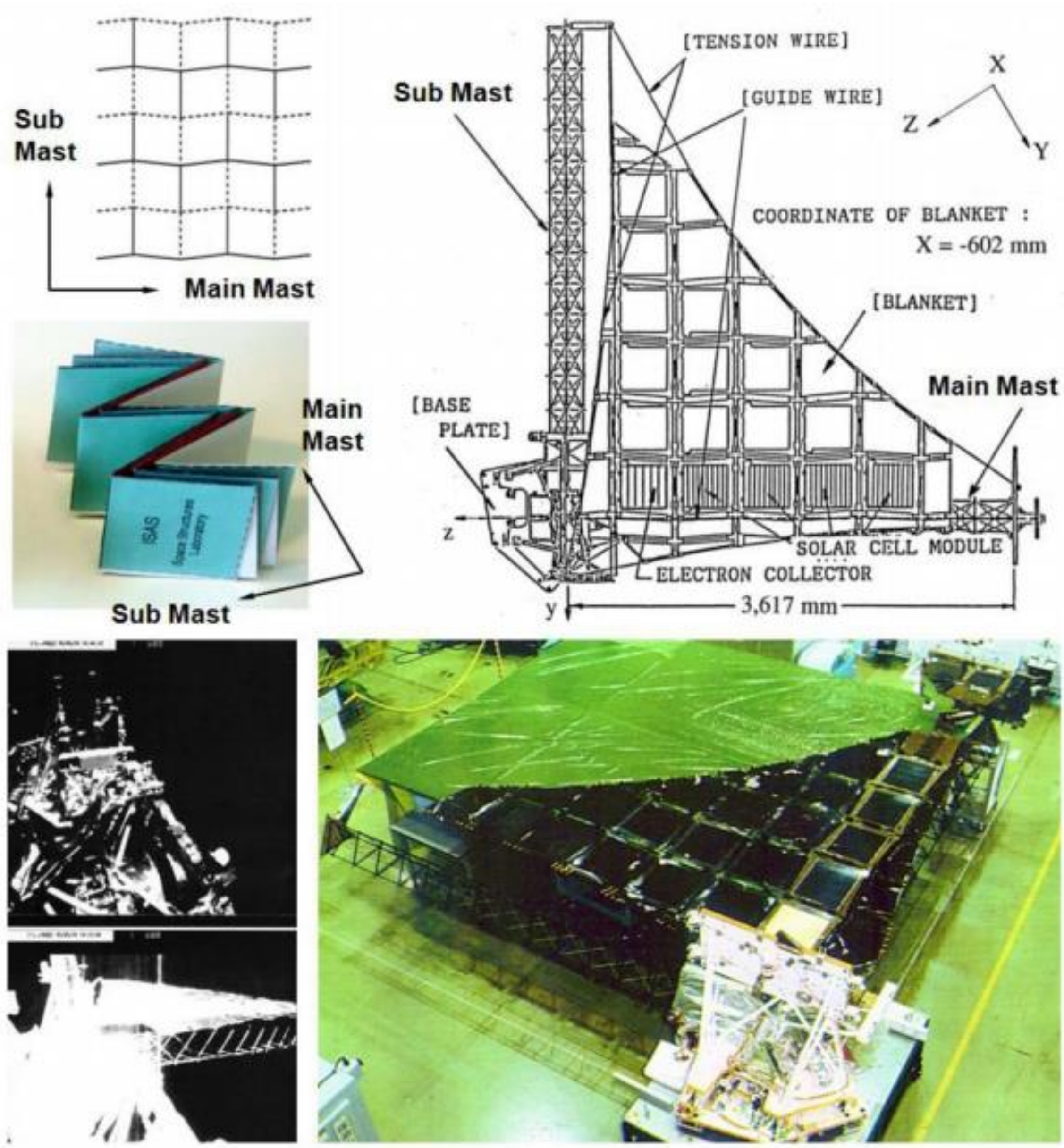

(a)

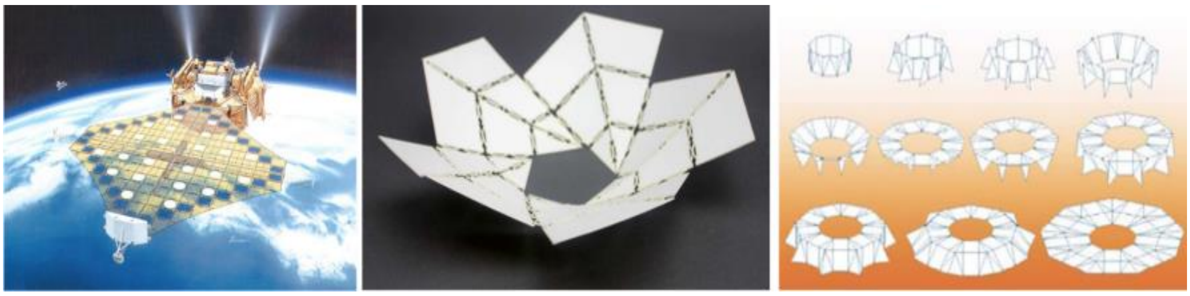

(b) (c) (d)

Fig. 1-13 Application of origami in the aerospace domain: (a) Miura-ori solar panel arrays [82]; (b) foldable solar panel [83]; (c) deployable antenna [84] and (d) foldable telescopic lens [85].

used as the core for blast-resistant sandwich beams [97] (see Fig. 1-15(a)). By introducing defects in the original Miura-ori pattern structure, this mechanical metamaterial can be reprogrammed [98]. Pratapa et al. introduced a four-vertex origami cell that could morph continuously between a Miura mode and an eggbox mode through the variation in the mountain and valley assignments of one of the creases, leading to a smooth switch through a wide range of negative and positive Poisson's ratios [99], as shown in Fig. 1-15(b). In addition to the periodic Miura-ori pattern, a non-periodic Ron Resch pattern has an unusually large load bearing capability, which can help build mechanical metamaterials [100]. Furthermore, the rigid origami tubes can be used as the basic units to construct metamaterials [101-103]. In addition to the design of metamaterials, the square-twist pattern [104], single vertexes in the Miura-ori pattern [105] and the waterbomb pattern [106] can be used to develop multi-stability structures.

In the civil engineering domain, the origami technique has been used in the design of mobile facets [70, 107, 108], reconfigurable and multi-locomotive devices [109, 110, 111] and other structures. In the biomedical engineering domain, an origami stent graft was developed [112], and several encapsulation origami robots [113-115] and origami surgical grippers [116, 117] were designed.

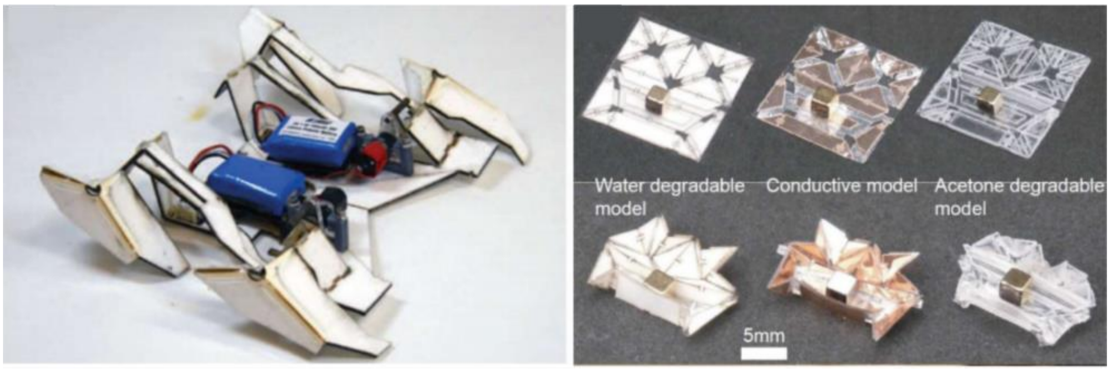

(a) (b)

Fig. 1-14 Origami robot: (a) electric drive robot [87], (b) magnetic drive robot [88].

1.2.2.6 Origami-inspired linkages

Inspired by rigid origami, several mechanisms have been developed. For instance, a parallel mechanism based on the waterbomb origami pattern was developed [118]. Extending this approach, Zhang and Dai proposed a plane-symmetric double-spherical 6*R* linkage, which was extracted from a closed-loop origami structure [119]. Feng derived a novel 6*R* linkage through a triangle twist origami pattern [120], as shown in Fig. 1-16.

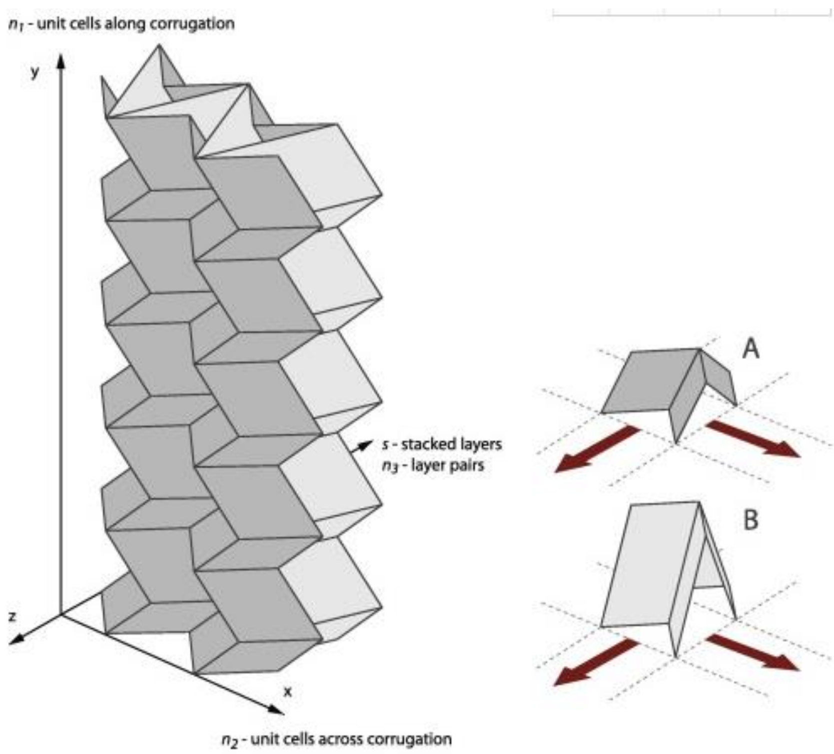

(a)

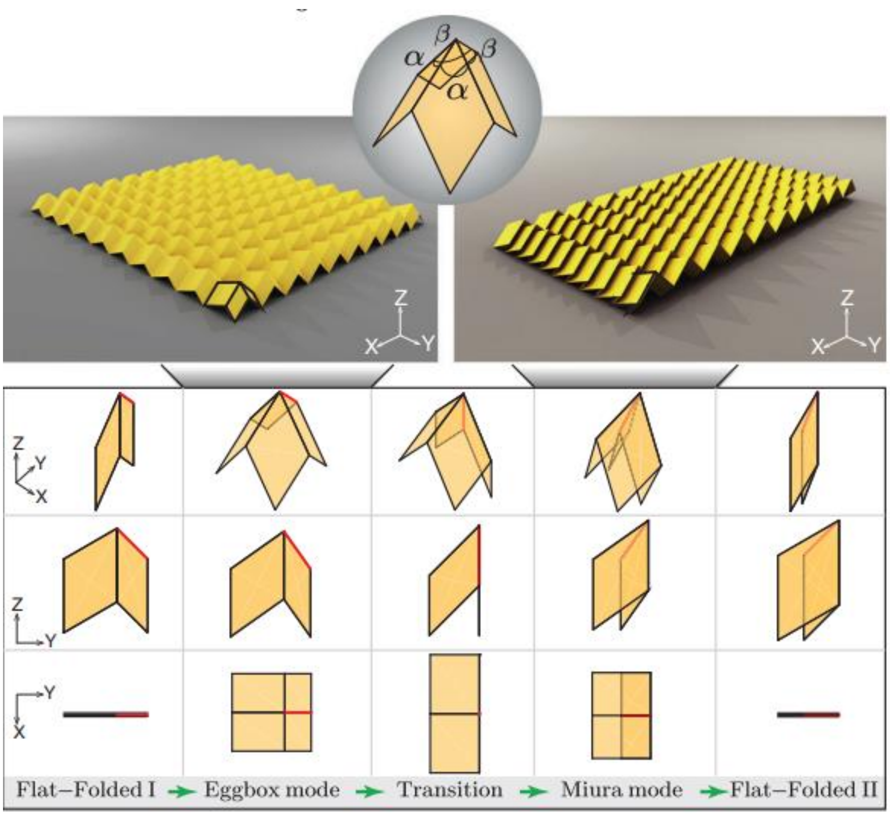

(b)

Fig. 1-15 Origami metamaterials: (a) core for sandwich beams [97] and (b) material with switchable Poisson's ratios [99].

1.2.3 Overconstrained spatial linkages and their networks

The mobility of a spatial linkage, that is, the number of independent coordinates needed to define the configuration of a kinematic chain or mechanism [121], can be determined using the Grübler–Kutzbach criterion [14].

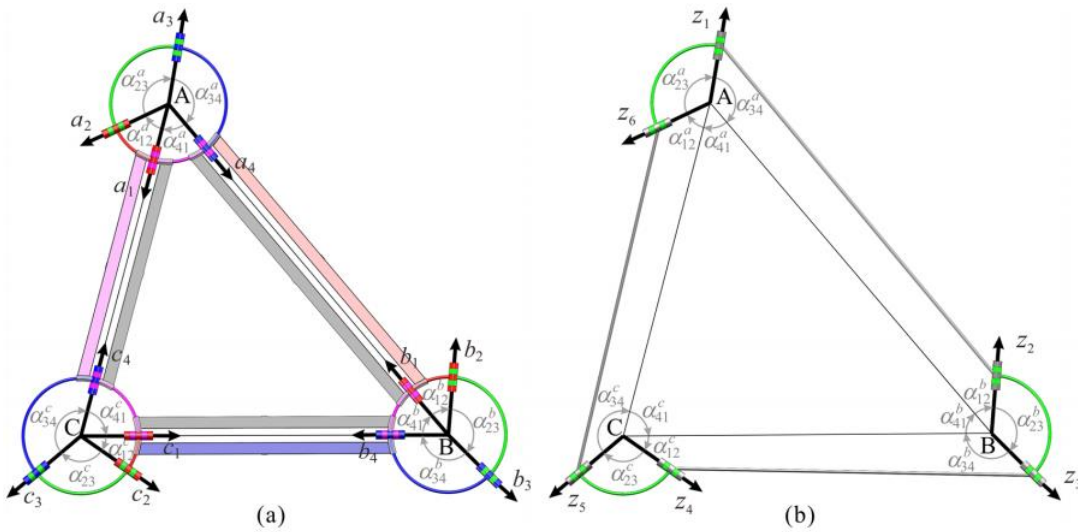

Fig. 1-16 Equivalent mechanisms of (a) triangle twist origami pattern, and (b) the derived overconstrained 6*R* linkage for the kirigami pattern [120].

$$m = 6(k - j - 1) + \sum_{i=1}^{j} d_i, \tag{1-8}$$

in which m is the number of DOFs of the linkage, k is the number of links in the linkage including the fixed link, j is the number of kinematic pairs in the linkage, and d_i is the number of DOFs for the ith kinematic pair.

Certain spatial linkages do not satisfy the mobility criterion in Eqn. (1-8) but are still mobile, and these linkages are known as overconstrained linkages [122].

1.2.3.1 Overconstrained 4*R* linkages

The Bennett linkage is a famous 4-bar spatial linkage with zero offsets in which alternative links have the same lengths and twists, and the lengths are proportional to the sine values of the corresponding twists, as illustrated in Fig. 1-17. According to the D-H notation, the following coordinates can be established:

$$\begin{aligned} a_{12} &= a_{34} = a, \\ a_{23} &= a_{41} = b, \end{aligned} \tag{1-9a}$$

$$\begin{aligned} \alpha_{12} &= \alpha_{34} = \alpha, \\ \alpha_{23} &= \alpha_{41} = \beta, \end{aligned} \tag{1-9b}$$

$$\sin\alpha / a = \sin\beta / b, \tag{1-9c}$$

$$R_i = 0, (i = 1, 2, 3 \text{ and } 4) \tag{1-9d}$$

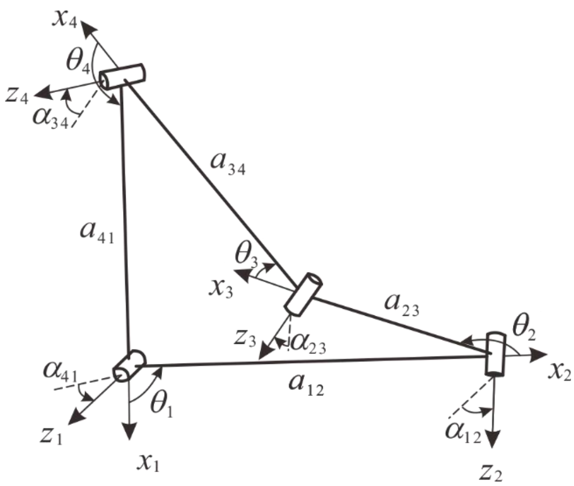

Fig. 1-17 Bennett linkage.

(a)

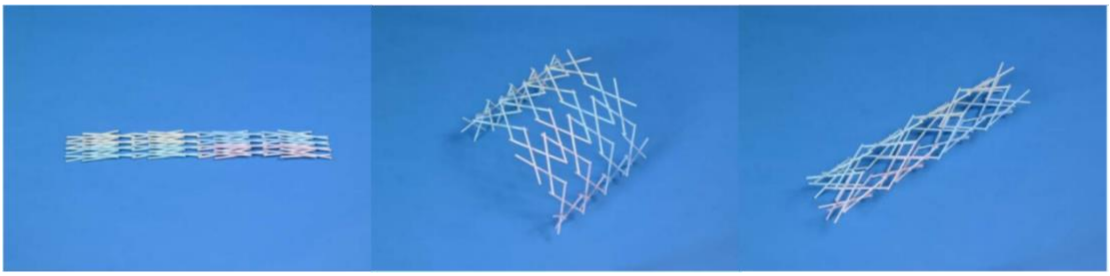

(b)

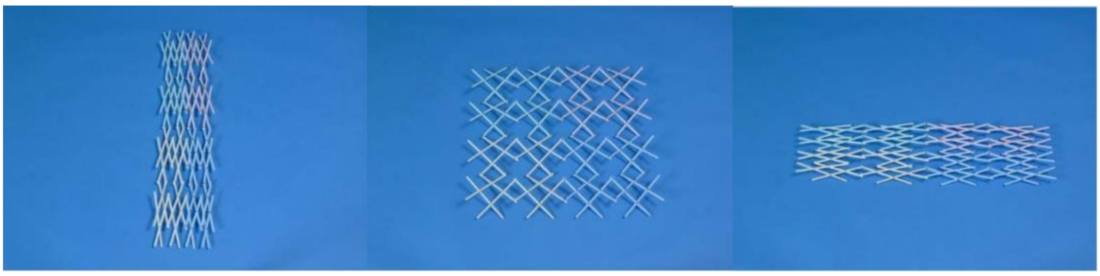

(c)

Fig. 1-18 Deployable structures of Bennett linkages: (a) cylinder; (b) arch and (c) flat deployable structure [123].

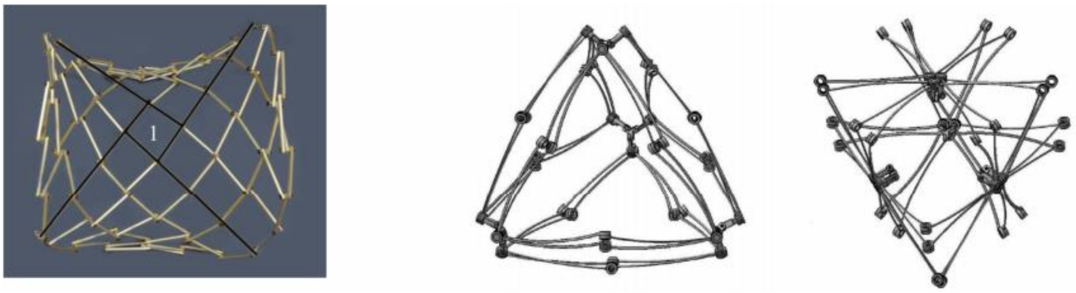

(a) (b)

Fig. 1-19 Mobile assemblies of Bennett linkages: (a) assembly approximating a saddle surface [125] and (b) tetrahedral linkage [126].

Chen designed a family of deployable structures based on the kinematics of Bennett linkages [123, 124] (shown in Fig. 1-18). In addition, the mobile assembly of Bennett linkages can be designed as a saddle surface [125] and polyhedrons [126]. These structures are shown in Fig. 1-19.

1.2.3.2 Overconstrained 5*R* linkages

The Goldberg 5*R* linkage [127] is obtained by combining a pair of Bennett linkages such that a common link of two combined linkages is removed and a pair of adjacent links is rigidly attached to each other; this process can be explained as the summation or subtraction of two Bennett linkages to produce a new linkage.

The Myard 5*R* linkage [128], which is composed of two rectangular Bennett linkages with one pair of twist angles [129], is shown in Fig. 1-20. It can be observed that the two Bennett linkages ABCD and ADCE are arranged as mirror images. By combining these linkages in the symmetric plane, the common joint D and common links AD and CD (grey parts in Fig. 1-20) can be removed. The geometric conditions are as follows:

$$
\begin{aligned}
& a_{34}=0,\ a_{12}=a_{51},\ a_{34}=a_{45}, \\
& \alpha_{23}=\alpha_{45}=\frac{\pi}{2},\ \alpha_{51}=\pi-\alpha_{12},\ \alpha_{34}=\pi-2\alpha_{12}, \\
& R_i=0\ (i=1, 2, 3, 4 \text{ and } 5) \text{ and} \\
& a_{12}=\alpha_{23}\sin\alpha_{12}.
\end{aligned}
\tag{1-10}
$$

A family of mobile assemblies of Myard linkages was designed by Liu and Chen [130], and one of the assemblies is shown in Fig. 1-21(a). Two types of large spatial assemblies of Myard linkages with different twist angles were developed by Qi and Deng [131], and one of the assemblies is shown in Fig. 1-21(b).

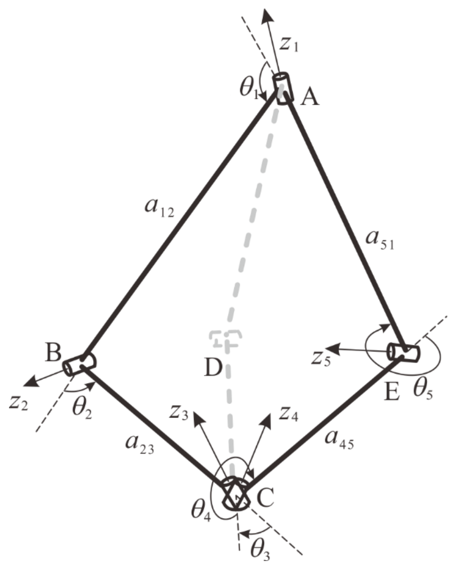

Fig. 1-20 Myard linkage.

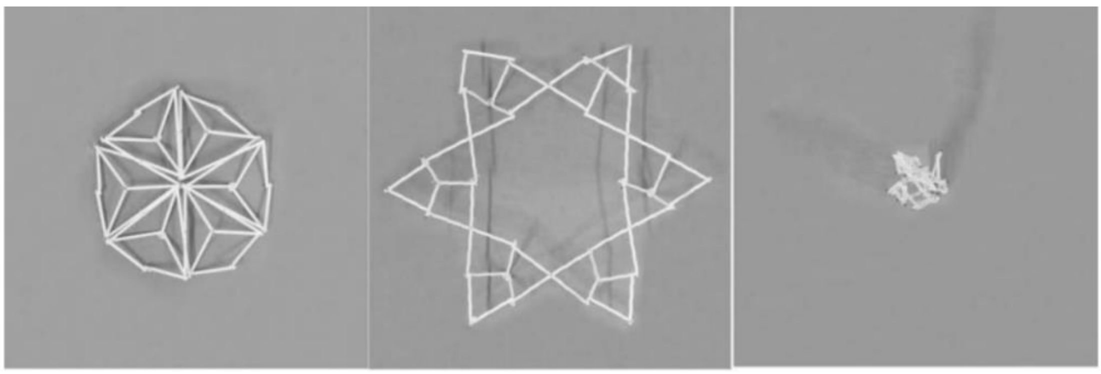

(a)

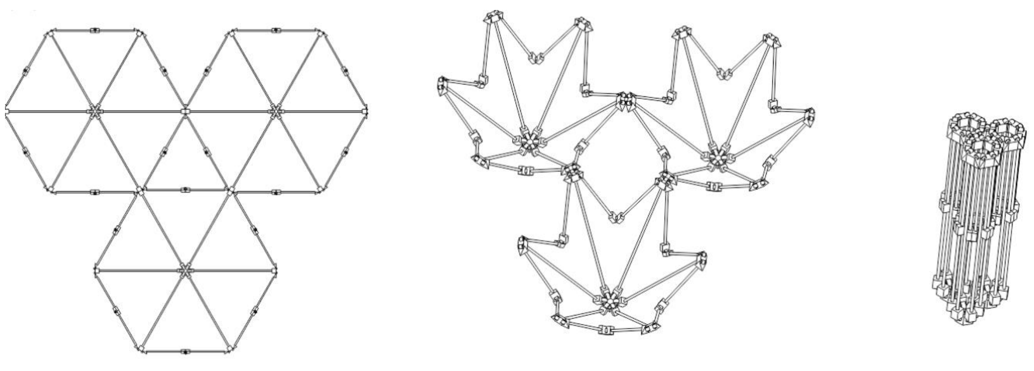

(b)

Fig. 1-21 Mobile assemblies of Myard linkages: (a) assembly constructed by Liu and Chen [130] and (b) by Qi and Deng [131].

1.2.3.3 Overconstrained 6*R* linkages

The Sarrus linkage was the first 3D overconstrained linkage to be reported [132], and this linkage was analysed by Bennett [133]. A schematic is shown in Fig. 1-22. The four links A, R, S, and B, as well as the links A, T, U, and B are consecutively hinged by three parallel horizontal hinges. The directions of the two sets of hinges are different, and link A can exhibit rectilinear motion, vertically up and down, relative to link B. This linkage can be assembled with other mechanisms to construct deployable structures [134, 135].

Similar to Goldberg 5*R* linkages, a 6*R* linkage was generated by merging three Bennett linkages [136]. Figure 1-23 illustrates the construction of a Goldberg 6*R* linkage by the summation of three Bennett linkages, where the common parts shown in the grey lines are removed. Two other double-Goldberg 6*R* linkages [137] were created by summing Goldberg 5*R* linkages. Next, a complete family of double-Goldberg 6*R* linkages was proposed [138] by combining a subtractive Goldberg 5*R* linkage and Goldberg 5*R* linkage. All the Goldberg 5*R* and 6*R* linkages are Bennett-based overconstrained linkages, and since the Bennett linkage is the construction unit, the corresponding geometric condition should be satisfied for all the linkages.

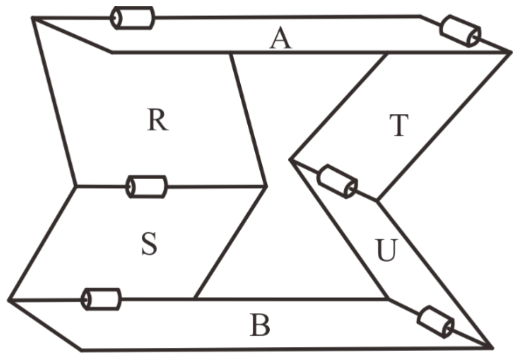

Fig. 1-22 Schematic of a Sarrus linkage.

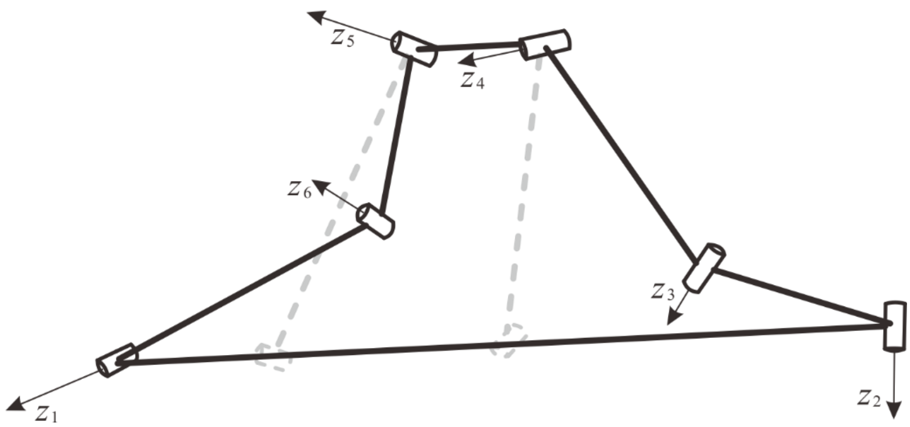

Fig. 1-23 Construction of a Goldberg 6*R* linkage.

Bricard proposed six distinct types of mobile 6*R* linkages [139], which are shown in Figs. 1-24(a) to (f). The geometric conditions of these six cases are as follows.

In the line-symmetric case,

$$
\begin{aligned}
&a_{12}=a_{45}, a_{23}=a_{56}, a_{34}=a_{61}, \\
&\alpha_{12}=\alpha_{45}, \alpha_{23}=\alpha_{56}, \alpha_{34}=\alpha_{61}, \\
&R_1=R_4, R_2=R_5, R_3=R_6.
\end{aligned} \tag{1-11a}
$$

In the plane-symmetric case,

$$
\begin{aligned}
&a_{12}=a_{61}, a_{23}=a_{56}, a_{34}=a_{45}, \\
&\alpha_{12}+\alpha_{61}=\pi, \alpha_{23}+\alpha_{56}=\pi, \alpha_{34}+\alpha_{45}=\pi, \\
&R_1=R_4=0, R_2=R_6, R_3=R_5.
\end{aligned} \tag{1-11b}
$$

In the trihedral case,

$$
\begin{aligned}
&a_{12}{}^2+a_{34}{}^2+a_{56}{}^2=a_{23}{}^2+a_{45}{}^2+a_{61}{}^2, \\
&\alpha_{12}=\alpha_{34}=\alpha_{56}=\pi/2, \alpha_{23}=\alpha_{45}=\alpha_{61}=3\pi/2, \\
&R_1=R_2=R_3=R_4=R_5=R_6=0.
\end{aligned} \tag{1-11c}
$$

In the line-symmetric octahedral case,

$$
\begin{aligned}
&a_{12}=a_{23}=a_{34}=a_{45}=a_{56}=a_{61}=0, \\
&R_1+R_4=R_2+R_5=R_3+R_6=0.
\end{aligned} \tag{1-11d}
$$

In the plane-symmetric octahedral case,

$$
\begin{aligned}
&a_{12}=a_{23}=a_{34}=a_{45}=a_{56}=a_{61}=0, \\
&R_2=-R_1\sin\alpha_{34}/\sin(\alpha_{12}+\alpha_{34}), R_3=R_1\sin\alpha_{12}/\sin(\alpha_{12}+\alpha_{34}), R_4=-R_1, \\
&R_5=R_1\sin\alpha_{61}/\sin(\alpha_{45}+\alpha_{61}), R_6=-R_1\sin\alpha_{45}/\sin(\alpha_{45}+\alpha_{61}).
\end{aligned} \tag{1-11e}
$$

In the doubly collapsible octahedral case,

$$
\begin{aligned}
&a_{12}=a_{23}=a_{34}=a_{45}=a_{56}=a_{61}=0, \\
&R_1R_3R_5+R_2R_4R_6=0.
\end{aligned} \tag{1-11f}
$$

Bricard linkages has been extensively studied. Lee presented the closure equations for the three octahedral cases according to the matrix transformation [140]. Chai and Chen proposed a stationary structural configuration of the line-symmetric octahedral case with identical twists and offsets [141]. Baker analysed the planar, spherical and skew counterparts of the doubly collapsible octahedral case [142]. Wohlhart analysed the orthogonal case and proposed two distinct trihedral cases [143]. Baker analysed the line-symmetric case with the reciprocal screw system [144] and examined the plane-symmetric case of a Bricard linkage through the reciprocal screw system approach [145]. Li and Schicho investigated the movability of a plane-symmetric Bricard linkage based on the theory of bonds [146]. Deng et al. presented a geometric approach to design and synthesize a plane-symmetric Bricard linkage [147].

In terms of the networks of Bricard linkages, Chen and You [148] presented a mobile assembly of threefold-symmetric Bricard linkages, which could be folded to a handle and deployed to a flat surface, as illustrated in Fig. 1-25 (a). Moreover, an alternative form of the threefold-symmetric Bricard linkage was discussed [148]. Huang, Deng and Li [149] formed a deployable structure based on a Bricard linkage with a scissor-like connection, as shown in Fig. 1-25(b).

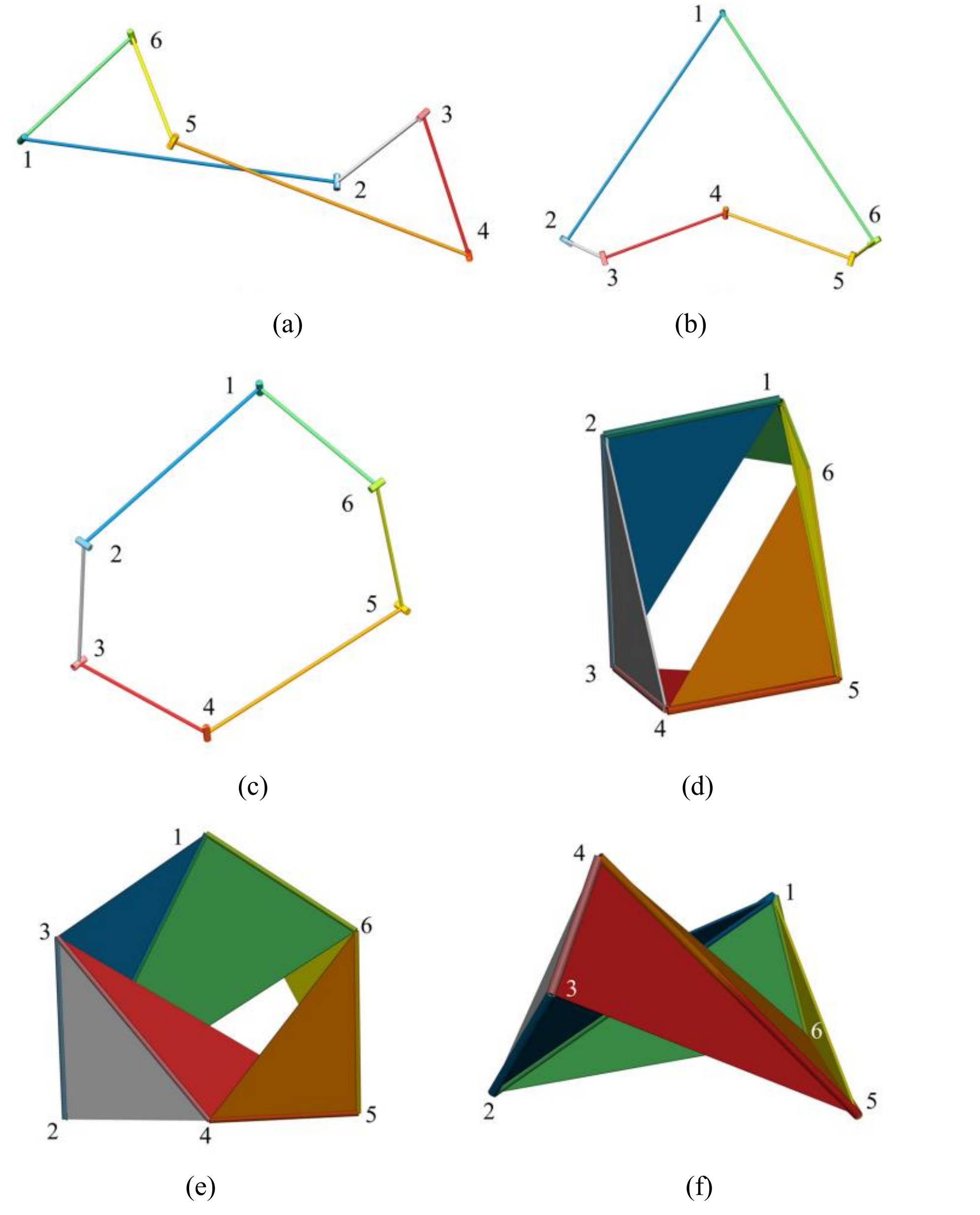

Fig. 1-24 Bricard 6R linkages: (a) General line-symmetric case, (b) general plane-symmetric case, (c) trihedral case, (d) line-symmetric octahedral case, (e) plane-symmetric octahedral case, and (f) doubly collapsible octahedral case [120].

In addition to the Bennett-based and Bricard linkages, other 6R overconstrained linkages exist. Baker presented the compatible conditions of a double-Hooke’s-joint linkage, which has been widely used as a transmission coupling mechanism [150] with the following geometric conditions:

$$a_{23} = a_{34} = a_{56} = a_{61} = 0,$$
$$\alpha_{23} = \alpha_{34} = \alpha_{56} = \alpha_{61} = \pi/2, \tag{1-12}$$
$$R_1 = R_2 = R_3 = R_6 = 0.$$

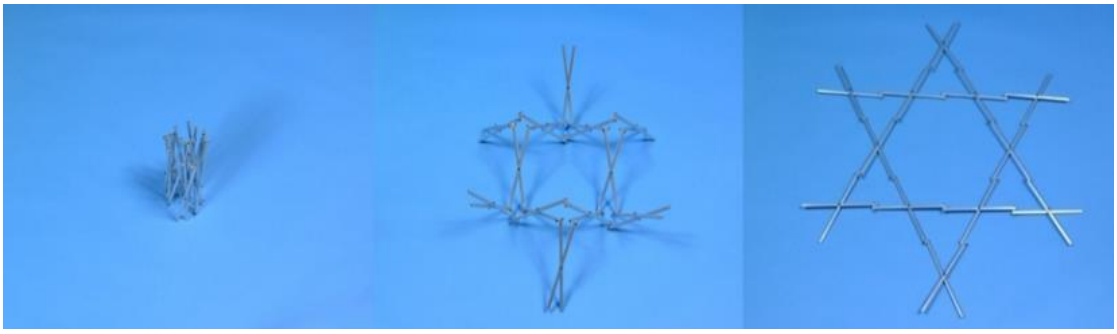

(a)

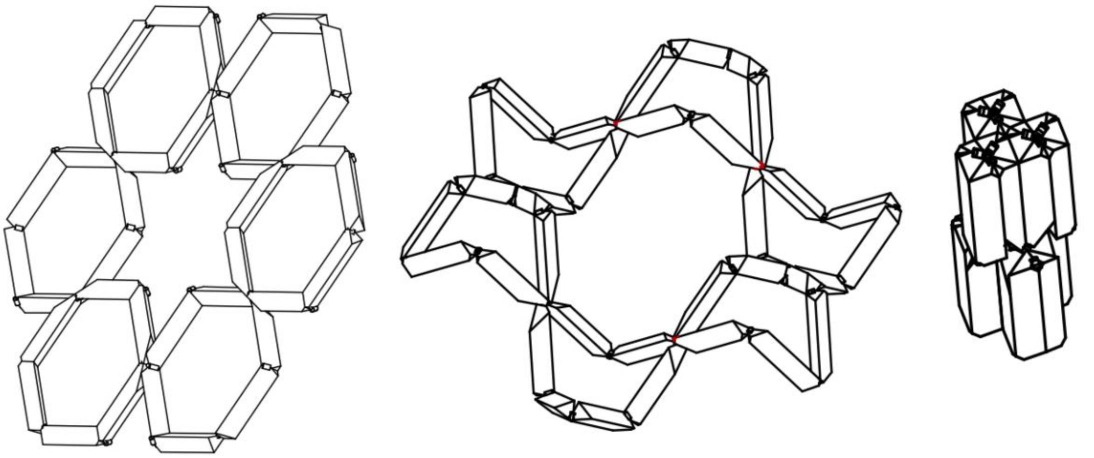

(b)

Fig. 1-25 Mobile assemblies of Bricard linkages. (a) assembly of threefold-symmetric Bricard linkage constructed by Chen and You [148] and (b) assembly formed using scissor-like connection based hexagon Bricard modules by Huang, Deng and Li [149].

In this section, the kinematics theories of the linkages are reviewed, several overconstrained linkages are introduced, and the geometrical conditions of the linkages are summarized.

1.3 Aim and Scope

Focused on the interdisciplinary area of kinematics and structure, this thesis is aimed at examining the kinematics of the assembly of spherical linkages, known as rigid origami, and extending the family of deployable structures based on spherical linkages.

In this process, inspired by rigid origami patterns, a 1D helical structure with switchable and hierarchical chirality is presented, which is constructed by assembling origami-inspired units in series. Next, an approach to obtain morphing surfaces inspired by the eggbox pattern, which is a 2D network of spherical linkages, is proposed. Finally, the 3D network of spherical linkages is studied, an extended family of rigid origami tubes is proposed and the approach to construct thick-panel origami tubes is presented.

1.4 Outline of the Dissertation

This dissertation consists of six chapters.

Chapter 1 presents a brief review of the existing works pertaining to the mechanism theory to analyse the linkages, compatible conditions for closed-loop linkages and deployable structures composed of revolute hinges. Moreover, as origami is a special technique for designing deployable structures, its definition and applications are described in this chapter.

Chapter 2 describes the helical structures with switchable and hierarchical chirality inspired by origami techniques. Eggbox-based chiral units are proposed to construct homogeneous and heterogeneous chiral structures and a theoretical approach to tune the chirality of these structures by modulating the geometrical parameters is demonstrated, whose chirality switching is realized through mechanism reconfiguration. Moreover, hierarchical structures with a chirality transfer from the construction elements to the morphological level are designed and a novel helix with two zero-height configurations during the unwinding process is developed.

Chapter 3 describes the method to construct morphing surfaces inspired by the eggbox origami pattern by developing a one-DOF surface that can transform from a parabolic cylinder to a paraboloid.

Chapter 4 describes the extended family of rigid origami tubes. Using a mechanism construction process, existing origami tubes can be used as building blocks to form new tubes that are rigidly foldable with a single degree-of-freedom. A combination process is adopted, along with the choice of inserting new facets into an existing tube. The approach can be applied to both single and multi-layered tubes with a straight or curved profile.

Chapter 5 describes the method to construct thick-panel origami tubes. By replacing the spherical 4*R* linkages in the original zero-thickness tubes with spatial overconstrained mechanisms, thick-panel origami tubes with line-symmetric and planar-symmetric cross-sections are obtained, and these tubes can reproduce motions identical to those of zero-thickness structures.

Chapter 6 presents the concluding remarks and describes the scope of future research.

Chapter 2 1D mobile networks of spherical linkages: helical structures with switchable and hierarchical chirality

2.1 Introduction

Chirality has emerged as a new research domain in biological and chemical communities. Compared with achiral structures, chiral structures may have special physiological properties or pharmacological effects. Moreover, manipulation of specific morphological chirality is a promising approach to design metamaterials with tailored mechanical, optical, or electromagnetic properties. However, the realization of many properties found in nature, such as switchable and hierarchical chirality, which can allow electromagnetic control of the polarization of light and enhancement of mechanical properties, in human-made structures remains challenging. In this section, based on origami techniques, helical structures with switchable and hierarchical chirality are described.

This chapter is organized as follows. In Chapter 2.2, eggbox-based chiral units used to construct homogeneous and heterogeneous chiral structures are presented, and Chapter 2.3 theoretically demonstrates chirality tuning by modulating the geometrical parameters. Next, Chapter 2.4 describes the realization of the chirality switching in a single-helix via mechanism bifurcation without any external stimulus. Chapter 2.5 describes a hierarchically chiral structure with two zero-height configurations. The concluding remarks are presented in Chapter 2.6.

2.2 Construction and geometry of chiral units

Chirality refers to the asymmetric configurational property of an object or a system that cannot be superposed onto its mirror image [151]. Chirality is typically realized morphologically at the macroscale through a helix. Origami-inspired metamaterials with tuneable chirality have been designed [94-96]. Considering this aspect, I examined whether origami techniques can be adopted to create novel helical structures.

To achieve the torsional or helical morphology of chiral structures, first, a twisted origami unit is constructed. The basic origami pattern used is that of an eggbox, which is a non-developable four-crease pattern (i.e., the pattern cannot be flattened onto a plane without overlap or separation). Two identical eggboxes are placed symmetrically to construct a chiral unit (Fig. 2-1(a)). To induce twisting properties, the two eggboxes must fold simultaneously. Therefore, a parallelogram OAED is added to rigidly connect the pair of coplanar facets OAB and OCD (Fig. 2-1(b), where the dotted line represents the crease not in view); thus, no rotation occurs in the connected plate. When all the four facet pairs in the two eggboxes are connected in this manner, an interconnected unit is obtained. The unit can be twisted anticlockwise and clockwise when compressed and elongated, respectively, and thus, this unit is defined as a right-handed (RH) chiral unit. If the connection segment to the parallelogram OBFC is changed, as shown in Fig. 2-1(c), a left-handed (LH) chiral unit is obtained, which twists clockwise when compressed.

Two design parameters, a and α, are adopted to characterize the chiral unit (Fig. 2-1(d)), which denote the lateral edge length and sector angle of the eggbox, respectively. To quantitatively analyse the chirality of the structures, three more parameters are introduced, as shown in Fig. 2-1(d), where ϕ is the dihedral angle between the two lower facets connecting the two eggboxes (i.e., the unit configuration angle), γ is the angle between the two horizontal alternative creases (i.e., the unit twist angle) and h is the distance between the bottom and top faces (i.e., the unit height).

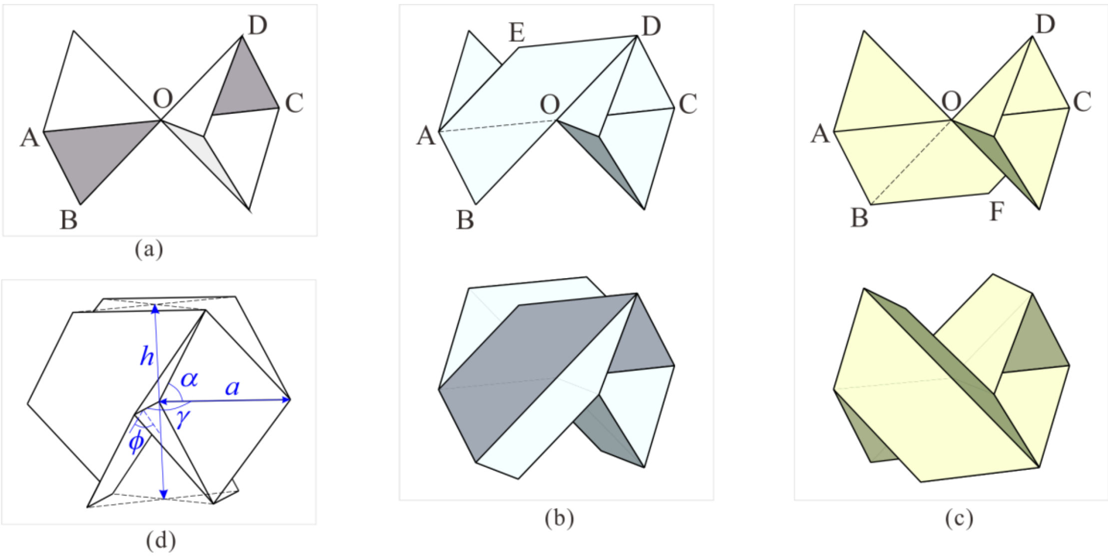

Fig. 2-1 Construction of the origami-inspired chiral unit: (a) basic element; (b, c) construction of a right-handed (RH) and left-handed (LH) unit and (d) geometrical parameters in the chiral unit.

Figure 2-2(a) shows an RH chiral unit with a 4-crease eggbox pattern containing four panels and four creases, AO, BO, CO and DO. As shown in Fig. 2-2(a), the four creases intersect at a common point O, the four dihedral angles between each two adjacent panels are ω_1, ω_2, ω_3 and ω_4, the angle between OA and OC is γ_1, and ϕ and γ denote the configuration angle and twist angle, respectively. According to the cosine formula for a spherical triangle, the following relationships can be derived:

$$\cos\gamma = \cos^2\alpha + \sin^2\alpha\cos\omega_1, \tag{2-1a}$$

$$\cos(\gamma/2) = \cos\alpha\cos(\gamma_1/2) + \sin\alpha\sin(\gamma_1/2)\cos(\omega_1/2), \tag{2-1b}$$

$$\cos(\gamma_1/2) = \cos\alpha\cos(\gamma/2) + \sin\alpha\sin(\gamma/2)\cos(\omega_2/2). \tag{2-1c}$$

Substituting Eqns. (2-1a) and (2-1b) in Eqn. (2-1c) yields the following relationship between ω_1 and ω_2:

$$\tan(\omega_1/2)\tan(\omega_2/2)=1/\cos\alpha \tag{2-2}$$

Moreover, Fig. 2-2 shows that

$$\omega_2=\pi-\phi. \tag{2-3}$$

Substituting Eqns. (2-2) and (2-3) in Eqn. (2-1a) gives

$$\cos\gamma=\cos^2\alpha+\sin^2\alpha\cos(2\arctan(1/\cos\alpha\tan((\pi-\phi)/2))). \tag{2-4}$$

Moreover, the unit geometry yields the following relationship:

$$h=2a\sin\alpha\cos(\phi/2). \tag{2-5}$$

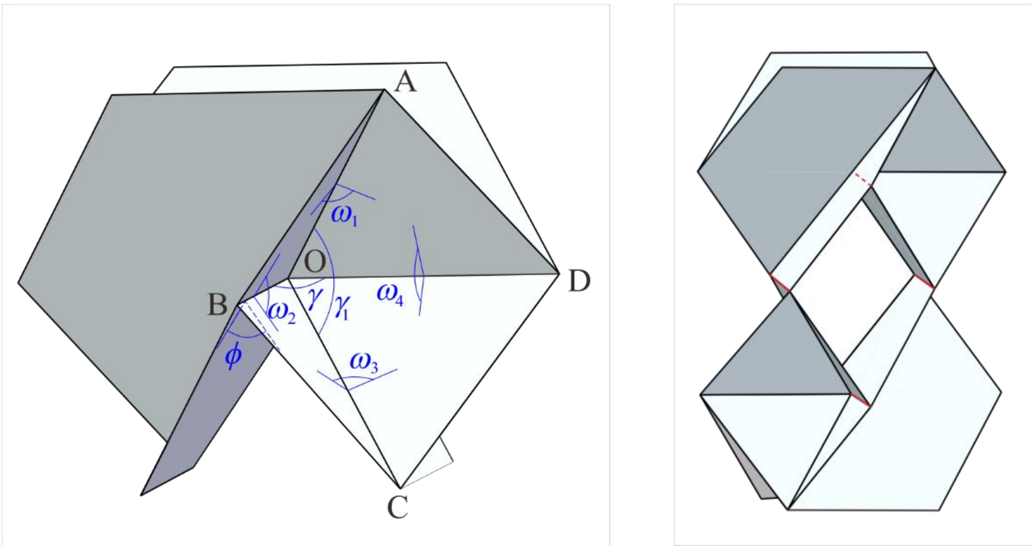

(a) (b)

Fig. 2-2 RH chiral units: (a) geometry and (b) connection.

By connecting identical chiral units at the parallel edges on the bottom or top faces, homogeneous RH or LH chiral structures can be obtained and an example is illustrated in Fig. 2-2(b), where the red lines represent the connected edges. The rotational angle and distance between the top and bottom faces of the structure are defined as the structural twist angle Γ and structural height H, respectively. Since the chiral units are placed in series, the structural twist angle and structural height can be simply calculated as $\Gamma=N\gamma$ and $H=Nh$, respectively, where N is the number of units in the structure. Figure 2-3(a) presents paper model photographs of an RH chiral structure with a maximum twist angle of 360°, constructed using three RH units with $\alpha=60^\circ$. In the same manner, an LH chiral structure can be derived, as shown in Fig. 2-3(b). The chirality of the structure is characterized by a virtual helix, which is formed by connecting the same vertex in each chiral unit, as indicated by the red line in Fig. 2-

3(e).

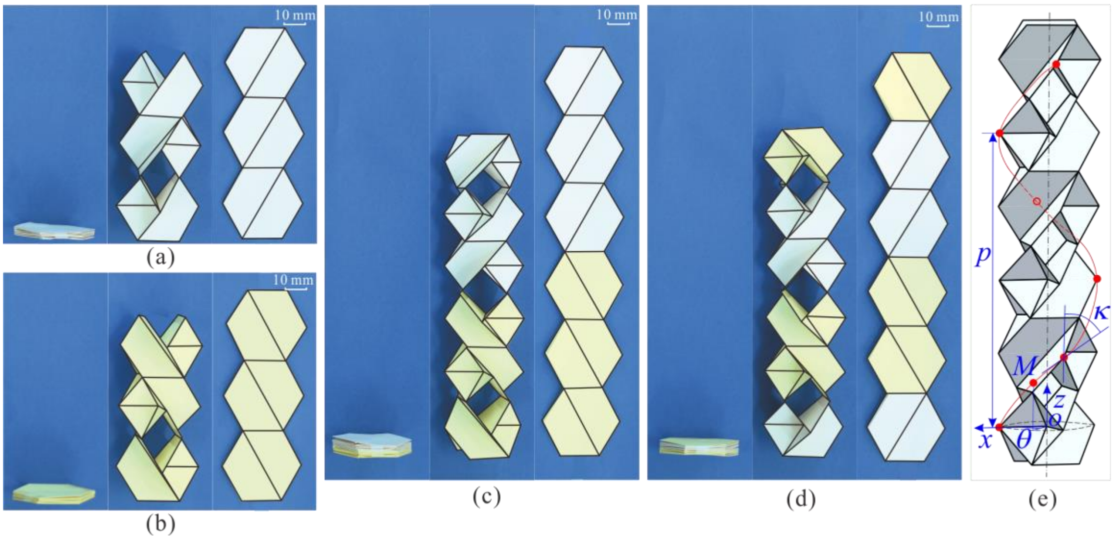

Fig. 2-3 Chiral structures: (a–d) paper model photographs of chiral and achiral structures: (a) RH chiral structure; (b) LH chiral structure; (c) and (d) achiral structure; (e) geometrical parameters in the chiral structure.

In addition to these homogeneous structures, heterogeneous chiral structures can be generated by mixing RH and LH units. The expressed chirality of the structure is determined by the number of RH and LH units, whereas the arrangement of these units changes only the internal twist angle in the structure. An achiral structure is obtained when the number of RH units equals the number of LH units since the chirality of the whole structure is counteracted in this case. For example, Fig. 2-3(c) shows an achiral structure with a maximum internal twist angle of 360°, obtained by connecting the RH and LH chiral structures shown in Figs. 2-1(b) and 2-1(c), respectively. If the arrangement of the chiral units is changed, as shown in Fig. 2-3(d), the structure remains achiral but with a decreased maximum internal twist angle of 240°

The same vertex in each chiral unit forms a virtual helix defined by the pitch p and helical angle κ, as shown in Fig. 2-3(e). According to the definition of p and κ, $p = 2\pi h / \gamma$ and $\tan\kappa = 2\pi a / p$. Winding (by twisting the chiral units) can be considered to describe the behaviour of the helix. A coordinate system wherein the *z*-axis is along the helical axis (see Fig. 2-3(e)) is established, the *x*-axis is along the radial direction pointing to the origin of the helix, and the *y*-axis is determined by the right-hand rule. Therefore, the helix can be expressed as

$$\begin{cases} x = a\cos\theta \\ y = a\sin\theta \\ z = p\theta / 2\pi \end{cases}. \tag{2-6}$$

where a is the radius of the helix, which is equal to the lateral edge length of the eggbox, and θ is the winding angle of an arbitrary point M on the helix. When the chiral unit folds from the maximum height to zero, ϕ increases from 0° to 180°, and γ ranges from zero to 2α.

2.3 Tunability of single chiral structures

The chirality of single chiral structures can be tuned by adjusting their design parameters, specifically, the sector angle α and number of units, N. Since the effect of N on the chirality is linear, I attempted to tune the chirality by modulating α. To determine the influence of α on the folding behaviour and the helical properties when a is constant, three cases with $\alpha = 40^{\circ}$, 60° and 80° are considered. Using Eqns. (2-1), (2-4) and (2-5), the relationship among the non-dimensional unit height h/a, unit twist angle γ, and unit configuration angle ϕ can be determined, as shown in Fig. 2-4(a). When folding the chiral unit, γ increases to 2α, and h decreases to zero. For a given ϕ, a larger α corresponds to larger h/a and γ values. Hence, a chiral structure with a larger α is more twisted when equally folded. Moreover, the folding of the chiral units generates the helix winding of the whole structure.

The folding of chiral units generates helical winding of the whole structure. In general, κ is considered as the characteristic quantity for a helical structure. During the folding process, the helical pitch p reduces to zero, whereas κ increases to $\pi/2$, according to Fig. 2-3(e). The relationship between κ and ϕ is presented in Fig. 2-4(b). This figure shows that κ is positively related to α when ϕ is constant, which means that a larger value of α can be adopted to design a more highly wound helix. With the increase in κ, p/a and h decrease, whereas γ increases (Figs. 2-4(c and d)). Moreover, the relationship between p/a and κ (Fig. 2-4(c)) remains unchanged for different values of α, which indicates that either p/a or κ can determine the helical properties of the helix. Furthermore, the helix becomes more wound with the twisting of the chiral unit. The coupling between the twisting of the chiral unit and winding of the helix can be clarified considering the relationship curve of γ and κ, as shown in Fig. 2-4(d). This figure shows that for helices with identical κ, a larger α always produces a larger γ. Thus, in cases with a larger α, fewer units are needed to complete a helix turn. The slope of the curve shown in Fig. 2-4(d) indicates that the rate of variation in γ first increases and later decreases as κ increases, indicating that the twisting of the chiral unit is more sensitive to the winding of a less-wound helix.

The manifestation of the phenomena for RH chiral models with different α values is demonstrated experimentally in Fig. 2-4 (e), which shows the photographs of three representative configurations for each paper model with unit twist angles of γ=40°, 60° and 80°. In all three cases, the structural height increases as γ reduces, which is in agreement with the theoretical trend shown in Fig. 2-4(a). However, the structure is less folded in the case of a larger α, leading to a larger height for a given value of γ, which is consistent with the predicted behaviour in Fig. 2-4(a). Therefore, α can be tubed to design chiral structures with the target properties of the helices (e.g., height and degree of folding).

The analytical results were validated by conducting a tensile experiment on a homogeneous RH chiral structure made of ENDURO Ice material with $N = 4$ and α=60°. Each RH unit in the specimen consists of four identical panels, as illustrated in Fig. 2-5(a). To strengthen the stiffness of the specimen to avoid panel deformation, each panel was constructed using two layers of 0.3-mm-thick ENDURO Ice material (a tear-resistant, transparent paper material), cut using a Trotec Speedy 300 laser cutter (produced by Trotec in Austria) with a cutting power and speed of 64 W and 70 mm/s, respectively, during the cutting process and glued together with 502 adhesive. An RH unit in the specimen was fabricated by connecting four panels with tape (Scotch Tough Duct Tape, produced by Minnesota Mining and Manufacturing in America), as shown in Fig. 2-5(b) in which a and α denote the lateral edge length and sector angle of the eggbox, respectively, with a=40 mm and α=60°. The specimen consisted of four such units connected by Scotch tape.

To avoid the influence of gravity, the tensile experiment was conducted on a horizontal testing machine developed in-house, as presented in Fig. 2-5(c). The experiment was conducted in the displacement-control mode, and the experimental data of the displacement and force on the specimen were collected using a data acquisition system. The machine had a 50 N load cell (JLBS-50N, produced by Bengbu Sensor System of Engineering in China), with a resolution and maximum displacement of 0.25 N and ΔH=238 mm, respectively.

During the experiment, the displacement rate was set as 5 mm/min to eliminate the dynamic effects. A dial was used to observe $\Delta\Gamma$, which is the structural twist angle increment, as illustrated in Fig. 2-5(d). The instrument involved two parts, where one part is attached to the specimen by using a holder and can rotate with the end of the specimen, and the other is a nonrotatable part attached to the testing machine. The experimental displacement data were recorded every 10° of dial rotation.

Photographs of four representative configurations of the structure during the tension process are presented in Fig. 2-6(a). The theoretical and experimental relationships between $\Delta\Gamma$ and the structural height increment ΔH are presented as blue dots and black lines in Fig. 2-6(b), respectively. In this case, a = 40 mm, $\Delta\Gamma = \Gamma - \Gamma_0$, $\Delta H = H - H_0$, and Γ_0 is the initial structural twist angle when H_0 = 25 mm. The experimental data match with the analytical results, and $\Delta\Gamma$ decreases exponentially as ΔH increases. The slight deviation in the experimental data can be attributed to the small rotational stiffness of the creases of the physical specimen, which is assumed to be zero in the theoretical model.

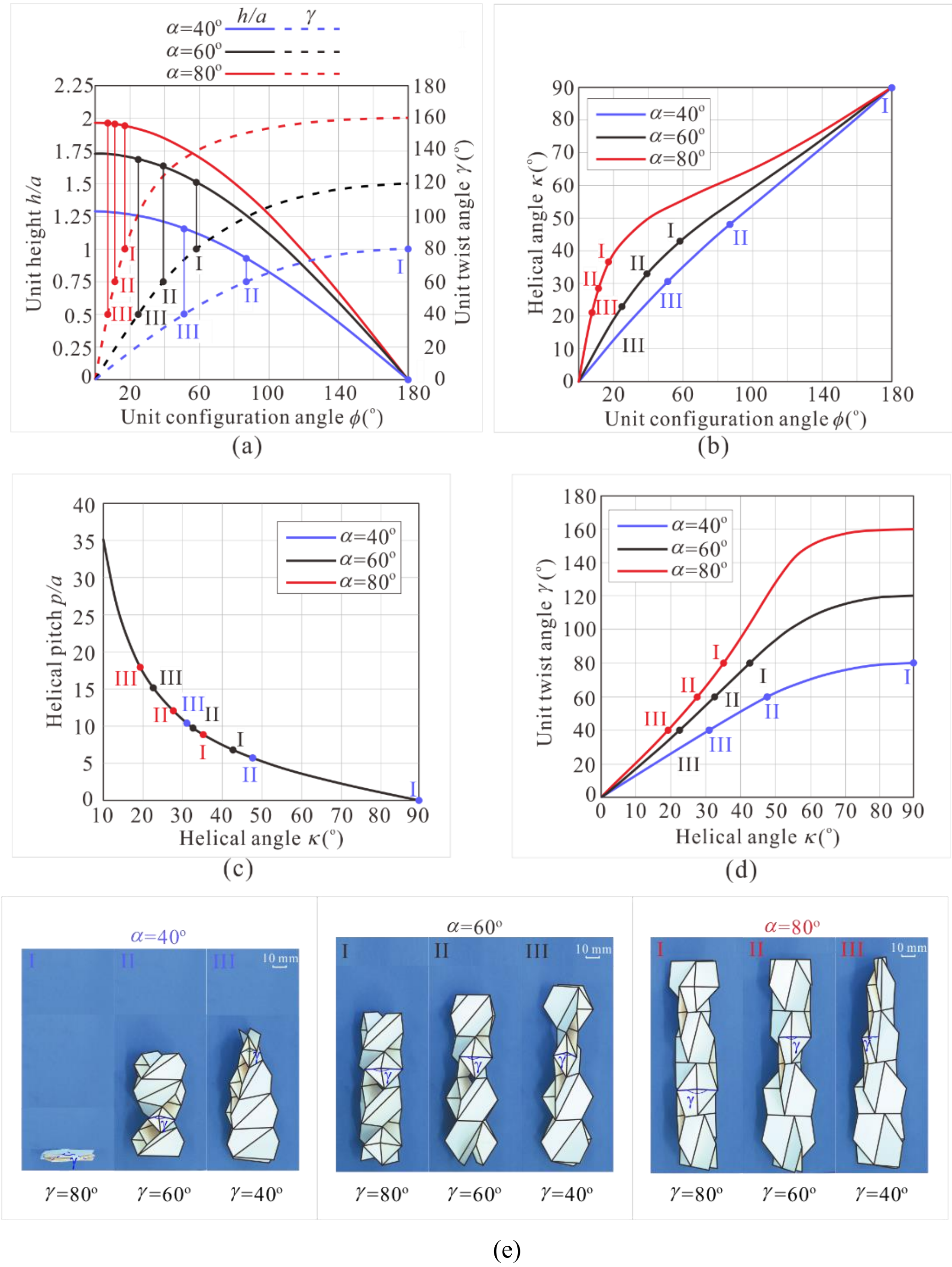

Fig. 2-4 Helical characteristics of the RH chiral structure when α is set as 40° (blue line), 60° (black line) and 80° (red line): (a) relationship among the non-dimensional unit height h/a, γ and ϕ; (b) relationship between angle κ and ϕ; (c) relationship between the non-dimensional helical pitch p/a, and κ; (d) relationship between γ and κ. (e) photographs of three configurations of the paper models.

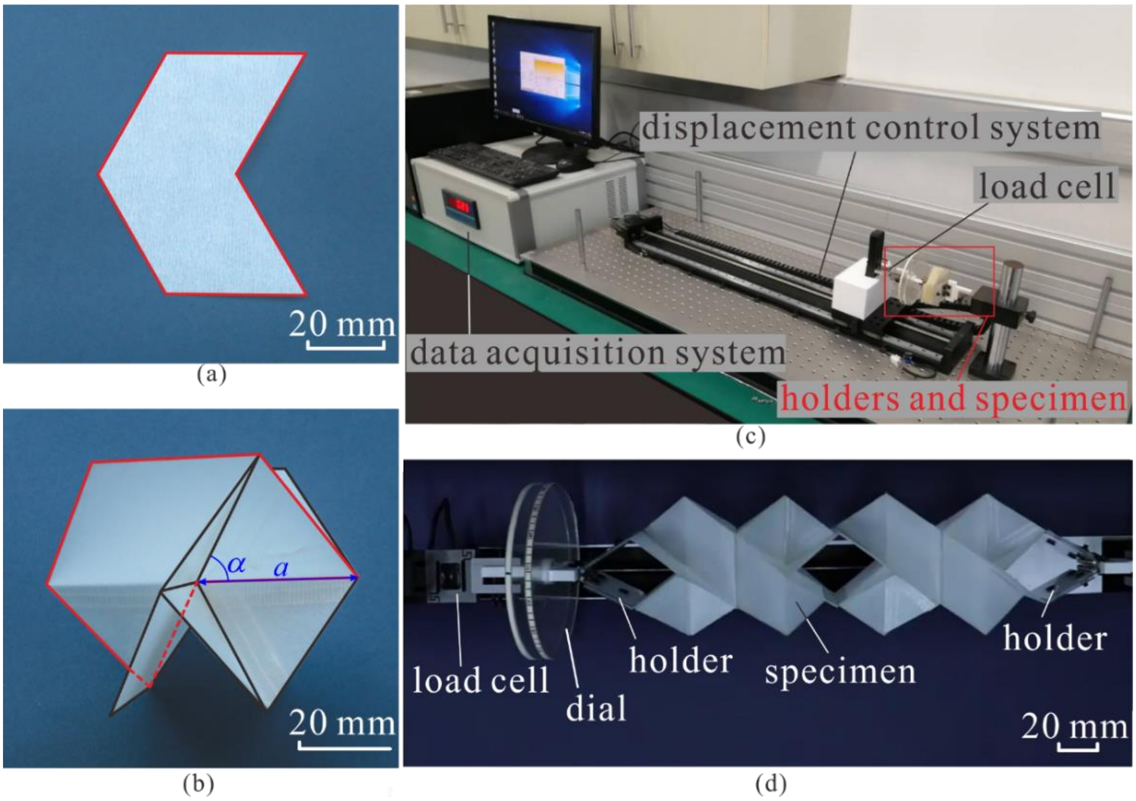

Fig. 2-5 Specimen fabrication and experiment. (a) One panel in an RH chiral unit of the specimen. (b) One RH unit in the specimen. (c) Data acquisition and test system of the horizontal testing machine. (d) Attachment of the specimen to the testing machine.

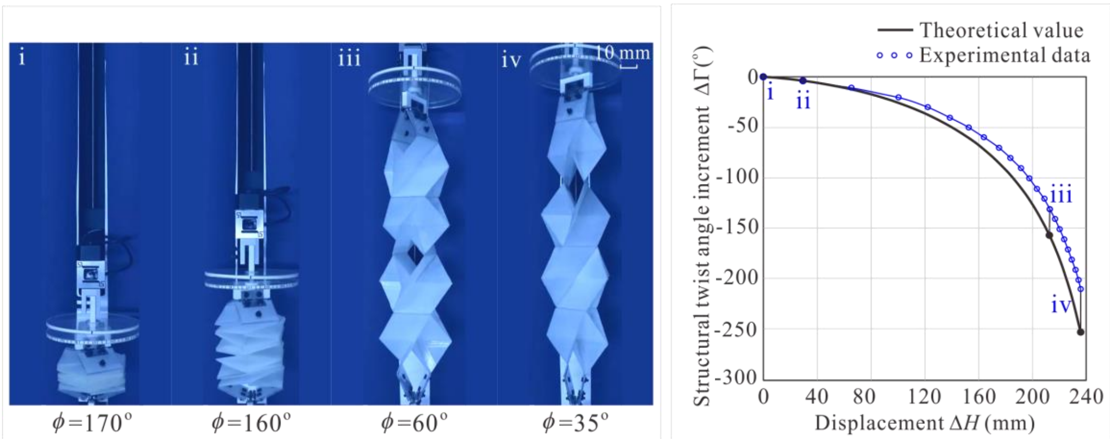

Fig. 2-6 Result of the tensile experiment: (a) tensile experiment; (b) theoretical (black line) and experimental (blue dots) $\Delta\Gamma$ versus ΔH .

Thus, I clarified the twist and helical properties of homogeneous RH structures as well as the chirality tuneability. In the case of LH structures, only the handedness changes, and the helical properties remain the same in the geometry design and folding cases. Therefore, LH structures exhibit the same behaviour.

2.4 Chirality switching

In general, the chirality of a structure is fixed once the structure is designed. The chirality switching in chiral structures allows the electromagnetic control of the polarization of light and enhancement of the mechanical properties. However, this switching is challenging to realize in human-made chiral structures owing to the different construction of RH or LH structures. This problem also exists in the developed paper models: the movement of the RH chiral structure in Fig. 2-7(a) is terminated when the model reaches the fully elongated state owing to the facet interference. To achieve chirality switching, the connection between the two eggboxes must be changed. From a mechanistic perspective, the chiral structure can be regarded as a network of spherical 4*R* and planar 4*R* linkages, and a different chirality corresponds to different motion branches of the whole linkage network. Inspired by the concept of reconfiguration, this study represents the first attempt to achieve chirality switching through mechanism bifurcation (i.e., changes to different motion branches through the singularity configuration). Since the fully elongated configuration is a singularity configuration, the idea is to redesign the structure to avoid facet interference while maintaining its bifurcation property at this point. By replacing the paper facets with curved links without changing their rotational axes, the facet interference can be avoided. The model with the redesigned links is kinematically equivalent to the paper model. Exploiting the bifurcation of the spherical 4*R* and planar 4*R* linkages, an RH chiral structure can be transform to an LH structure through the fully elongated configuration. This chirality switching process is illustrated in Fig. 2-7(b) in which configurations I and II correspond to RH chirality, IV and V correspond to LH chirality, and III corresponds to the critical position at which the switching occurs.

To determine the variation in the twisting and helical properties during the chirality switch, γ and h/a are plotted as functions of κ, as shown in Figs. 2-7(c) and (d), respectively. This analysis indicates that the switch occurs in the configuration with $\kappa = 0^{\circ}$ and $\gamma = 0^{\circ}$, which corresponds to the fully elongated configuration with the maximum unit height. This switching behaviour is different from that of most previously reported examples wherein chirality switching is induced by external stimuli [152-155]. Moreover, this behaviour is different from the spontaneous chirality switching found in bacterial flagella where periodic chirality switching occurs in certain regions of the flagellum and travels as a pulse along the length of the filament [156]. Since chirality switching in the structure is achieved by mechanism bifurcation, the structure can be fabricated and controlled more easily compared to the existing mechanisms with molecular structural changes. Because of the switch, the range of the helical angle is expanded to $[-90^{\circ}, 90^{\circ}]$, which is two times that of the paper structure presented in Figs 2-1 and 2-3.

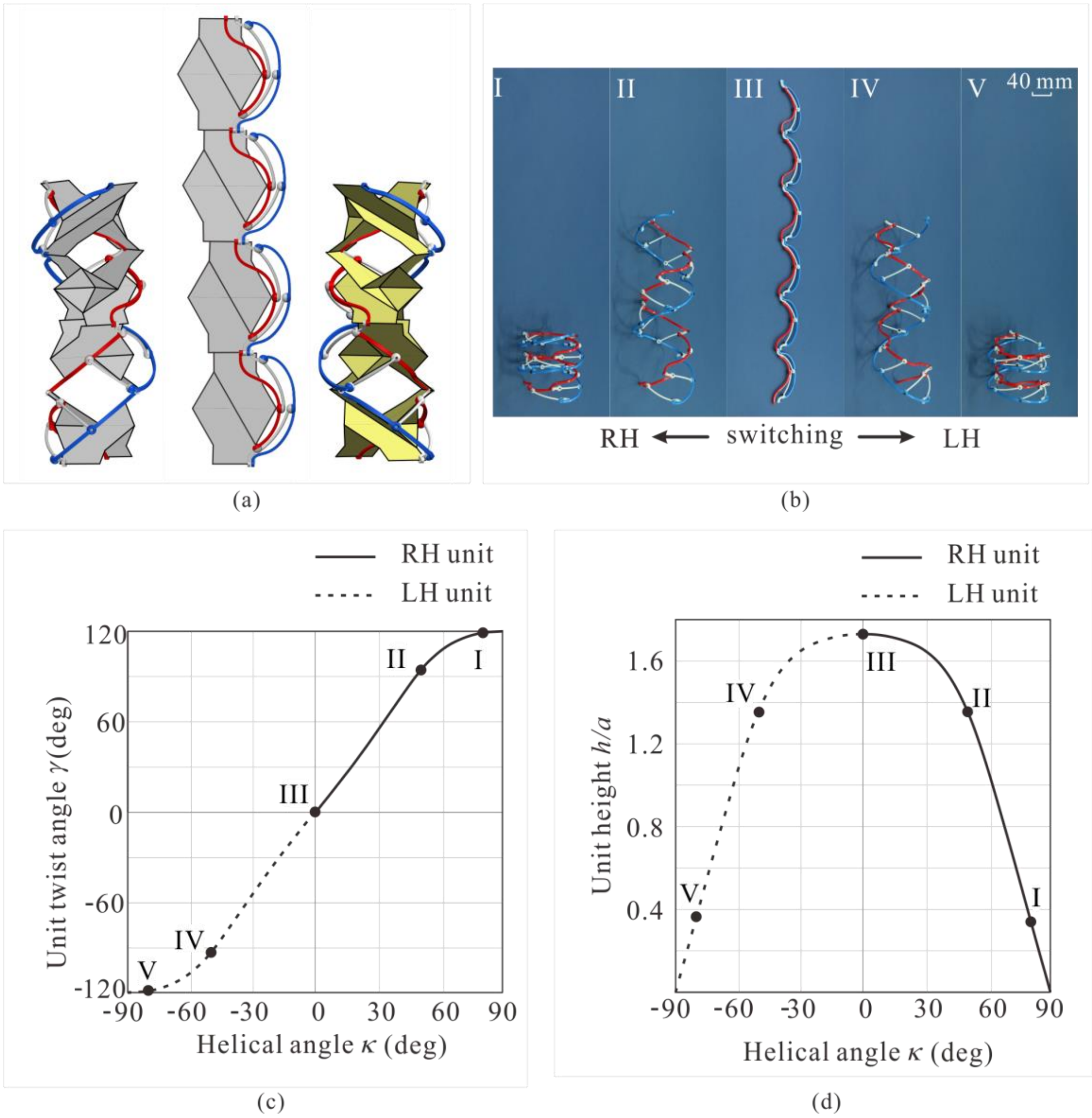

Fig. 2-7 RH and LH chirality switching: (a) design of the switchable chiral structure; (b) photographs of 3D-printed and manually assembled linkage models; (c) relationship between the unit twist angle γ and helical angle κ; (d) relationship between the non-dimensional unit height h/a, and κ.

2.5 Hierarchically chiral structures

To achieve a hierarchically chiral structure with more helices, the apex of each eggbox should not be located along the same axis as in the previous single case shown in Fig. 2-1 in which the connection between the adjacent chiral units must be changed. The chiral construction unit is altered to a more general unit, as shown in Fig. 2-8(a), introducing one additional parameter β, which is the sector angle of the connection part. The creases of the connection part are presented as dashed lines in Fig. 2-8(b). The hierarchically chiral structure has two helices, defined as the major and minor helices, represented by the thick and thin red lines in Fig. 2-8(c), respectively. The major helix is formed by the apex of each eggbox, whereas the minor helix is formed by one identical vertex in the base of each eggbox, which is the same as the single-helix in our paper model shown in Fig. 2-3(e). Similar to the previously reported synthetic hierarchically chiral structures [157, 158], our structure transfers chirality at the same macroscale, owing to which, the dimensions of the two helices have the same order of magnitude (centimetre scale in this case). Four parameters, K, P, R and L, are introduced to characterize the major helix, specifically, the helical angle, helical pitch, radius and length along the helical axis, respectively. A coordinate system where the z-axis is along the helical axis of the major helix is established, the x-axis is along the radial direction pointing to the origin of the helix, and the y-axis is determined by the right-hand rule. The equation of the major helix is

$$\begin{cases} x = R\cos\theta_{\mathrm{m}} \\ y = R\sin\theta_{\mathrm{m}} \\ z = P\theta_{\mathrm{m}} / 2\pi \end{cases}, \tag{2-7}$$

where θ_{m} is the winding angle of each point on the major helix. The equation of the minor helix is expressed as

$$\begin{cases} x = R\cos\theta_{\mathrm{m}} - r\cos\theta_{\mathrm{s}}\cos\theta_{\mathrm{m}} + rP\sin\theta_{\mathrm{s}}\sin\theta_{\mathrm{m}} / \sqrt{4\pi^2R^2+P^2} \\ y = R\sin\theta_{\mathrm{m}} - r\cos\theta_{\mathrm{s}}\sin\theta_{\mathrm{m}} - rP\sin\theta_{\mathrm{s}}\cos\theta_{\mathrm{m}} / \sqrt{4\pi^2R^2+P^2} \\ z = P\theta_{\mathrm{m}}R\sin\theta_{\mathrm{m}} / (2\pi) + 2\pi Rr\sin\theta_{\mathrm{s}} / \sqrt{4\pi^2R^2+P^2} \end{cases}. \tag{2-8}$$

where r is the radius of the minor helix, which equals a, and θ_{s} is the winding angle of each point on the minor helix.

Next, the helical properties of the hierarchical chiral structure is analysed. With the introduction of the major helix, an unusual property of the hierarchically chiral structure can be observed, which does not occur in the existing synthetic and biological structures with a monotonically increasing height during the unwinding process; specifically, the height of the structure first increases from zero to the maximum value and later decreases to zero when the structure is unwound (i.e., as K varies from 90° to 0°), as shown in Fig. 2-8(d). Photographs of the physical model (made of ENDURO Ice material) of five representative configurations made of 12 RH units with α = 60° and β = 30° are presented along with their corresponding unit configuration angles.

Figure 2-9(a) presents a hierarchically chiral structure with $N = 8$, where O_i (i=1 to 8) forms the major helix. To obtain the equation of the major helix, the coordinates of points O_1 to O_8 must be expressed in the same global frame. The local coordinate frame F_i is established in each unit i, as illustrated in Fig. 2-9(b), where the Z_i-axis is along the direction of vector $\mathbf{B}_i\mathbf{D}_i$, the X_i-axis is along the direction of vector $\mathbf{O}_i\mathbf{B}_i \times \mathbf{B}_i\mathbf{D}_i$, and the Y_i-axis can be determined by the right-hand rule. Moreover, ω_1, ω_2, and γ are defined in accordance with Fig. 2-2, and ρ_1 and ρ_2 represent two dihedral angles in the connection part. The position vector of point O_i in the local frame F_i is obtained as

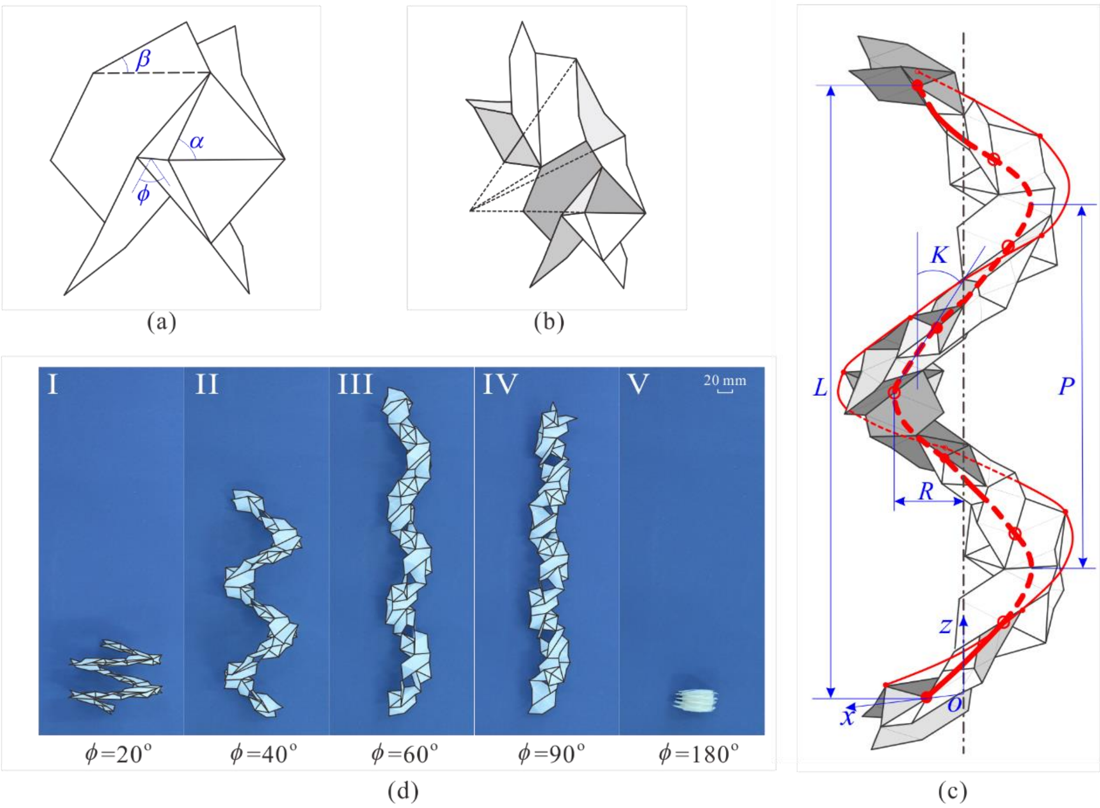

Fig. 2-8 Design and helical characteristics of the hierarchically chiral structure: (a) altered chiral unit; (b) two connected altered chiral units; (c) geometrical parameters in the hierarchically chiral structure; (d) photographs of five configurations of the hierarchically chiral structure.

$$\mathbf{p}_{i,i} = \begin{pmatrix} 0 \\ -a\cos(\gamma/2) \\ a\sin(\gamma/2) \end{pmatrix}, \tag{2-9}$$

where the first and second i values in subscript (i,i) represent point O_i and frame F_i, respectively. In two adjacent chiral units,

$$\mathbf{P}_{(i+1),i} = \boldsymbol{T}\mathbf{P}_{(i+1),(i+1)}, \tag{2-10a}$$

$$\mathbf{P}_{i,j} = \begin{pmatrix} \mathbf{p}_{i,j} \\ 1 \end{pmatrix}, \tag{2-10b}$$

where $\boldsymbol{T}$ is the transformation matrix that transforms the expression in frame F_{i+1} to F_i. $\boldsymbol{T}$ is identical for different *i* because all the units in the structure are identical.

Figure 2-9(c) presents the transformation process from frame F_i to F_{i+1} through frames f_{i1} to f_{i13} in which axis z_{i1}, which is determined based on the rotation from axis Z_i around axis X_i with a rotation angle of $(\pi-\gamma)/2$, is along the direction of vector $\mathbf{B}_i\mathbf{O}_i$; axis x_{i2}, which is obtained by the rotation from axis x_{i1} around axis z_{i1} with a rotation angle of $\pi-\omega_2/2$, is along the direction of vector $\mathbf{A}_i\mathbf{B}_i\times\mathbf{B}_i\mathbf{O}_i$; frame f_{i3} is obtained by the translation from frame f_{i2} along vector $\mathbf{B}_i\mathbf{O}_i$; axis z_{i4}, which is obtained by the rotation from axis z_{i3} around axis x_{i3} with the rotation angle of $-\alpha$, is along the direction of vector $\mathbf{A}_i\mathbf{O}_i$; axis x_{i5}, which is obtained by the rotation from axis x_{i4} around axis z_{i4} with the rotation angle of $\pi-\omega_1$, is along the direction of vector $\mathbf{A}_i\mathbf{O}_i\times\mathbf{O}_i\mathbf{D}_i$; axis z_{i6}, which is obtained by the rotation from axis z_{i5} around axis x_{i5} with the rotation angle of $-\alpha$, is along the direction of vector $\mathbf{D}_i\mathbf{O}_i$; frame f_{i7} is obtained by the translation from frame f_{i6} along vector $\mathbf{O}_i\mathbf{E}_i$; axis z_{i8}, which is obtained by the rotation from axis z_{i7} around axis x_{i7} with the rotation angle of $-\beta$, is along the direction of vector $\mathbf{E}_i\mathbf{A}_i$; axis x_{i9}, which is obtained by the rotation from axis x_{i8} around axis z_{i8} with the rotation angle of $\pi-\rho_2$, is along the direction of vector $\mathbf{A}_i\mathbf{E}_i\times\mathbf{E}_i\mathbf{B}_{i+1}$; axis z_{i10}, which is obtained by the rotation from axis z_{i9} around axis x_{i9} with the rotation angle of $-\beta$, is along the direction of vector $\mathbf{E}_i\mathbf{B}_{i+1}$; axis x_{i11}, which is obtained by the rotation from axis x_{i10} around axis z_{i10} with the rotation angle of $\pi-\rho_1$, is along the direction of vector $\mathbf{B}_{i+1}\mathbf{E}_i\times\mathbf{E}_i\mathbf{C}_{i+1}$; frame f_{i12} is obtained by the translation from frame f_{i11} along vector $\mathbf{E}_i\mathbf{B}_{i+1}$; axis x_{i13} is obtained by the rotation from axis x_{i12} around axis z_{i12} with the rotation angle of $-\omega_2/2$; and axis Z_{i+1} is obtained by the rotation from axis z_{i13} around axis X_{i+1} with the rotation angle of $-(\pi-\gamma)/2$ (if the rotation angle is negative, the rotation is clockwise; otherwise, the rotation is anticlockwise). The whole transformation process is summarized in Tab. 2-1.

Hence,

$$\begin{aligned}\boldsymbol{T}=&\boldsymbol{R}_x((\pi-\gamma)/2)\boldsymbol{R}_z(\pi-\omega_2/2)\boldsymbol{D}_z(a)\boldsymbol{R}_x(-\alpha)\boldsymbol{R}_z(\pi-\omega_1)\boldsymbol{R}_x(-\alpha)\\&\boldsymbol{D}_z(-a-a\sin\alpha/\tan\beta+a\cos\alpha)\boldsymbol{R}_x(-\beta)\boldsymbol{R}_z(\pi-\rho_2)\boldsymbol{R}_x(-\beta)\boldsymbol{R}_z(\pi-\rho_1)\\&\boldsymbol{D}_z((a\sin\alpha-a\cos\alpha\tan\beta)/\tan\beta)\boldsymbol{R}_z(-\omega_2/2)\boldsymbol{R}_x(-(\pi-\gamma)/2),\end{aligned}\tag{2-11}$$

where the rotation around axis x with an angle of δ is

$$\boldsymbol{R}_x(\delta)=\begin{bmatrix}1 & 0 & 0 & 0\\ 0 & \cos\delta & -\sin\delta & 0\\ 0 & \sin\delta & \cos\delta & 0\\ 0 & 0 & 0 & 1\end{bmatrix}; \tag{2-12a}$$

the rotation around axis z with an angle of λ is

$$\boldsymbol{R}_z(\lambda)=\begin{bmatrix}\cos\lambda & -\sin\lambda & 0 & 0\\ \sin\lambda & \cos\lambda & 0 & 0\\ 0 & 0 & 1 & 0\\ 0 & 0 & 0 & 1\end{bmatrix}; \tag{2-12b}$$

the translation along axis z with a distance of s is

$$\boldsymbol{D}_z(s)=\begin{bmatrix}1 & 0 & 0 & 0\\ 0 & 1 & 0 & 0\\ 0 & 0 & 1 & s\\ 0 & 0 & 0 & 1\end{bmatrix}; \tag{2-12c}$$

and

$$\rho_1=\pi-\omega_2; \tag{2-12d}$$

$$\tan(\rho_1/2)\tan(\rho_2/2)=1/\cos\beta. \tag{2-12e}$$

If frame F_1 is selected as the global frame, the expression of all points O_i in frame F_1 can be derived as

$$R=\left\|(\mathbf{p}_{i,1}-\mathbf{p}_1)\times\mathbf{s}\right\|, \tag{2-13}$$

where $\mathbf{p}_1$ represents the position vector of the intersection point of the major helical axis and the Y_1-B_1-Z_1 plane, and $\mathbf{s}$ is the normalized direction vector of the helical axis. By substituting Eqns. (2-10), (2-11) and (2-12) in Eqn. (2-13), the solution of R and $\mathbf{s}$ can be obtained.

To derive L and P, the distance between O_i and O_{i+1} along the major helical axis must be determined; thus, the chiral structure is rotated such that its helical axis is parallel to axis Z_1. In this case,

$$\begin{aligned}\mathbf{P}_i &= \boldsymbol{R}_x(\arccos(\sqrt{\mathbf{s}(1,1)^2+\mathbf{s}(3,1)^2}/\sqrt{\mathbf{s}(1,1)^2+\mathbf{s}(2,1)^2+\mathbf{s}(3,1)^2}))\\ &\quad \boldsymbol{R}_y(-\arctan(\mathbf{s}(1,1)/\mathbf{s}(3,1)))\mathbf{P}_{i,1},\end{aligned} \tag{2-14a}$$

$$\mathbf{P}_i=\begin{pmatrix}\mathbf{p}_i\\ 1\end{pmatrix}, \tag{2-14b}$$

where $\mathbf{s}(i,1)$ represents the element of vector $\mathbf{s}$ in the ith row, $\mathbf{p}_i$ is the position vector of point O_i after the rotation and

$$\boldsymbol{R}_{\mathrm{y}}(\tau)=\begin{bmatrix}\cos\tau & 0 & \sin\tau & 0\\ 0 & 1 & 0 & 0\\ -\sin\tau & 0 & \cos\tau & 0\\ 0 & 0 & 0 & 1\end{bmatrix}, \tag{2-15}$$

Next, it can be derived that the distance between O_i and O_{i+1} along the helical axis as

$$l=\mathbf{P}_{i+1}(3,1)-\mathbf{P}_i(3,1)=\mathbf{P}_2(3,1)-\mathbf{P}_1(3,1), \tag{2-16}$$

Projecting the major helix to its cross-section generates a circle whose centre is O and radius is R, as illustrated in Fig. 2-9(d) in which points O_i are located on the circle. The angle between OO_i and OO_{i+1} can be obtained as

$$\begin{aligned}\sin(\eta/2)&=\sqrt{\left(\mathbf{P}_{i+1}(1,1)-\mathbf{P}_i(1,1)\right)^2+\left(\mathbf{P}_{i+1}(2,1)-\mathbf{P}_i(2,1)\right)^2}/(2R)\\&=\sqrt{\left(\mathbf{P}_2(1,1)-\mathbf{P}_1(1,1)\right)^2+\left(\mathbf{P}_2(2,1)-\mathbf{P}_1(2,1)\right)^2}/(2R).\end{aligned} \tag{2-17}$$

According to the definition of P, K and L,

$$P=2\pi l/\eta, \tag{2-18a}$$

$$\tan K=2\pi R/P, \tag{2-18b}$$

$$L=Nl. \tag{2-18c}$$

The major and minor helices have identical chirality, although the chirality of the existing hierarchically chiral structures may be different. This aspect indicates that the chirality of our structure is dominated by its constituent units. However, the helical properties of the major and minor helices differ considerably. With the folding of the structure (i.e., as ϕ increases from 0° to 180°), the minor helix winds while the major helix unwinds; that is, the helical angle of the major helix decreases, and the helical angle of the minor helix (i.e. the angle between the minor helix and its axial line pertaining to the major helix, whose value is the same as that in the previous single RH chiral structure when ϕ is identical) increases, as indicated by the solid and dashed black lines in Fig. 2-10(a), respectively. Since the basic vertexes forming the major and minor helices are in the same chiral unit, the corresponding windings are coupled, in contrast to the existing hierarchically chiral structures, which exhibit independent winding. Moreover, in contrast with the single-helix case, which exhibits a monotonically decreasing pitch and unit length during winding, the pitch P and unit length $L/(Na)$ of the major helix first increase and later decrease, as shown in Fig. 2-10(b). The pitch P of the major helix first increases and later decreases, as shown in Fig. 2-10(c), Moreover, the radius R of the major helix is positively related to K (see Fig. 2-10(d)), whereas it is constant in the single-helix case. Furthermore, the results

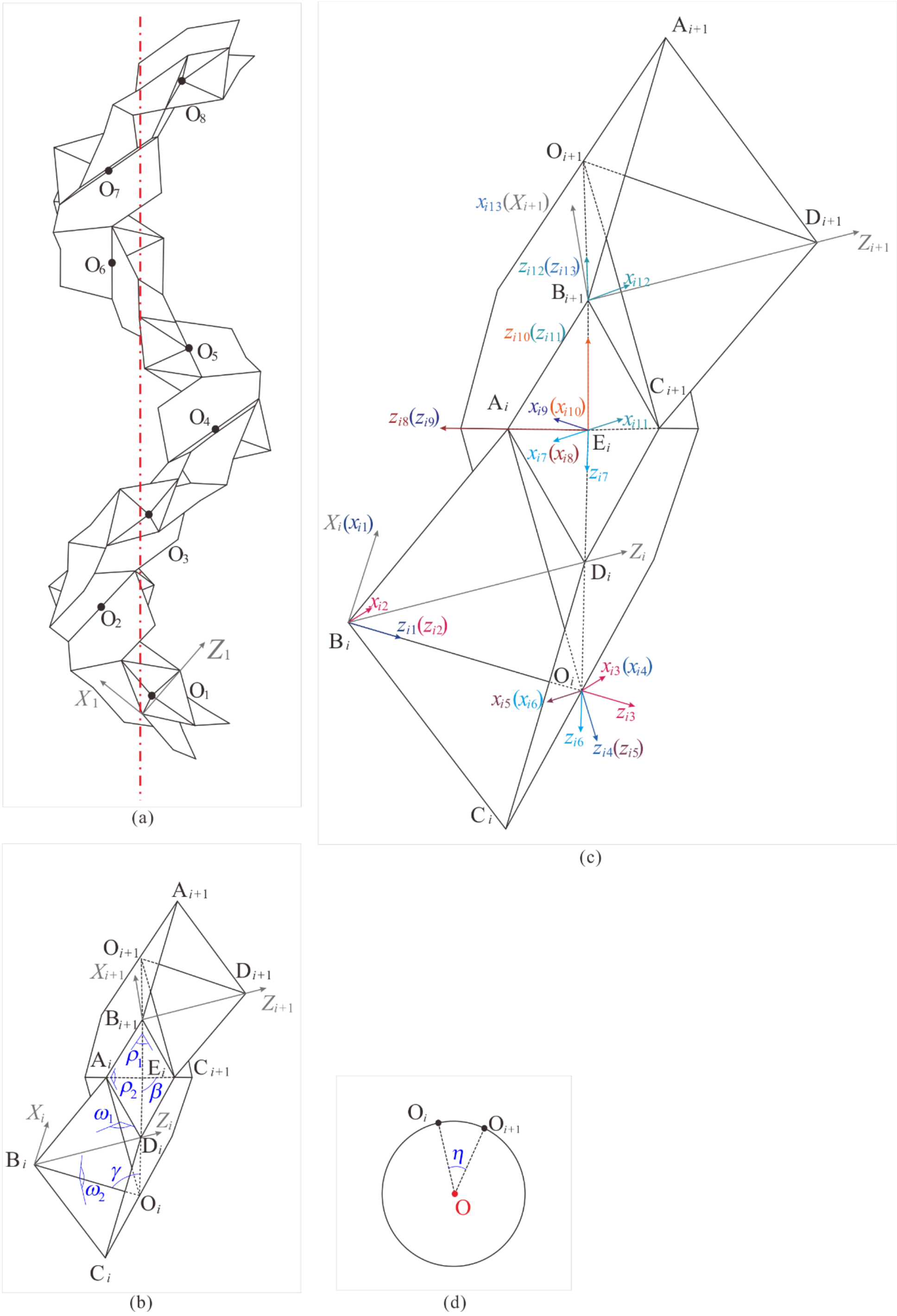

Fig. 2-9 Geometry of the hierarchically chiral structure: (a) a hierarchically chiral structure with $N=8$, where O_i (i=1 to 8) forms the major helix; (b) setup of the coordinate frames and geometrical parameters in two adjacent chiral units; (c) transition process of the frames between two adjacent chiral units; (d) projection of the major helix and points O_i and O_{i+1}

.

for the helices with three different values of β in Fig. 2-9 indicate that the helical properties of the major helix can be tuned through β. A more highly wound helix can be obtained if a larger β is selected, and more circles can be formed in a fully wound helix by adopting a larger β. Finally, increasing β leads to a reduction in the helix length; however, this effect is substantial only at relatively small helical angles.

Tab. 2-1 Transformation process from frame F_i to F_{i+1}

Step	From	Transformation method	Rotation around/ Translation along	Rotation angle/Translation distance	To	Target direction vector
1	Z_i	Rotation	X_i	$\frac{\pi-\gamma}{2}$	z_{i1}	$\mathbf{B}_i\mathbf{O}_i$
2	x_{i1}	Rotation	z_{i1}	$\pi-\frac{\omega_2}{2}$	x_{i2}	$\mathbf{A}_i\mathbf{B}_i \times \mathbf{B}_i\mathbf{O}_i$
3	f_{i2}	Translation	$\mathbf{B}_i\mathbf{O}_i$	a	f_{i3}	N/A
4	z_{i3}	Rotation	x_{i3}	$-\alpha$	z_{i4}	$\mathbf{A}_i\mathbf{O}_i$
5	x_{i4}	Rotation	z_{i4}	$\pi-\omega_1$	x_{i5}	$\mathbf{A}_i\mathbf{O}_i \times \mathbf{O}_i\mathbf{D}_i$
6	z_{i5}	Rotation	x_{i5}	$-\alpha$	z_{i6}	$\mathbf{D}_i\mathbf{O}_i$
7	f_{i6}	Translation	$\mathbf{O}_i\mathbf{E}_i$	$a\cos\alpha-\frac{a\sin\alpha}{\tan\beta}$ $+a$	f_{i7}	N/A
8	z_{i7}	Rotation	x_{i7}	$-\beta$	z_{i8}	$\mathbf{E}_i\mathbf{A}_i$
9	x_{i8}	Rotation	z_{i8}	$\pi-\rho_2$	x_{i9}	$\mathbf{A}_i\mathbf{E}_i \times \mathbf{E}_i\mathbf{B}_{i+1}$
10	z_{i9}	Rotation	x_{i9}	$-\beta$	z_{i10}	$\mathbf{E}_i\mathbf{B}_{i+1}$
11	x_{i10}	Rotation	z_{i10}	$\pi-\rho_1$	x_{i11}	$\mathbf{B}_{i+1}\mathbf{E}_i \times \mathbf{E}_i\mathbf{C}_{i+1}$
12	f_{i11}	Translation	$\mathbf{E}_i\mathbf{B}_{i+1}$	$\frac{a\sin\alpha}{\tan\beta}-a\cos\alpha$	f_{i12}	N/A
13	x_{i12}	Rotation	z_{i12}	$-\frac{\omega_2}{2}$	x_{i13}	X_{i+1}
14	z_{i13}	Rotation	X_{i+1}	$-\frac{\pi-\gamma}{2}$	Z_{i+1}	Z_{i+1}

2.6 Conclusions

Helical units and structures based on eggbox-shaped origami are proposed, the chirality of which can be tuned by adjusting the geometrical parameters. These structures can be used as a theoretical model to understand the mechanism of chirality in nature. For example, towel gourd tendrils gradually evolve into a helical shape with opposite handedness to allow the plant to climb to a sufficient height when attached to a supporting object, similar to our proposed achiral structure with internal twist, as shown in Fig. 2-2(d). Studying the movement of the developed model can enhance the understanding of the chiral growth mechanism of towel gourd tendrils. Switchable chirality was achieved through the bifurcation of kinematically equivalent linkages, which can allow the alteration of the on-sight optical or electromagnetic property of the metamaterial constructed from such helical units. Nevertheless, it may be challenging to manufacture a metamaterial with a large deformation to achieve the chirality switch in industrial applications. Moreover, I designed hierarchically chiral structures with major and minor helices at the same macroscale in which the winding of the minor helix drove the unwinding of the major helix. This unusual behaviour, resulting in two compact folding configurations, provides an opportunity to design multi-functional morphing structures in aerospace engineering applications. Furthermore, due to its single degree-of-freedom, the proposed chiral structures can be applied to bionic robots with a simple control system, which is a topic of our subsequent work.

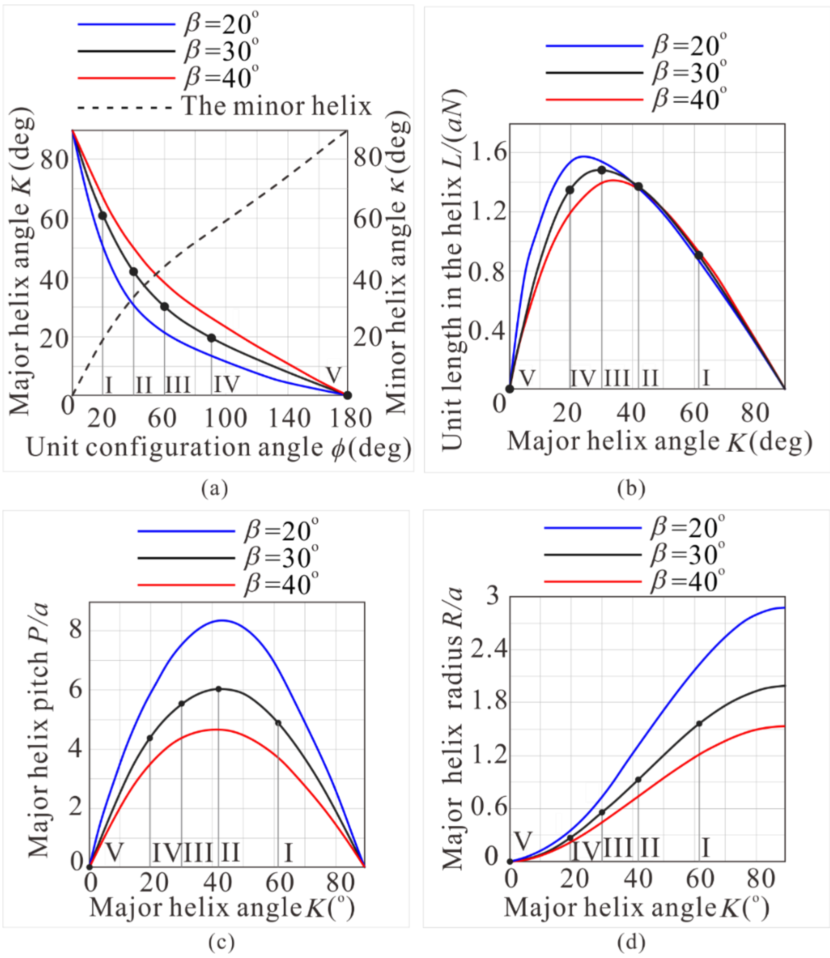

Figure 2-10 Effect of the sector angle β on the helical characteristics of the hierarchically chiral structure, where β is set as 20°, 30° and 40°: (a) relationship among K, κ, and ϕ; (b) relationship between the non-dimensional length of each chiral unit $L/(aN)$ and K; (c) relationship between the non-dimensional pitch P/a and K; (d) relationship between the non-dimensional major helix radius R/a.

Chapter 3 2D mobile networks of spherical linkages: morphing surfaces

3.1 Introduction

In the mechanical engineering domain, rigid origami is generally studied as a network system of spherical linkages. For a single vertex of a rigid origami structure, rigid links can be rotated around revolute joints during folding, and all the axes of the joints may intersect at a point. In this case, the single vertex can be regarded as a spherical linkage. I developed a novel form of a one-DOF network system of spherical 4*R* linkages by replacing the unit facets of a planar origami pattern with volumetric tetrahedrons. The altered form retained its original one-DOF characteristic, and the network could be expanded to a morphing surface. Thus, a morphing surface that could transform from a parabolic cylinder to a paraboloid through the motion of the spherical linkages is obtained.

The layout of this chapter is as follows. First, in Chapter 3.2, a novel one-DOF network system of spherical 4*R* linkages inspired by origami is described. The above-mentioned network system is extended to a morphing surface. Next, in Chapter 3.3, an example of the morphing surface that can transform from a parabolic cylinder to a paraboloid is presented. Finally, the concluding remarks are presented in Chapter 3.4.

3.2 Network system and morphing surface inspired by origami

Inspired by the famous eggbox origami pattern, a novel form of a one-DOF network system of spherical 4*R* linkages is established by replacing the unit facets of the eggbox pattern with volumetric tetrahedrons. An eggbox with four rhombic units is illustrated in Fig. 3-1(a) in which the dashed lines represent the crease patterns that cannot be observed from the view point, and the red lines are the two edges AB and AD of the rhombic unit ABCD connected to its neighbouring units. Folding the unit ABCD around the crease line BD with the dihedral angle ω yields a spatial quadrilateral. By adding an identical spatial quadrilateral, a tetrahedral unit is constructed. This process is shown in Fig. 3-1(b). It can be noted that

$$\cos\omega = (\cos\alpha - \cos^2((\pi-\alpha)/2)/\sin^2((\pi-\alpha)/2). \qquad (3\text{-}1)$$

Figure 3-1(c) shows the oblique, top and bottom views of the assembly of four tetrahedral units, which can be regarded as a spherical 4*R* linkage. By connecting the three above-mentioned assemblies in series and adding planar triangle units, the mobile network shown in the left part of Fig. 3-1(d) is achieved in which the triangle units are shown in white. The paper model of the mobile network is shown in Fig. 3-1(d) left in which the blue and white parts denote the tetrahedrons and planar triangle units, respectively. This network is a one-DOF assembly of spherical 4*R* linkages.

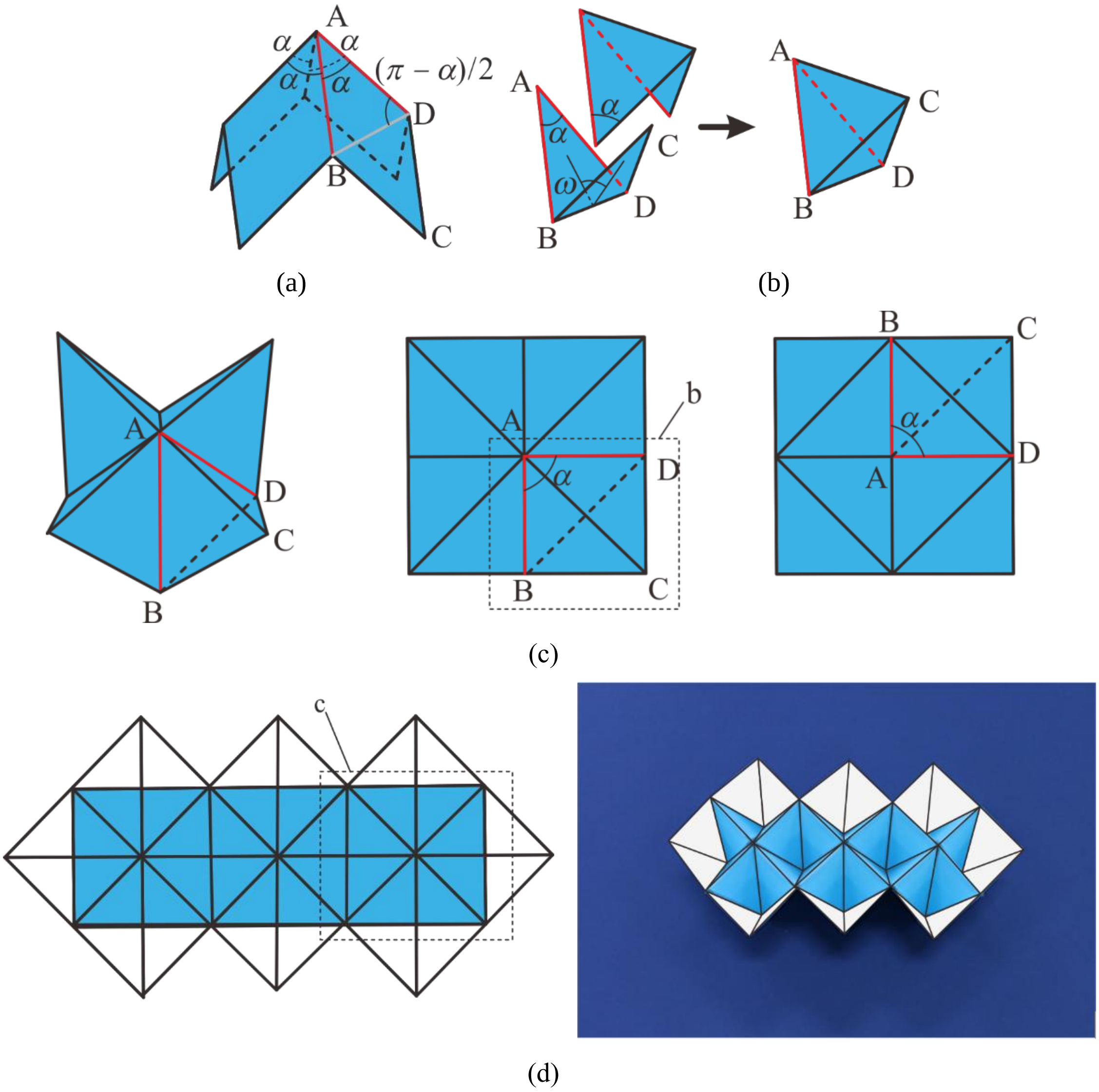

Fig. 3-1 One-DOF network inspired by rigid origami: (a) vertex of the eggbox pattern; (b) construction of a tetrahedral unit; (c) assembly of four tetrahedral units and (d) one-DOF mobile network.

The above-mentioned 4*R* configuration can be expanded to a one-DOF morphing surface profile by inserting more triangle units into the original network system. The simplest network is illustrated in Fig. 3-2, in which the blue and white parts represent tetrahedrons and triangle units, respectively.

By tuning the design parameters of the tetrahedrons and triangle units, different surfaces can be obtained. Although the planar units can be arbitrary triangles, for the sake of simplicity, three kinds of triangle units are used in the morphing surface shown in Fig. 3-3. As illustrated in Fig. 3-3 (a), panels with the same colour represent the same kind of triangle unit and the surface is two-fold symmetric. The tetrahedrons (blue part in the middle of the network) are formed by identical isosceles triangles (Fig. 3-3(b), left), with the length of the equal sides being L; the yellow and green triangles are isosceles triangles, with the length of the equal sides being L (Fig. 3-3(b), triangles in the middle and right). In this manner, a two-fold symmetric morphing surface can be obtained. If each triangle and tetrahedral unit is regarded as a link, three types of vertexes in the mobile network and different types of vertexes (considering vertexes A, I and C as an example, illustrated in Fig. 3-3(a)) are shown in Fig. 3-3(c) in which vertex A can be regarded as a spherical 4R linkage, and vertexes I and C can be regarded as spherical 6R and 8R linkages, respectively.

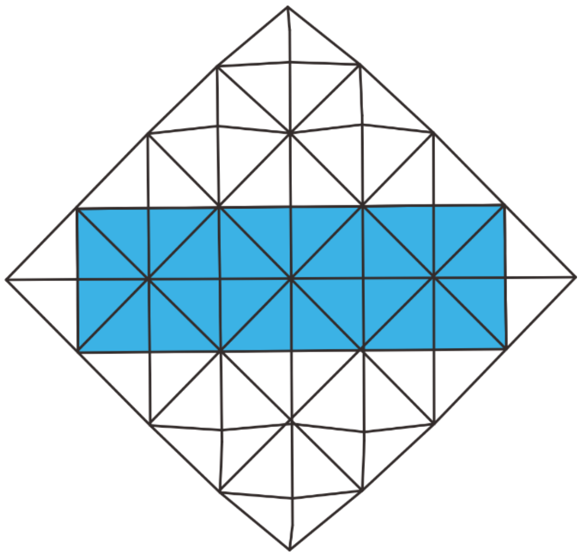

Fig. 3-2 Schematic of a morphing surface.

Subsequently, the relationship among the parameters at different vertexes is analyzed. For linkage A,

$$\alpha_{12}^{\mathrm{A}} = \alpha_{23}^{\mathrm{A}} = \alpha_{34}^{\mathrm{A}} = \alpha_{41}^{\mathrm{A}} = \alpha_1. \tag{3-2}$$

Substituting Eqn. (3-2) in Eqn. (1-7a) yields

$$\begin{aligned}
&\sin^2\alpha_1\cos\alpha_1\cos\theta_i^{\mathrm{A}} + \sin^2\alpha_1\cos\alpha_1\cos\theta_{i+1}^{\mathrm{A}} \\
&+\cos\alpha_1\sin^2\alpha_1\cos\theta_i^{\mathrm{A}}\cos\theta_{i+1}^{\mathrm{A}} \\
&-\sin{\alpha^2}_1\sin\theta_i^{\mathrm{A}}\sin\theta_{i+1}^{\mathrm{A}} - \cos^3\alpha_1 + \cos\alpha_1 = 0,
\end{aligned} \tag{3-3}$$

which can be expressed as

$$\theta_{i+1}^{\mathrm{A}} = f(\theta_i^{\mathrm{A}}). \tag{3-4}$$

For linkage I, which is a spherical 6R linkage, according to Eqns. (1-4) to (1-6),

$$\mathbf{Q}_{21}\mathbf{Q}_{32}\mathbf{Q}_{43}\mathbf{Q}_{54}\mathbf{Q}_{65}\mathbf{Q}_{16} = \boldsymbol{I}_3, \tag{3-5}$$

which can be expressed as

$$\mathbf{Q}_{21}\mathbf{Q}_{32}\mathbf{Q}_{43} = \mathbf{Q}_{61}\mathbf{Q}_{56}\mathbf{Q}_{45}. \tag{3-6}$$

In linkage I, the sector angles are

$$\alpha_{12}^{\mathrm{I}} = \alpha_{61}^{\mathrm{I}} = \alpha_1, \alpha_{23}^{\mathrm{I}} = \alpha_{56}^{\mathrm{I}} = \pi - 2\alpha_2, \alpha_{34}^{\mathrm{I}} = \alpha_{45}^{\mathrm{I}} = \alpha_3. \tag{3-7}$$

Substituting Eqn. (3-7) in Eqn. (3-6) yields

$$\begin{aligned}
&(\sin\alpha_1 \sin\theta_2^{\mathrm{I}} \sin\theta_3^{\mathrm{I}} + \sin\alpha_1 \cos 2\alpha_2 \cos\theta_2^{\mathrm{I}} \cos\theta_3^{\mathrm{I}} - \cos\alpha_1 \sin 2\alpha_2 \cos\theta_3^{\mathrm{I}}) \sin\alpha_3 \\
&-(\sin\alpha_1 \sin 2\alpha_2 \cos\theta_2^{\mathrm{I}} + \cos\alpha_1 \cos 2\alpha_2) \cos\alpha_3 \\
&= (\sin\alpha_1 \sin\theta_5^{\mathrm{I}} \sin\theta_6^{\mathrm{I}} + \sin\alpha_1 \cos 2\alpha_2 \cos\theta_5^{\mathrm{I}} \cos\theta_6^{\mathrm{I}} - \cos\alpha_1 \sin 2\alpha_2 \cos\theta_5^{\mathrm{I}}) \sin\alpha_3 \\
&-(\sin\alpha_1 \sin 2\alpha_2 \cos\theta_6^{\mathrm{I}} + \cos\alpha_1 \cos 2\alpha_2) \cos\alpha_3,
\end{aligned} \tag{3-8a}$$

$$\begin{aligned}
&(\cos\theta_1^{\mathrm{I}} \cos\theta_2^{\mathrm{I}} - \cos\alpha_1 \sin\theta_1^{\mathrm{I}} \sin\theta_2^{\mathrm{I}}) \cos\theta_3^{\mathrm{I}} \\
&+(\cos 2\alpha_2 \cos\theta_1^{\mathrm{I}} \sin\theta_2^{\mathrm{I}} + \cos\alpha_1 \cos 2\alpha_2 \sin\theta_1^{\mathrm{I}} \cos\theta_2^{\mathrm{I}} + \sin\alpha_1 \sin 2\alpha_2 \sin\theta_1^{\mathrm{I}}) \sin\theta_3^{\mathrm{I}} \\
&= (\cos\theta_5^{\mathrm{I}} \cos\theta_6^{\mathrm{I}} + \cos 2\alpha_2 \sin\theta_5^{\mathrm{I}} \sin\theta_6^{\mathrm{I}}) \cos\theta_4^{\mathrm{I}} \\
&-(\cos\alpha_3 \sin\theta_5^{\mathrm{I}} \cos\theta_6^{\mathrm{I}} - \cos 2\alpha_2 \cos\alpha_3 \cos\theta_5^{\mathrm{I}} \sin\theta_6^{\mathrm{I}} + \sin 2\alpha_2 \sin\alpha_3 \sin\theta_6^{\mathrm{I}}) \sin\theta_4^{\mathrm{I}},
\end{aligned} \tag{3-8b}$$

$$\begin{aligned}
&(\sin\theta_1^{\mathrm{I}} \cos\theta_2^{\mathrm{I}} + \cos\alpha_1 \cos\theta_1^{\mathrm{I}} \sin\theta_2^{\mathrm{I}}) \sin\alpha_3 \sin\theta_3^{\mathrm{I}} \\
&-(\cos 2\alpha_2 \sin\theta_1^{\mathrm{I}} \sin\theta_2^{\mathrm{I}} - \cos\alpha_1 \cos 2\alpha_2 \cos\theta_1^{\mathrm{I}} \cos\theta_2^{\mathrm{I}} - \sin\alpha_1 \sin 2\alpha_2 \cos\theta_1^{\mathrm{I}}) \sin\alpha_3 \cos\theta_3^{\mathrm{I}} \\
&+(\sin 2\alpha_2 \sin\theta_1^{\mathrm{I}} \sin\theta_2^{\mathrm{I}} - \cos\alpha_1 \sin 2\alpha_2 \cos\theta_1^{\mathrm{I}} \cos\theta_2^{\mathrm{I}} + \sin\alpha_1 \cos 2\alpha_2 \cos\theta_1^{\mathrm{I}}) \cos\alpha_3 \\
&= (-\cos\alpha_1 \sin\theta_5^{\mathrm{I}} \sin\theta_6^{\mathrm{I}} - \cos\alpha_1 \cos 2\alpha_2 \cos\theta_5^{\mathrm{I}} \cos\theta_6^{\mathrm{I}} + \sin\alpha_1 \sin 2\alpha_2 \cos\theta_5^{\mathrm{I}}) \sin\alpha_3 \\
&+(\cos\alpha_1 \sin 2\alpha_2 \cos\theta_6^{\mathrm{I}} - \sin\alpha_1 \cos 2\alpha_2) \cos\alpha_3.
\end{aligned} \tag{3-8c}$$

Equation (3-8) can be simplified as

$$\begin{aligned}
\theta_3^{\mathrm{I}} &= f_3^{\mathrm{I}}(\theta_1^{\mathrm{I}}, \theta_3^{\mathrm{I}}, \theta_6^{\mathrm{I}}), \\
\theta_4^{\mathrm{I}} &= f_4^{\mathrm{I}}(\theta_1^{\mathrm{I}}, \theta_2^{\mathrm{I}}, \theta_6^{\mathrm{I}}), \\
\theta_5^{\mathrm{I}} &= f_5^{\mathrm{I}}(\theta_1^{\mathrm{I}}, \theta_2^{\mathrm{I}}, \theta_6^{\mathrm{I}}).
\end{aligned} \tag{3-9}$$

In linkage C,

$$\boldsymbol{Q}_{21}\boldsymbol{Q}_{32}\boldsymbol{Q}_{43}\boldsymbol{Q}_{54}\boldsymbol{Q}_{65}\boldsymbol{Q}_{76}\boldsymbol{Q}_{87}\boldsymbol{Q}_{18} = \boldsymbol{I}_3, \tag{3-10}$$

which can be expressed as

$$\boldsymbol{Q}_{21}\boldsymbol{Q}_{32}\boldsymbol{Q}_{43}\boldsymbol{Q}_{54} = \boldsymbol{Q}_{81}\boldsymbol{Q}_{78}\boldsymbol{Q}_{67}\boldsymbol{Q}_{56}. \tag{3-11}$$

In linkage C, the sector angles are

$$\alpha_{12}^{\mathrm{C}} = \alpha_{81}^{\mathrm{C}} = \alpha_2, \alpha_{23}^{\mathrm{C}} = \alpha_{78}^{\mathrm{C}} = \pi - 2\alpha_3, \alpha_{34}^{\mathrm{C}} = \alpha_{67}^{\mathrm{C}} = \pi - 2\alpha_2, \alpha_{45}^{\mathrm{C}} = \alpha_{56}^{\mathrm{C}} = \alpha_3. \tag{3-12}$$

Merging Eqns. (3-11) and (3-12) yields

$$\begin{aligned}
\theta_4^{\mathrm{C}} &= f_4^{\mathrm{C}}(\theta_1^{\mathrm{C}}, \theta_2^{\mathrm{C}}, \theta_3^{\mathrm{C}}, \theta_7^{\mathrm{C}}, \theta_8^{\mathrm{C}}), \\
\theta_5^{\mathrm{C}} &= f_5^{\mathrm{C}}(\theta_1^{\mathrm{C}}, \theta_2^{\mathrm{C}}, \theta_3^{\mathrm{C}}, \theta_7^{\mathrm{C}}, \theta_8^{\mathrm{C}}), \\
\theta_6^{\mathrm{C}} &= f_6^{\mathrm{C}}(\theta_1^{\mathrm{C}}, \theta_2^{\mathrm{C}}, \theta_3^{\mathrm{C}}, \theta_7^{\mathrm{C}}, \theta_8^{\mathrm{C}}).
\end{aligned} \tag{3-13}$$

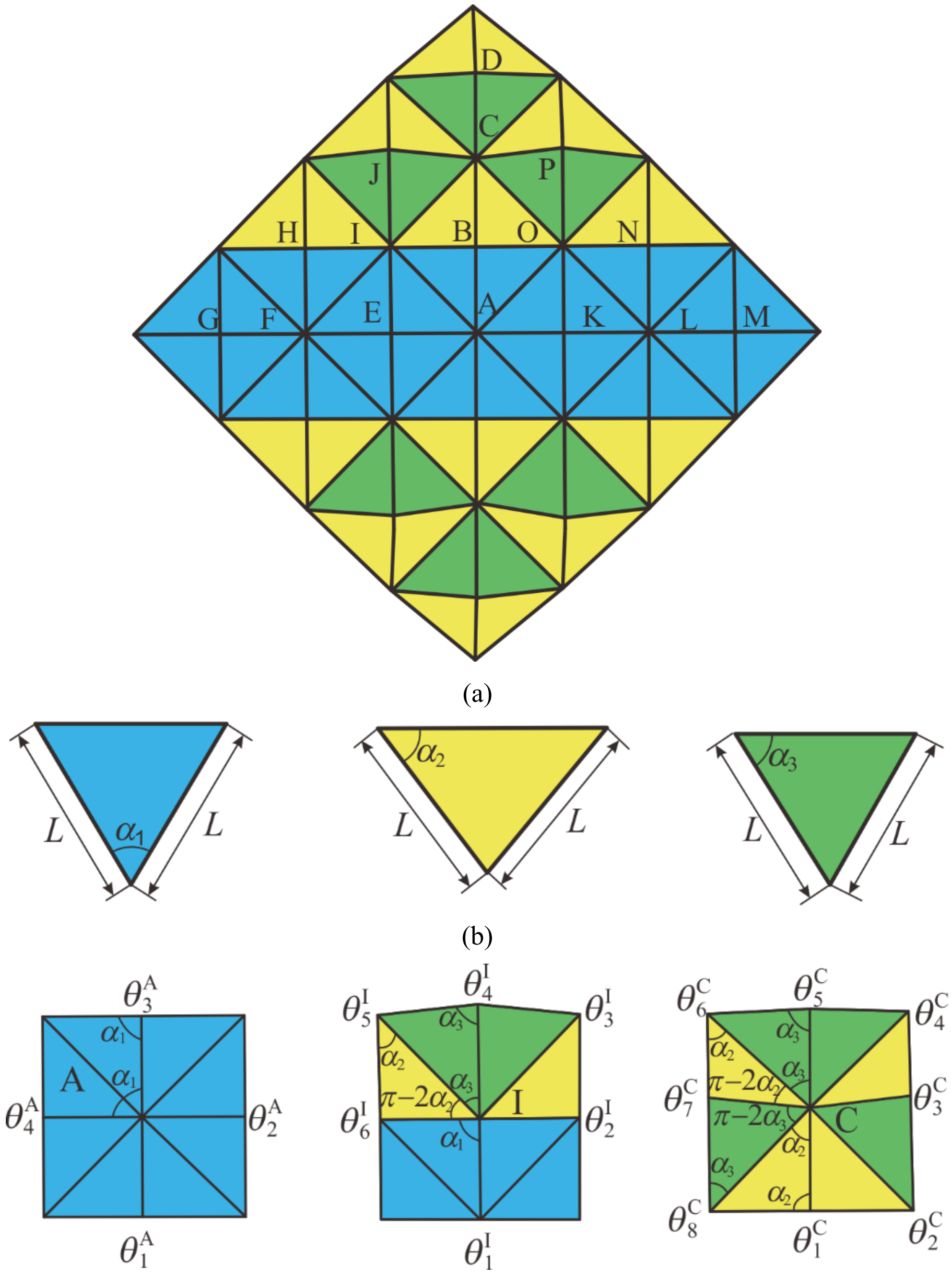

Fig. 3-3 Geometry of the morphing surface: (a) morphing surface with three kinds of triangle units; (b) three kinds of triangle units; (c) four kinds of vertexes in the morphing surface.

Since the morphing surface is symmetric, only half of the surface is considered. The relationship among the twist angles of half the mobile network is shown in Fig. 3-4. The twist angle at the end of an arrow can be obtained from the angle at the beginning of the arrow.

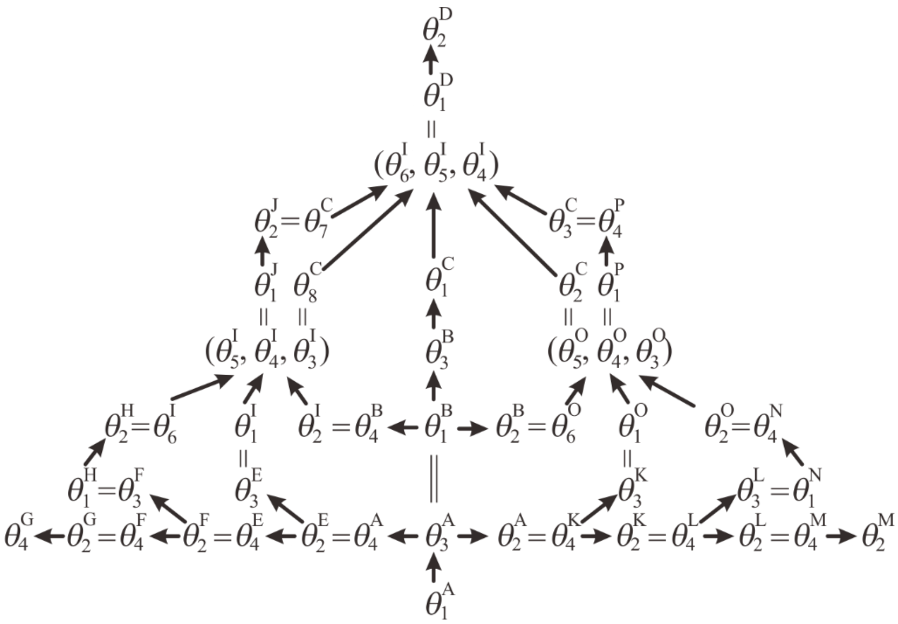

Fig. 3-4 Relationships among the parameters in the morphing surface.

For example, $\theta_3^{\mathrm{A}} \rightarrow \theta_4^{\mathrm{A}}$ represents $\theta_4^{\mathrm{A}} = f(\theta_3^{\mathrm{A}})$, which can be obtained from Eqn. (3-4). Vertexes I and O are regarded as spherical 6*R* linkages, which are three-DOF and can be determined by three input angles, which are determined according to the adjacent spherical 4*R* linkages; vertex C is regarded as a spherical 8*R* linkage, which requires five input angles to be determined, which are identified through linkages B, I, J, O and P. If angle θ_2^{D} is considered as the output angle of the mobile network, the output angle θ_2^{D} can be obtained even if only one input, angle θ_1^{A}, is given. Hence, the morphing surface has only one-DOF.

3.3 Transformation from a parabolic cylinder to a paraboloid

The morphing surface can transform between two target surfaces, and as described in this chapter, a morphing surface that can transform from a parabolic cylinder to a paraboloid is designed. A morphing surface constructed using isosceles triangle units has two zig-zag lines known as the “shape-lines” in which the H- and V-lines correspond to the horizontal and vertical shape-lines, respectively, constructed by connecting the vertexes in the two diagonal lines of the surface.

The two shape-lines of the arbitrary morphing surface match the two curved lines, as illustrated in Fig. 3-5. These two curved lines determine the shape of the morphing surface.

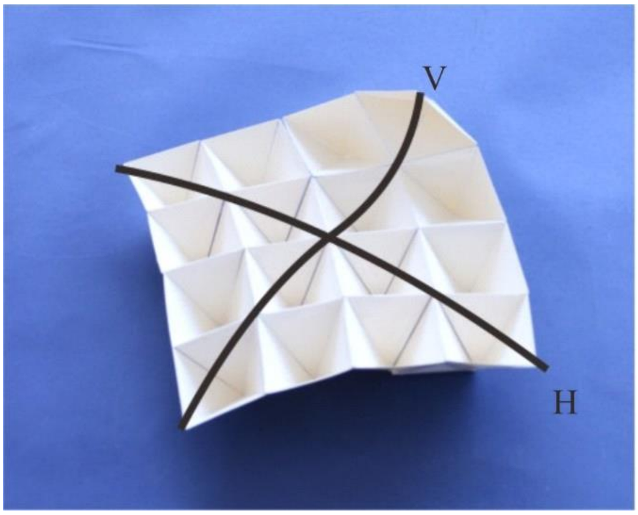

Fig. 3-5 Two curved lines matched by the two shape-lines of a morphing surface.

While designing a morphing surface, I focus only on the vertexes at the shape-lines. Assuming that the morphing surface is two-fold symmetric with respect to its shape-lines (see Fig. 3-6(a)), only a quarter of the network needs to be determined. The parameters of the morphing network and vertexes in the two shape-lines are shown in Fig. 3-6(b); in contrast to the network shown in Fig. 3-3, six different triangle units are used to construct the network, and the two shape-lines of the network are shown in Fig. 3-6(c) in which γ_i and ϕ_i are angles that determine the two shape-lines of the morphing surface. Two coordinate frames are established in both the shape-lines. For each shape-line, the x-axis is horizontal, the y-axis is perpendicular to the x-axis, and vertex O is the origin of coordinates in both the frames. By obtaining the coordinates of the vertexes in the two shape-lines, the two shape-lines can be defined.

The shape of the morphing surface can be determined by the two shape-lines, and to obtain the angles γ_i and ϕ_i, coordinate systems are established at the vertexes in the shape-lines. The coordinate frame of vertex V_2 considered as an example is shown in Fig. 3-7. Linkage V_2 is plane-symmetric in which $\mathbf{a}_i^{V_2}$ represents the direction vector of the ith crease line of the spherical 8R linkage, $\mathbf{n}_i^{V_2}$ represents the direction vector of $\mathbf{a}_i^{V_2} \times \mathbf{a}_{i+1}^{V_2}$ and $\omega_i^{V_2}$ represents the dihedral angle between the two triangle units pertaining to vector $\mathbf{a}_i^{V_2}$ (for the sake of simplicity, only $\mathbf{n}_1^{V_2}$, $\mathbf{n}_2^{V_2}$, $\omega_1^{V_2}$ and $\omega_2^{V_2}$ are illustrated in Fig. 3-7). The angle between $\mathbf{n}_i^{V_2}$ and $\mathbf{n}_{i+1}^{V_2}$ is $(\pi - \omega_{i+1}^{V_2})$. The x-V_2-y plane of the coordinate system is determined by $\mathbf{a}_1^{V_2}$ and $\mathbf{a}_8^{V_2}$.The x-axis is along the downward direction of the bisector of the angle between vectors $\mathbf{a}_1^{V_2}$ and $\mathbf{a}_8^{V_2}$; the y-axis is perpendicular to the x-axis and along the right direction. For vertex

V$_2$, the angle between $\mathbf{a}_1^{V_2}$ and $\mathbf{a}_5^{V_2}$ should be obtained, and this angle is ϕ_2. For all vertexes in the two shape-lines,

$$\begin{aligned}
&\mathbf{a}_2^{\mathrm{O}} = \left(\cos(<\mathbf{a}_4^{\mathrm{O}},\mathbf{a}_2^{\mathrm{O}}>/2),\sin(<\mathbf{a}_4^{\mathrm{O}},\mathbf{a}_2^{\mathrm{O}}>/2),0\right)^{\mathrm{T}},\\
&\mathbf{a}_2^{\mathrm{V}_1} = \left(\cos(<\mathbf{a}_4^{\mathrm{V}_1},\mathbf{a}_2^{\mathrm{V}_1}>/2),\sin(<\mathbf{a}_4^{\mathrm{V}_1},\mathbf{a}_2^{\mathrm{V}_1}>/2),0\right)^{\mathrm{T}},\\
&\mathbf{a}_2^{\mathrm{V}_2} = \left(\cos(<\mathbf{a}_8^{\mathrm{V}_2},\mathbf{a}_2^{\mathrm{V}_2}>/2),\sin(<\mathbf{a}_8^{\mathrm{V}_2},\mathbf{a}_2^{\mathrm{V}_2}>/2),0\right)^{\mathrm{T}},\\
&\mathbf{a}_2^{\mathrm{V}_3} = \left(\cos(<\mathbf{a}_4^{\mathrm{V}_3},\mathbf{a}_2^{\mathrm{V}_3}>/2),\sin(<\mathbf{a}_4^{\mathrm{V}_3},\mathbf{a}_2^{\mathrm{V}_3}>/2),0\right)^{\mathrm{T}},\\
&\mathbf{a}_2^{\mathrm{H}_j} = \left(\cos(<\mathbf{a}_4^{\mathrm{H}_j},\mathbf{a}_2^{\mathrm{H}_j}>/2),\sin(<\mathbf{a}_4^{\mathrm{H}_j},\mathbf{a}_2^{\mathrm{H}_j}>/2),0\right)^{\mathrm{T}},\\
&\mathbf{a}_2^{\mathrm{A}} = \left(\cos(<\mathbf{a}_4^{\mathrm{A}},\mathbf{a}_2^{\mathrm{A}}>/2),\sin(<\mathbf{a}_4^{\mathrm{A}},\mathbf{a}_2^{\mathrm{A}}>/2),0\right)^{\mathrm{T}},\\
&\mathbf{a}_2^{\mathrm{B}} = \left(\cos(<\mathbf{a}_4^{\mathrm{B}},\mathbf{a}_2^{\mathrm{B}}>/2),\sin(<\mathbf{a}_4^{\mathrm{B}},\mathbf{a}_2^{\mathrm{B}}>/2),0\right)^{\mathrm{T}},\\
&\mathbf{a}_2^{\mathrm{C}} = \left(\cos(<\mathbf{a}_4^{\mathrm{C}},\mathbf{a}_2^{\mathrm{C}}>/2),\sin(<\mathbf{a}_4^{\mathrm{C}},\mathbf{a}_2^{\mathrm{C}}>/2),0\right)^{\mathrm{T}},
\end{aligned} \tag{3-14a}$$

$$\begin{aligned}
&\mathbf{a}_{i-1}^{\mathrm{O}}\cdot\mathbf{n}_i^{\mathrm{O}}=0,\mathbf{a}_{i-1}^{\mathrm{V}_j}\cdot\mathbf{n}_i^{\mathrm{V}_j}=0,\mathbf{a}_{i-1}^{\mathrm{H}_j}\cdot\mathbf{n}_i^{\mathrm{H}_j}=0,\mathbf{a}_{i-1}^{\mathrm{A}}\cdot\mathbf{n}_i^{\mathrm{A}}=0,\mathbf{a}_{i-1}^{\mathrm{B}}\cdot\mathbf{n}_i^{\mathrm{B}}=0,\mathbf{a}_{i-1}^{\mathrm{C}}\cdot\mathbf{n}_i^{\mathrm{C}}=0,\mathbf{a}_{i-1}^{\mathrm{C}}\cdot\mathbf{n}_i^{\mathrm{C}}=0,\\
&\mathbf{a}_i^{\mathrm{O}}\cdot\mathbf{n}_i^{\mathrm{O}}=0,\mathbf{a}_i^{\mathrm{V}_j}\cdot\mathbf{n}_i^{\mathrm{V}_j}=0,\mathbf{a}_i^{\mathrm{H}_j}\cdot\mathbf{n}_i^{\mathrm{H}_j}=0,\mathbf{a}_i^{\mathrm{A}}\cdot\mathbf{n}_i^{\mathrm{A}}=0,\mathbf{a}_i^{\mathrm{B}}\cdot\mathbf{n}_i^{\mathrm{B}}=0,\mathbf{a}_i^{\mathrm{C}}\cdot\mathbf{n}_i^{\mathrm{C}}=0,
\end{aligned} \tag{3-14b}$$

$$\begin{aligned}
&\cos<\mathbf{a}_{i-1}^{\mathrm{O}},\mathbf{a}_i^{\mathrm{O}}>=(\mathbf{a}_{i-1}^{\mathrm{O}}\cdot\mathbf{a}_i^{\mathrm{O}})/(\|\mathbf{a}_{i-1}^{\mathrm{O}}\|\|\mathbf{a}_i^{\mathrm{O}}\|),\cos<\mathbf{a}_{i-1}^{\mathrm{V}_j},\mathbf{a}_i^{\mathrm{V}_j}>=(\mathbf{a}_{i-1}^{\mathrm{V}_j}\cdot\mathbf{a}_i^{\mathrm{V}_j})/(\|\mathbf{a}_{i-1}^{\mathrm{V}_j}\|\|\mathbf{a}_i^{\mathrm{V}_j}\|),\\
&\cos<\mathbf{a}_{i-1}^{\mathrm{H}_j},\mathbf{a}_i^{\mathrm{H}_j}>=(\mathbf{a}_{i-1}^{\mathrm{H}_j}\cdot\mathbf{a}_i^{\mathrm{H}_j})/(\|\mathbf{a}_{i-1}^{\mathrm{H}_j}\|\|\mathbf{a}_i^{\mathrm{H}_j}\|),\cos<\mathbf{a}_{i-1}^{\mathrm{A}},\mathbf{a}_i^{\mathrm{A}}>=(\mathbf{a}_{i-1}^{\mathrm{A}}\cdot\mathbf{a}_i^{\mathrm{A}})/(\|\mathbf{a}_{i-1}^{\mathrm{A}}\|\|\mathbf{a}_i^{\mathrm{A}}\|),\\
&\cos<\mathbf{a}_{i-1}^{\mathrm{B}},\mathbf{a}_i^{\mathrm{B}}>=(\mathbf{a}_{i-1}^{\mathrm{B}}\cdot\mathbf{a}_i^{\mathrm{B}})/(\|\mathbf{a}_{i-1}^{\mathrm{B}}\|\|\mathbf{a}_i^{\mathrm{B}}\|),\cos<\mathbf{a}_{i-1}^{\mathrm{C}},\mathbf{a}_i^{\mathrm{C}}>=(\mathbf{a}_{i-1}^{\mathrm{C}}\cdot\mathbf{a}_i^{\mathrm{C}})/(\|\mathbf{a}_{i-1}^{\mathrm{C}}\|\|\mathbf{a}_i^{\mathrm{C}}\|),
\end{aligned} \tag{3-14c}$$

$$\begin{aligned}
&\cos<\mathbf{n}_{i-1}^{\mathrm{O}},\mathbf{n}_i^{\mathrm{O}}>=-\cos\omega_{i-1}^{\mathrm{O}},\cos<\mathbf{n}_{i-1}^{\mathrm{V}_j},\mathbf{n}_i^{\mathrm{V}_j}>=-\cos\omega_{i-1}^{\mathrm{V}_j},\\
&\cos<\mathbf{n}_{i-1}^{\mathrm{H}_j},\mathbf{n}_i^{\mathrm{H}_j}>=-\cos\omega_{i-1}^{\mathrm{H}_j},\cos<\mathbf{n}_{i-1}^{\mathrm{A}},\mathbf{n}_i^{\mathrm{A}}>=-\cos\omega_{i-1}^{\mathrm{O}},\\
&\cos<\mathbf{n}_{i-1}^{\mathrm{B}},\mathbf{n}_i^{\mathrm{B}}>=-\cos\omega_{i-1}^{\mathrm{O}},\cos<\mathbf{n}_{i-1}^{\mathrm{C}},\mathbf{n}_i^{\mathrm{C}}>=-\cos\omega_{i-1}^{\mathrm{O}},
\end{aligned} \tag{3-14d}$$

$$\begin{aligned}
&\cos<\mathbf{a}_{i-2}^{\mathrm{O}},\mathbf{a}_i^{\mathrm{O}}>=\cos<\mathbf{a}_{i-2}^{\mathrm{O}},\mathbf{a}_{i-1}^{\mathrm{O}}>\cdot\cos<\mathbf{a}_{i-1}^{\mathrm{O}},\mathbf{a}_i^{\mathrm{O}}>\\
&+\sin<\mathbf{a}_{i-2}^{\mathrm{O}},\mathbf{a}_{i-1}^{\mathrm{O}}>\cdot\sin<\mathbf{a}_{i-1}^{\mathrm{O}},\mathbf{a}_i^{\mathrm{O}}>\cos\omega_{i-1}^{\mathrm{O}},\\
&\cos<\mathbf{a}_{i-2}^{\mathrm{V}_j},\mathbf{a}_i^{\mathrm{V}_j}>=\cos<\mathbf{a}_{i-2}^{\mathrm{V}_j},\mathbf{a}_{i-1}^{\mathrm{V}_j}>\cdot\cos<\mathbf{a}_{i-1}^{\mathrm{V}_j},\mathbf{a}_i^{\mathrm{V}_j}>\\
&+\sin<\mathbf{a}_{i-2}^{\mathrm{V}_j},\mathbf{a}_{i-1}^{\mathrm{V}_j}>\cdot\sin<\mathbf{a}_{i-1}^{\mathrm{V}_j},\mathbf{a}_i^{\mathrm{V}_j}>\cos\omega_{i-1}^{\mathrm{V}_j},\\
&\cos<\mathbf{a}_{i-2}^{\mathrm{H}_j},\mathbf{a}_i^{\mathrm{H}_j}>=\cos<\mathbf{a}_{i-2}^{\mathrm{H}_j},\mathbf{a}_{i-1}^{\mathrm{H}_j}>\cdot\cos<\mathbf{a}_{i-1}^{\mathrm{H}_j},\mathbf{a}_i^{\mathrm{H}_j}>\\
&+\sin<\mathbf{a}_{i-2}^{\mathrm{H}_j},\mathbf{a}_{i-1}^{\mathrm{H}_j}>\cdot\sin<\mathbf{a}_{i-1}^{\mathrm{H}_j},\mathbf{a}_i^{\mathrm{H}_j}>\cos\omega_{i-1}^{\mathrm{H}_j},
\end{aligned} \tag{3-14e}$$

$$
\begin{aligned}
&\cos < \mathbf{a}_{i-2}^{\mathrm{A}}, \mathbf{a}_{i}^{\mathrm{A}} >= \cos < \mathbf{a}_{i-2}^{\mathrm{A}}, \mathbf{a}_{i-1}^{\mathrm{A}} > \cdot \cos < \mathbf{a}_{i-1}^{\mathrm{A}}, \mathbf{a}_{i}^{\mathrm{A}} > \\
&+ \sin < \mathbf{a}_{i-2}^{\mathrm{A}}, \mathbf{a}_{i-1}^{\mathrm{A}} > \cdot \sin < \mathbf{a}_{i-1}^{\mathrm{A}}, \mathbf{a}_{i}^{\mathrm{A}} > \cos \omega_{i-1}^{\mathrm{A}}, \\
&\cos < \mathbf{a}_{i-2}^{\mathrm{B}}, \mathbf{a}_{i}^{\mathrm{B}} >= \cos < \mathbf{a}_{i-2}^{\mathrm{B}}, \mathbf{a}_{i-1}^{\mathrm{B}} > \cdot \cos < \mathbf{a}_{i-1}^{\mathrm{B}}, \mathbf{a}_{i}^{\mathrm{B}} > \\
&+ \sin < \mathbf{a}_{i-2}^{\mathrm{B}}, \mathbf{a}_{i-1}^{\mathrm{B}} > \cdot \sin < \mathbf{a}_{i-1}^{\mathrm{B}}, \mathbf{a}_{i}^{\mathrm{B}} > \cos \omega_{i-1}^{\mathrm{B}}, \\
&\cos < \mathbf{a}_{i-2}^{\mathrm{C}}, \mathbf{a}_{i}^{\mathrm{C}} >= \cos < \mathbf{a}_{i-2}^{\mathrm{C}}, \mathbf{a}_{i-1}^{\mathrm{C}} > \cdot \cos < \mathbf{a}_{i-1}^{\mathrm{C}}, \mathbf{a}_{i}^{\mathrm{C}} > \\
&+ \sin < \mathbf{a}_{i-2}^{\mathrm{C}}, \mathbf{a}_{i-1}^{\mathrm{C}} > \cdot \sin < \mathbf{a}_{i-1}^{\mathrm{C}}, \mathbf{a}_{i}^{\mathrm{C}} > \cos \omega_{i-1}^{\mathrm{C}},
\end{aligned}
\tag{3-14f}
$$

where $<\mathbf{a},\mathbf{b}>$ represents the angle between vectors $\mathbf{a}$ and $\mathbf{b}$. At each vertex, the relationship between the dihedral angle ω_i and twist angle θ_i is as follows:

$$
\begin{aligned}
&\omega_i = \pi - \theta_i \quad \text{(mountain crease line)}, \\
&\omega_i = \pi + \theta_i \quad \text{(valley crease line)}.
\end{aligned}
\tag{3-14g}
$$

According to Section 3.2, all the direction vectors $\mathbf{a}_i$ at each vertex can be derived from Eqns. (3-14a) to (3-14f) by defining the dihedral angle ω_1^{O}, through a similar process as that shown in Fig. 3-4.

After obtaining the direction vectors at each vertex in the two shape-lines, the coordinates of these vertexes in the frames shown in Fig. 3-6(c) can be derived. Specifically, the following equations can be obtained:

$$
\begin{aligned}
&\cos \gamma_0 = \cos < \mathbf{a}_2^{\mathrm{O}}, \mathbf{a}_4^{\mathrm{O}} >, \\
&\cos \gamma_1 = \cos < \mathbf{a}_2^{\mathrm{H}_1}, \mathbf{a}_4^{\mathrm{H}_1} >, \\
&\cos \gamma_2 = \cos < \mathbf{a}_2^{\mathrm{H}_2}, \mathbf{a}_4^{\mathrm{H}_2} >, \\
&\cos \gamma_3 = \cos < \mathbf{a}_2^{\mathrm{H}_3}, \mathbf{a}_4^{\mathrm{H}_3} >,
\end{aligned}
\tag{3-15a}
$$

$$
\begin{aligned}
&\cos \phi_0 = \cos < \mathbf{a}_1^{\mathrm{O}}, \mathbf{a}_3^{\mathrm{O}} >, \\
&\cos \phi_1 = \cos < \mathbf{a}_1^{\mathrm{V}_1}, \mathbf{a}_3^{\mathrm{V}_1} >, \\
&\cos \phi_2 = \cos < \mathbf{a}_1^{\mathrm{V}_2}, \mathbf{a}_5^{\mathrm{V}_2} >, \\
&\cos \phi_3 = \cos < \mathbf{a}_1^{\mathrm{V}_3}, \mathbf{a}_3^{\mathrm{V}_3} >,
\end{aligned}
\tag{3-15b}
$$

$$
\begin{aligned}
&\mathbf{p}_{\mathrm{O}} = (0,0)^{\mathrm{T}}, \\
&\mathbf{p}_{\mathrm{H}_1} = \mathbf{p}_{\mathrm{O}} + \left(L\cos(\pi/2 - \gamma_0/2), -L\sin(\pi/2 - \gamma_0/2)\right)^{\mathrm{T}}, \\
&\mathbf{p}_{\mathrm{H}_2} = \mathbf{p}_{\mathrm{H}_1} + \left(L\cos(\pi/2 - \gamma_1 + \gamma_0/2)), -L\sin(\pi/2 - \gamma_1 + \gamma_0/2))\right)^{\mathrm{T}}, \\
&\mathbf{p}_{\mathrm{H}_3} = \mathbf{p}_{\mathrm{H}_2} + \left(L\cos(\pi/2 - \gamma_2 + \gamma_1 - \gamma_0/2), -L\sin(\pi/2 - \gamma_2 + \gamma_1 - \gamma_0/2)\right)^{\mathrm{T}}, \\
&\mathbf{p}_{\mathrm{H}_4} = \mathbf{p}_{\mathrm{H}_3} + \left(L\cos(\pi/2 - \gamma_3 + \gamma_2 - \gamma_1 + \gamma_0/2), -L\sin(\pi/2 - \gamma_3 + \gamma_2 - \gamma_1 + \gamma_0/2)\right)^{\mathrm{T}},
\end{aligned}
\tag{3-15c}
$$

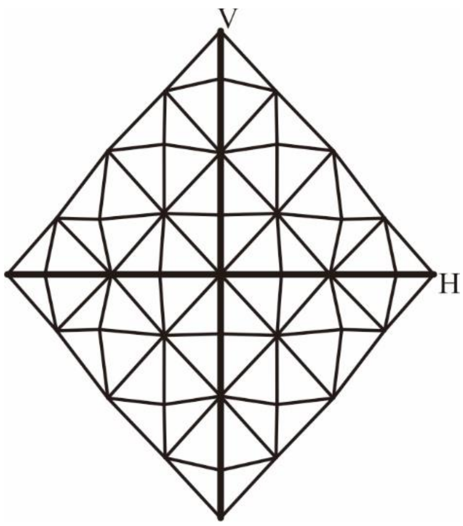

(a)

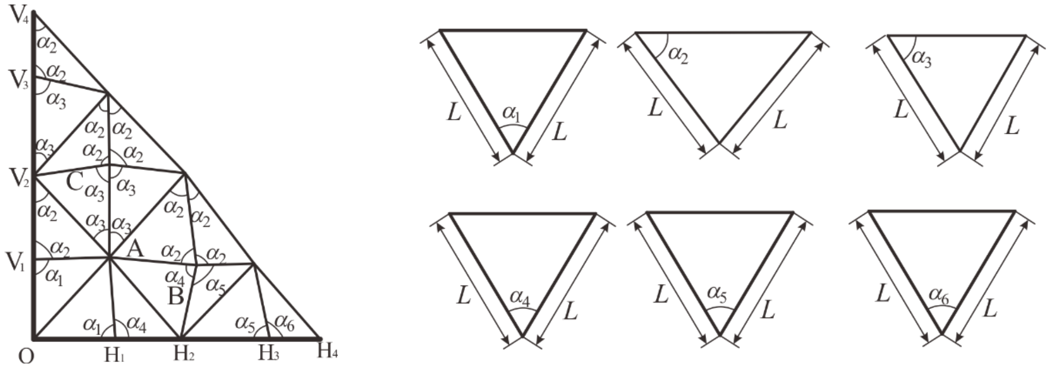

(b)

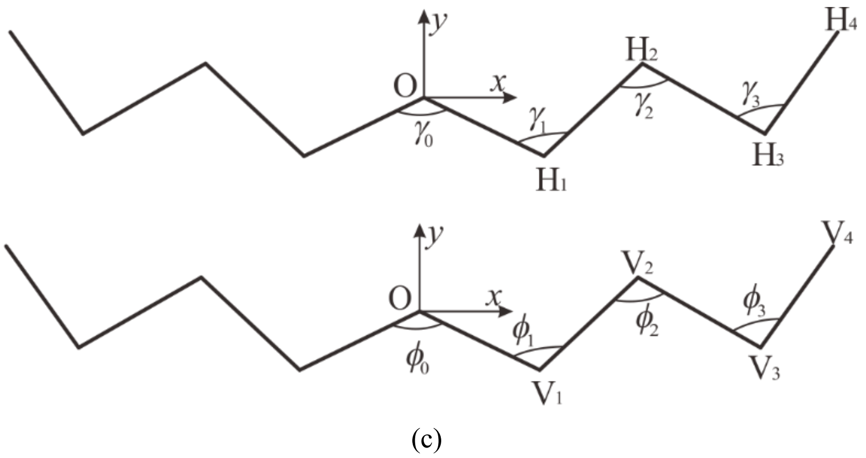

(c)

Fig. 3-6 Morphing surface: (a) network; (b) parameters of the network; (c) two shape-lines: H-line (top) and V-line (bottom).

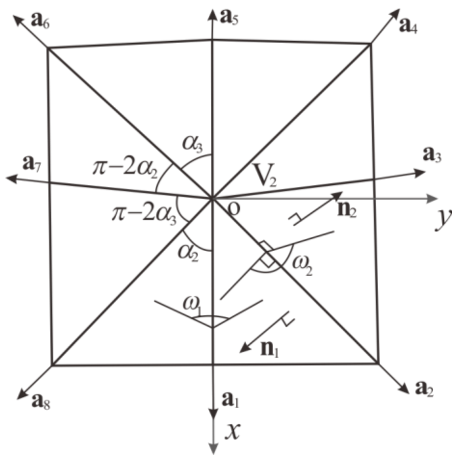

Fig. 3-7 Coordinate frame at vertex V_2.

$$
\begin{aligned}
&\mathbf{p}_{V_1} = \mathbf{p}_O + \left(L\cos(\pi/2-\phi_0/2), -L\sin(\pi/2-\phi_0/2)\right)^T,\\
&\mathbf{p}_{V_2} = \mathbf{p}_{V_1} + \left(2L\cos\alpha_2\cos(\pi/2-\gamma_1+\phi_0/2)), -2L\cos\alpha_2\sin(\pi/2-\gamma_1+\phi_0/2))\right)^T,\\
&\mathbf{p}_{V_3} = \mathbf{p}_{V_2} + \left(2L\cos\alpha_2\cos(\pi/2-\gamma_1+\phi_0/2)), -2L\cos\alpha_2\sin(\pi/2-\gamma_1+\phi_0/2))\right)^T,\\
&\mathbf{p}_{V_4} = \mathbf{p}_{V_3} + \begin{pmatrix} 2L\cos\alpha_2\cos(\pi/2-\gamma_3+\gamma_2-\gamma_1+\phi_0/2), \\ -2L\cos\alpha_2\sin(\pi/2-\gamma_3+\gamma_2-\gamma_1+\phi_0/2) \end{pmatrix},
\end{aligned}
\tag{3-15d}
$$

where $\mathbf{p}$ represents the coordinate and its subscript represents the vertex.

Since the coordinates of all the vertexes in the shape-lines have been defined, we can match the shape of the morphing surface to the target surface by selecting proper design parameters. This process is described using an example in which a parabolic cylinder is transformed to a paraboloid.

One of our target surfaces is a paraboloid, which can be obtained from the rotation around the y-axis of a parabola, as shown in Fig. 3-8(a) in which the parabola is indicated in red. The function of this parabola is assumed to be $y = m_1 x^2$, and for a morphing surface, if the coordinates of vertexes O, V_2, V_4, H_2 and H_4 match the function of this parabola, the morphing surface matches the paraboloid.

The other target surface is a parabolic cylinder, which can be constructed by the translation along the *z*-axis of a parabola, as illustrated in Fig. 3-8(b) in which the parabola is represented in blue. Assuming that the function of this parabola is $y = m_2 x^2$, in a morphing surface, if the coordinates of vertexes O, V_2, and V_4 match the function of this parabola, and the coordinates of vertexes O, H_2 and H_4 match the straight line $y = 0$, the morphing surface matches the parabolic cylinder. If the morphing surface and target surface are matched, the following equation should be satisfied:

$$\left\|\mathbf{p}_{\mathrm{H}_2}-\mathbf{P}_{\mathrm{H}_2}\right\|<\varepsilon,$$
$$\left\|\mathbf{p}_{\mathrm{H}_4}-\mathbf{P}_{\mathrm{H}_4}\right\|<\varepsilon; \tag{3-16a}$$

$$\left\|\mathbf{p}_{\mathrm{V}_2}-\mathbf{P}_{\mathrm{V}_2}\right\|<\varepsilon,$$
$$\left\|\mathbf{p}_{\mathrm{V}_4}-\mathbf{P}_{\mathrm{V}_4}\right\|<\varepsilon; \tag{3-16b}$$

where ε is the accuracy error, and

$$\mathbf{P}_{\mathrm{H}_i}=\left(\mathbf{p}_{\mathrm{H}_i}(1,1),\ m_1(\mathbf{p}_{\mathrm{H}_i}(1,1))^2\right)^{\mathrm{T}},$$
$$\mathbf{P}_{\mathrm{V}_i}=\left(\mathbf{p}_{\mathrm{V}_i}(1,1),\ m_2(\mathbf{p}_{\mathrm{V}_i}(1,1))^2\right)^{\mathrm{T}}, \tag{3-17}$$

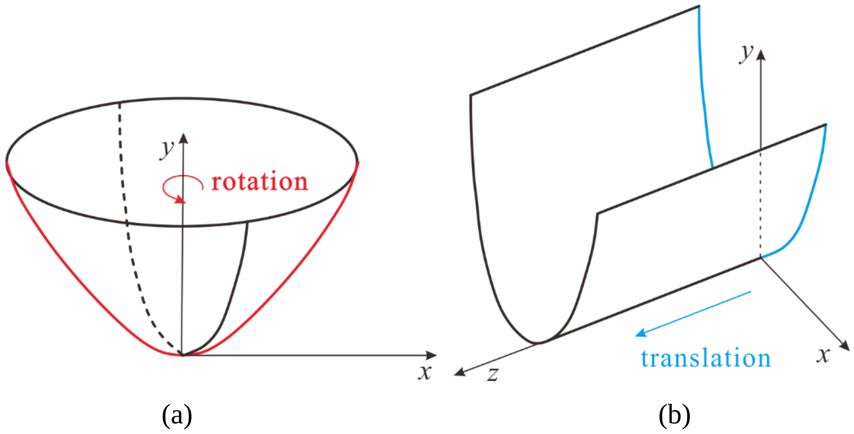

Fig. 3-8 Construction of (a) a paraboloid and (b) a parabolic cylinder.

Next, the conditions under which a morphing surface can transform between the two target surfaces are discussed. The process can be described as follows:

(1) Step 1: the two target surfaces are defined, with m_1 less than m_2. I assume that the length L=0.5.

(2) Step 2: different values are assigned to $\alpha_1-\alpha_6$ and γ_0.

(3) Step 3: $\alpha_1-\alpha_6$ are substitute with different γ_0 values in Eqns. (3-14) and (3-15) and obtain the coordinates of the vertexes in the shape-lines of the morphing surface to the function of the parabola in the paraboloid and parabolic cylinder.

(4) Step 4: check whether these coordinates satisfy the function of the parabola in the paraboloid and parabolic cylinder. If no matching occurs, return to Step 2 or proceed to Step 5.

(5) Step 5: the proper design parameters that allow the morphing surface to transform between the two target surfaces are identified, and the process is terminated.

This process is illustrated in Fig. 3-9 and implemented in MATLAB.

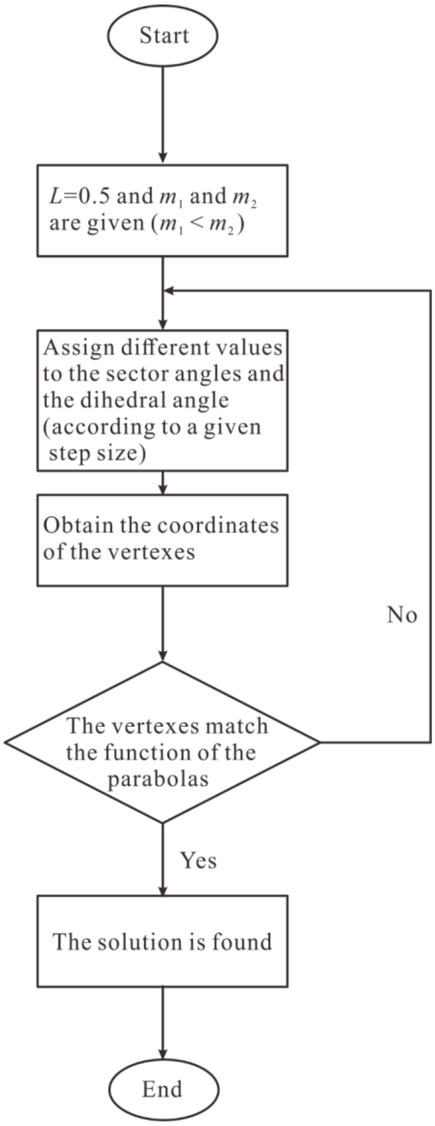

Fig. 3-9 Process of identifying a morphing surface that can transform between two target surfaces.

An example is shown in Fig. 3-10 with

$$\alpha_1 = 60^{\circ}, \alpha_2 = 56.5^{\circ}, \alpha_3 = 58.5^{\circ}, \alpha_4 = 58^{\circ}, \ \alpha_5 = 56^{\circ}, \ \alpha_6 = 56^{\circ},$$

and the surface can transform from a paraboloid ($m_1 = 0.13$ and $\gamma_0 = 92.5^{\circ}$) to a parabolic cylinder ($m_2 = 0.25$ and $\gamma_0 = 88.5^{\circ}$). The two surfaces are shown in Figs. 3-10(a) and (b), respectively, and the morphing process is illustrated in Fig. 3-10(c).

3.4 Conclusions

This chapter describes a one-DOF mobile assembly of spherical 4*R* linkages inspired by origami, which is extended to a morphing surface that is one-DOF by adding spherical 6*R* and 8*R* linkages. The above-mentioned morphing surface is transformed

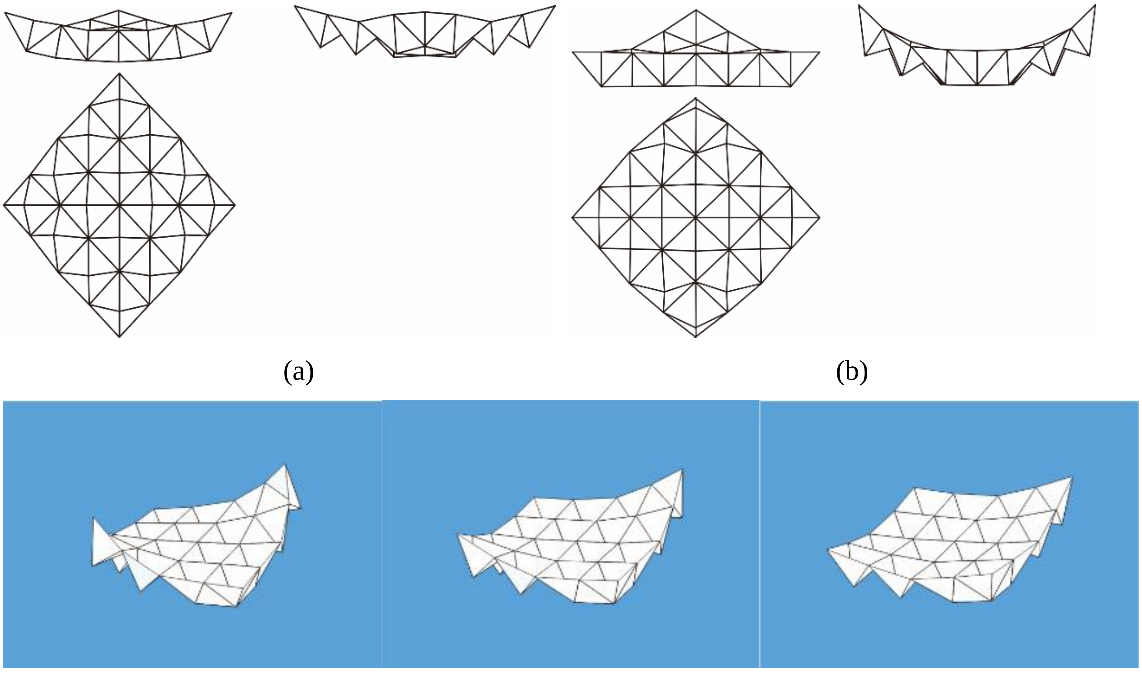

(c)

Fig. 3-10 Morphing surface: (a) front view (top left), left view (top right) and top view (bottom) of the paraboloid; (b) front view (top left), left view (top right) and top view (bottom) of the parabolic cylinder; (c) process of transformation from a parabolic cylinder to a paraboloid.

through the motion of the spherical linkages. The surface has two shape-lines that determine the shape of the surface, and the surfaces can be designed by tuning the two shape-lines. An example of the morphing surface that can transform from a parabolic cylinder to a paraboloid is provided, which may provide a reference to design flexible antennas in aerospace applicatio

Chapter 4 3D mobile networks of spherical linkages: rigid origami tubes

4.1 Introduction

Rigidly foldable origami tubes with open ends have been reported in the past. Kinematically, these tubes are assemblies of spherical linkages in which the rigid links are connected by revolute joints. In this chapter, new methods to obtain origami tubes that are rigidly foldable with a single degree-of-freedom are described.

The layout of this chapter is as follows. First, as described in Chapter 4.2, several existing tubes are conjoined by merging common sides or corners, resulting in a family of tubes with asymmetric polygonal cross-sections. Next, Chapter 4.3 introduces transition parts in an existing tube, thereby developing the second set of origami tubes in which the crease lines between neighbouring layers form nonplanar polygons. The formation of multi-layered and curved tubes based on the above-mentioned tubes is discussed in Chapter 4.4. Finally, the concluding remarks are presented in Chapter 4.5.

4.2 Two tubes formed by combination

Goldberg 5*R* and 6*R* linkages are obtained by merging two or more Bennett linkages through a summation or subtraction process depending on the relative positions of the adjoined Bennett linkages. New tubes known as *combined tubes* are generated by adopting a similar approach for the sections of the tubes.

4.2.1 Summation of two tubes

Figures 4-1(a) and 4-1(b) show two one-DOF rigidly foldable tubes, Tubes 1 and 2. The facets of both the tubes are parallelograms. Tube 1 with a kite cross-section, as shown in Fig. 4-1(a), is formed using two pieces with facets having different lengths. Both the top and bottom pieces are flat developable with $\alpha^{\mathrm{T1}}+\gamma^{\mathrm{T1}}=\pi$, $\beta^{\mathrm{T1}}+\delta^{\mathrm{T1}}=\pi$, and $\alpha_1^{\mathrm{T1}}+\gamma_1^{\mathrm{T1}}=\pi$, $\beta_1^{\mathrm{T1}}+\delta_1^{\mathrm{T1}}=\pi$. To realize flat foldability, $\alpha^{\mathrm{T1}}=\beta^{\mathrm{T1}}$ and $\alpha_1^{\mathrm{T1}}=\beta_1^{\mathrm{T1}}$. To connect the pieces to form a one-DOF tube, $a\cos\alpha_1^{\mathrm{T1}}=b\cos\alpha^{\mathrm{T1}}$. In the case of Tube 2 with a parallelogram cross-section, as shown in Fig. 4-1(b), the left and right pieces are flat developable and have an identical geometry in which $\alpha^{\mathrm{T2}}=\beta^{\mathrm{T2}}$ and $\gamma^{\mathrm{T2}}=\delta^{\mathrm{T2}}$. The cross-sections of Tubes 1 and 2, ABCD, are plane-symmetric and line-symmetric, respectively. The tubes with the parallelogram and kite cross-sections have one and two flat folding states, respectively. If the two tubes are placed side by side such that they share a common side, the tubes can be joined via the common side, forming the compound tube shown in Fig. 4-1(c), with

$$\alpha^{\mathrm{T1}}=\alpha^{\mathrm{T2}}=\beta^{\mathrm{T1}}=\beta^{\mathrm{T2}}=\alpha; \tag{4-1}$$

where superscripts T1 and T2 represent Tubes 1 and 2, respectively. In addition, the widths of the facets of two tubes should match. If these conditions are satisfied, the combination does not alter the motion of each tube, and the combined tube has only one-DOF, i.e., the compound tube is also rigidly foldable. In this case, the common side of the two tubes can be removed, resulting in a new origami tube that is rigidly foldable, as shown in Fig. 4-1(d).

According to Chapter 1.2.3.1, Tubes 1 and 2 can be considered as the assembly of spherical 4R linkages at each vertex. In the case of Tube 1, at vertex A, the four twist angles are $\alpha_{12}=\alpha^{\mathrm{T1}}$, $\alpha_{23}=\gamma^{\mathrm{T1}}$, $\alpha_{34}=\delta^{\mathrm{T1}}$, and $\alpha_{41}=\beta^{\mathrm{T1}}$, and they can be substituted in Eqn. (1-7) to yield

$$\cos^2\alpha^{\mathrm{T1}}-\sin^2\alpha^{\mathrm{T1}}\cos\theta_1^{\mathrm{T1}}=\cos^2\gamma^{\mathrm{T1}}-\sin^2\gamma^{\mathrm{T1}}\cos\theta_3^{\mathrm{T1}}. \tag{4-2a}$$

Similarly, in the case of Tube 2, $\alpha_{12}=\alpha^{\mathrm{T2}}$, $\alpha_{23}=\gamma^{\mathrm{T2}}$, $\alpha_{34}=\delta^{\mathrm{T2}}$, and $\alpha_{41}=\beta^{\mathrm{T2}}$, and

$$\cos^2\alpha^{\mathrm{T2}}-\sin^2\alpha^{\mathrm{T2}}\cos\theta_1^{\mathrm{T2}}=\cos^2\gamma^{\mathrm{T2}}-\sin^2\gamma^{\mathrm{T2}}\cos\theta_3^{\mathrm{T2}}. \tag{4-2b}$$

Substituting Eqn. (4-1) in Eqn. (4-2) yields

$$\cos^2\alpha-\sin^2\alpha\cos\theta_1^{\mathrm{T1}}=\cos^2\gamma^{\mathrm{T1}}-\sin^2\gamma^{\mathrm{T1}}\cos\theta_3^{\mathrm{T1}}, \tag{4-3a}$$

$$\cos^2\alpha-\sin^2\alpha\cos\theta_1^{\mathrm{T2}}=\cos^2\gamma^{\mathrm{T2}}-\sin^2\gamma^{\mathrm{T2}}\cos\theta_3^{\mathrm{T2}}. \tag{4-3b}$$

After the tubes are attached, the obtained combination is one-DOF, and because of the assignment of the sector angles and mountain-valley crease lines,

$$\theta_1^{\mathrm{T1}}=\theta_1^{\mathrm{T2}}. \tag{4-4}$$

By merging Eqns. (4-3) and (4-4), Eqn. (4-3b) can be rewritten as

$$\cos^2\alpha-\sin^2\alpha\cos\theta_1^{\mathrm{T1}}=\cos^2\gamma^{\mathrm{T2}}-\sin^2\gamma^{\mathrm{T2}}\cos\theta_3^{\mathrm{T2}}. \tag{4-5}$$

Moreover, Eqn. (4-3a) is satisfied. In the new tube, after removing the common parts, vertex A in Tubes 1 and 2 becomes vertex A^{T1} and A^{T2}, respectively, as illustrated in Fig. 4-1(e). At vertex A^{T1},

$$\cos^2\alpha-\sin^2\alpha\cos\theta=\cos^2\gamma^{T1}-\sin^2\gamma^{T1}\cos\theta_3^{T1}. \tag{4-6a}$$

At vertex A^{T2},

$$\cos^2\alpha-\sin^2\alpha\cos(-\theta)=\cos^2\gamma^{\mathrm{T2}}-\sin^2\gamma^{\mathrm{T2}}\cos\theta_3^{\mathrm{T2}}. \tag{4-6b}$$

Moreover

$$\theta=-\theta_1^{\mathrm{T1}}. \tag{4-6c}$$

Merging Eqns. (4-6a) and (4-6c) yields Eqn. (4-2b), and merging Eqns. (4-6b) and (4-6c) yields Eqn. (4-5). The same relations can be achieved at vertex D^{T1} Hence, removing the common part of the two combined tubes does not change the relationships among their angles, and the new combined tube is also one-DOF.

The cross-section of the resultant tube is neither in line nor plane-symmetric. In fact, the cross-section is an arbitrary polygon. When vertex A of Tubes 1 and 2 is positioned at the same point,

$$\gamma^{\mathrm{T1}} + \gamma^{\mathrm{T2}} = \pi. \tag{4-7}$$

In this case, the two adjacent facets from each tube can be welded into one piece to form a new tube with a cross-section consisting of an odd number of sides.

The schematics in Figs. 4-2(a) and 4-2(b) illustrate the summation approach in which a kite tube and parallelogram tube are combined, as well as the physical models demonstrating the folding of the resultant tubes. It should be noted that when the two tubes are joined through one of their longer sides, the folding on the short side of the kite tube is not disturbed, and the combined tube still has two folding states, as shown in Fig. 4-2(b).

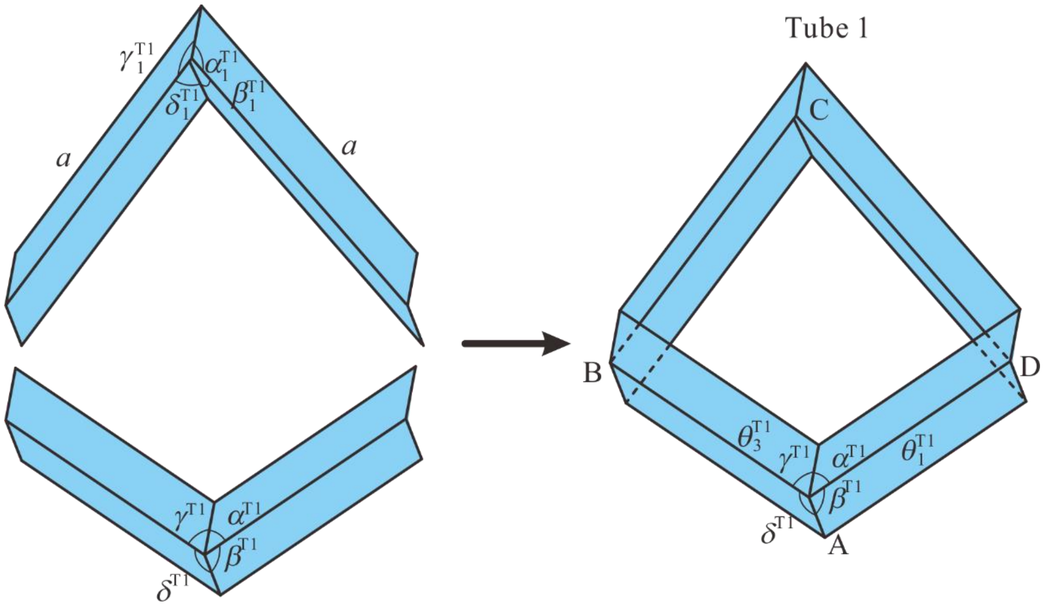

(a)

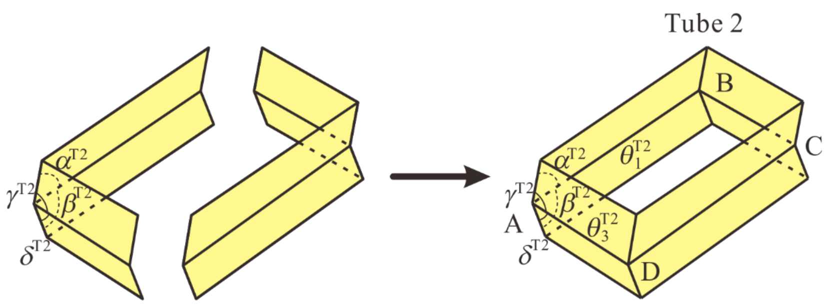

(b)

Fig. 4-1 Construction of a tube by summation: (a) Tube 1, (b) Tube 2, (c) Tube 2 is attached to Tube 1, and (d) the common portion of the joined tube is removed to form a new rigidly foldable tube; (e) sector angles in the new foldable tube.

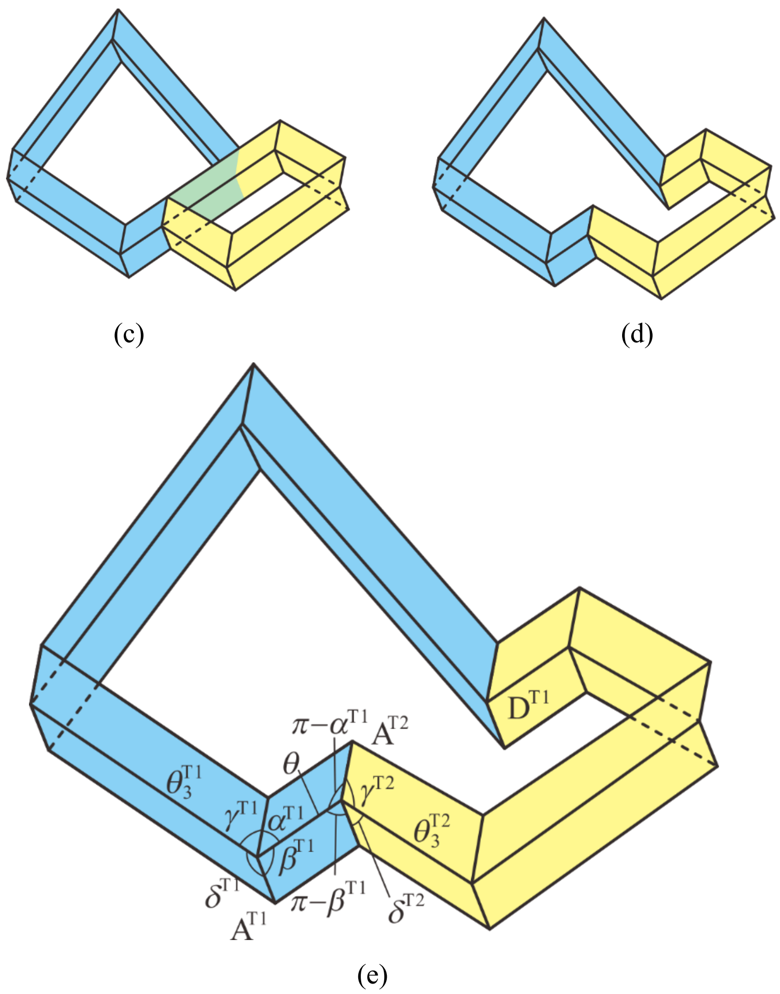

Fig. 4-1 Construction of a tube by summation: (a) Tube 1, (b) Tube 2, (c) Tube 2 is attached to Tube 1, and (d) the common portion of the joined tube is removed to form a new rigidly foldable tube; (e) sector angles in the new foldable tube. (continued)

4.2.2 Subtraction of two tubes

Figure 4-3 illustrates the subtraction process in which the tube with the smaller cross-section, Tube 2, is nested inside the larger Tube 1. When the geometric conditions

$$\gamma^{T1} = \gamma^{T2} = \delta^{T1} = \delta^{T2} = \gamma \tag{4-8}$$

are satisfied, and the widths of the facets of the two tubes match each other, the subtraction can be performed along one common side, as shown in Fig. 4-3(c). Alternatively, if the geometric conditions

$$\alpha^{T1} = \alpha^{T2} = \beta^{T1} = \beta^{T2} = \alpha, \tag{4-9a}$$

$$\gamma^{T1} = \gamma^{T2} = \delta^{T1} = \delta^{T2} = \gamma, \tag{4-9b}$$

are met, and the widths of the facets of the two tubes match each other, the subtraction can be performed at the common corner of the two tubes, Fig. 4-3(e), leading to two common sides. After removing the common parts, new tubes with combined and nonsymmetric cross-sections can be obtained, as shown in Figs. 4-3(d) and 4-3(f), respectively.

Consider the process shown in Figs. 4-3(e) and (f) as an example. At vertex B in Tube 2,

$$\cos^2\alpha-\sin^2\alpha\cos\theta_1^{\mathrm{T2}}=\cos^2(\pi-\gamma)-\sin^2(\pi-\gamma)\cos\theta_3^{\mathrm{T2}}, \tag{4-10a}$$

which can be simplified as

$$\cos^2\alpha-\sin^2\alpha\cos\theta_1^{\mathrm{T2}}=\cos\gamma-\sin^2\gamma\cos\theta_3^{\mathrm{T2}}. \tag{4-10b}$$

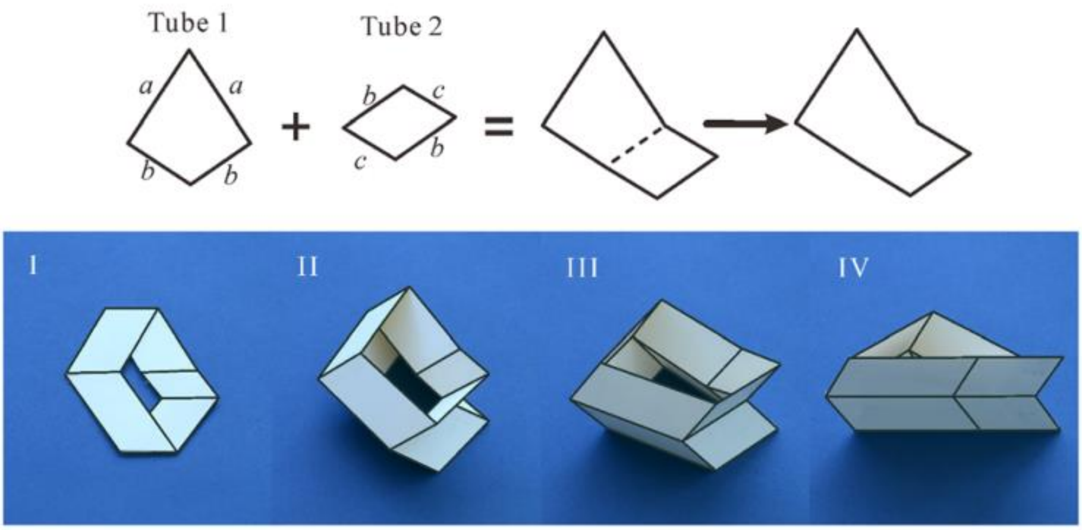

(a)

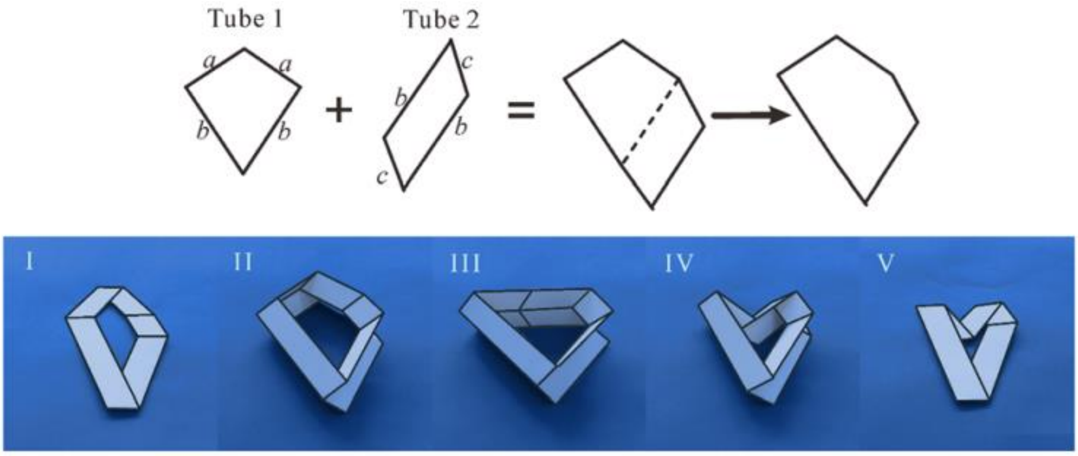

(b)

Fig. 4-2 Summation of two tubes: (a) schematic of the summation method with the shorter sides joined together, and the expansion sequence of a tube model from its flat folding state I; (b) schematic of the summation method with longer sides joined together, and the expansion sequence of a tube model from its flat folding state I to its second flat folding state V.

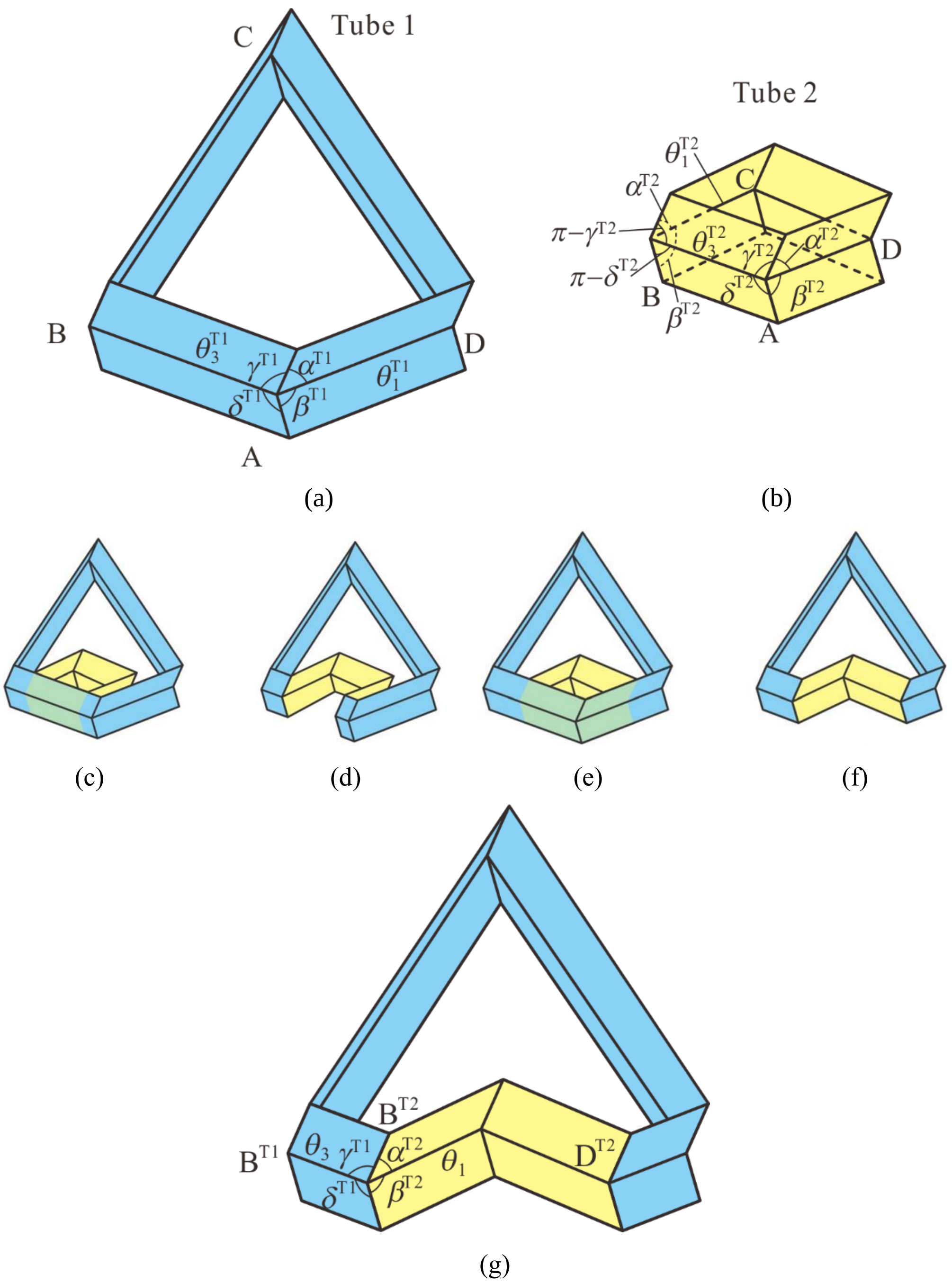

Fig. 4-3 Construction of a tube by subtraction: (a) Tube 1; (b) Tube 2; (c) Tube 2 is nested inside Tube 1; (d) the common portion of the joined tube is removed, thereby forming a new rigidly foldable tube; (e) Tube 2 is nested inside a corner of Tube 1; (f) the common portion of the joined tube is removed, thereby forming a new rigidly foldable tube and (g) sector angles in the new tube.

After the combination, vertex B in Tube 2 becomes vertex B^{T2}, and Eqn. (4-10b) is satisfied. Removing the common parts (see Fig. 4-3(g)) leads to

$$\cos^2\alpha - \sin^2\alpha\cos\theta_1 = \cos\gamma - \sin^2\gamma\cos\theta_3, \tag{4-11a}$$

$$\theta_1 = \theta_1^{\mathrm{T2}},\quad \theta_3 = -\theta_3^{\mathrm{T2}}. \tag{4-11b}$$

Merging Eqns. (4-11a) and (4-11b) leads to Eqn. (4-10b). The same conclusion can be achieved at vertex D^{T2}. Hence, the resultant tube exhibits rigid foldability with one-DOF. Similarly, the tube obtained from the process shown in Figs. 4-3(c) and 4-3(d) is also one-DOF. Figures 4-4 and 4-5 schematically illustrate the subtraction process involving a common side and common corner, respectively, accompanied by the folding sequences of the physical models obtained through this process.

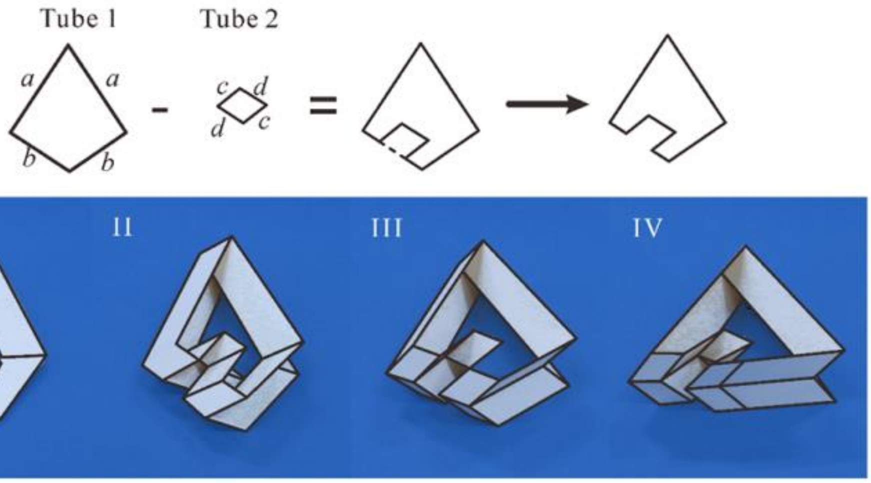

(a)

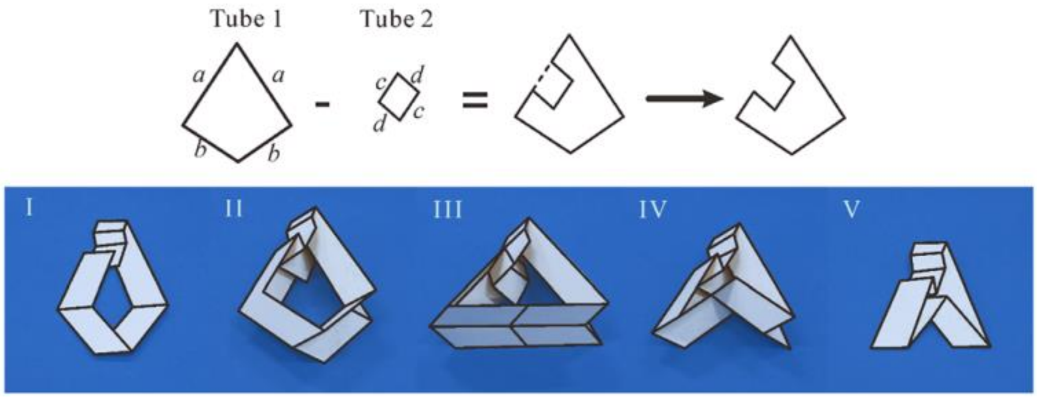

(b)

Fig. 4-4 Subtraction of two tubes: (a) schematic of the subtraction method with Tube 2 nested inside the shorter side of Tube 1, and the expansion sequence of a tube model from its flat folding state I and (b) schematic of the subtraction method with Tube 2 nested inside the longer side of Tube 1, and the expansion sequence of a tube model from its flat folding state I to its second flat folding state V.

4.2.3 Combination of more tubes

Not only can a pair of rigidly foldable tubes be combined to create new rigidly foldable tubes, but also more tubes can be united using both the summation and subtraction approaches. An example is shown in Fig. 4-6, which involves three tubes.

First, Tubes 1 and 2 are summed, and Tube 3 is subtracted from the combined tube, which results in a new tube with a seven-side polygonal cross-section (see Fig. 4-6(a)). Similar to Goldberg's method, we can subtract the summation of Tubes 1 and 2 from Tube 3 to produce a clipped tube. The process is shown in Fig. 4-6(b). All the new tubes exhibit rigid foldability, as demonstrated by the physical models.

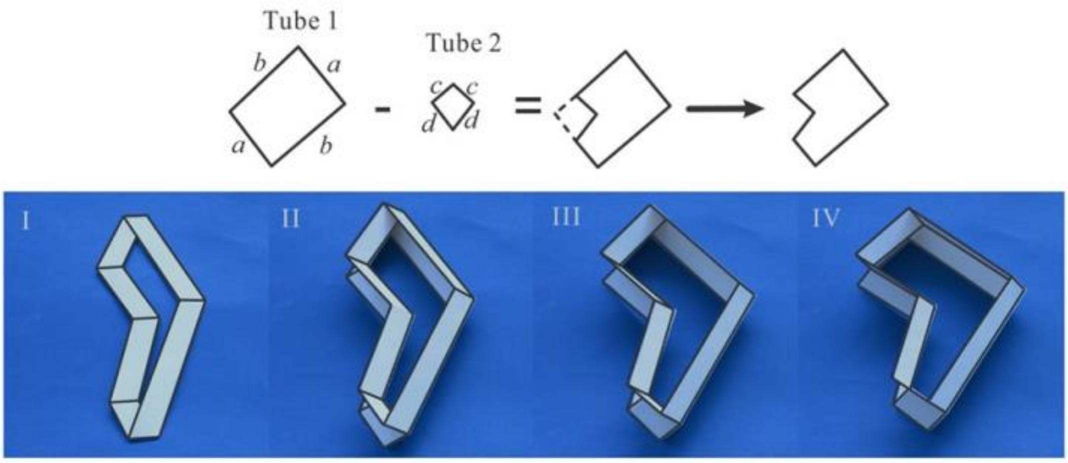

(a)

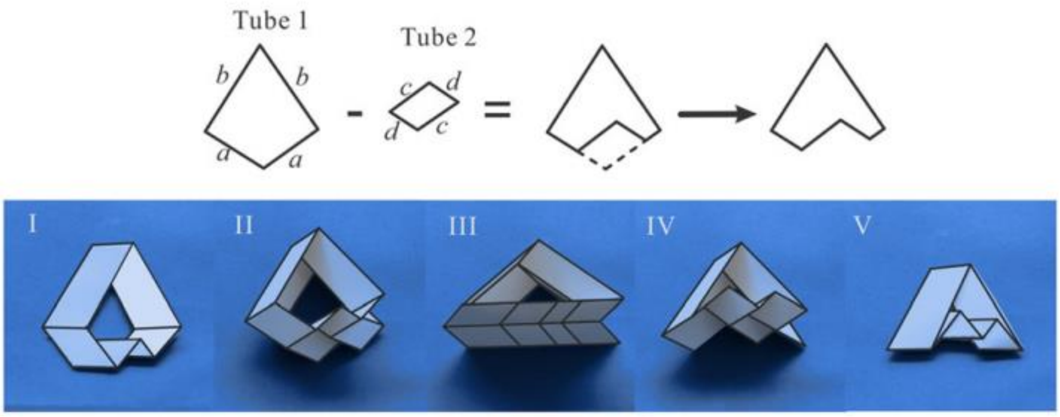

(b)

Fig. 4-5 Subtraction of two tubes: (a) schematic of the subtraction method in which Tube 2 with a kite cross-section is nested inside a corner of Tube 1 with a parallelogram cross-section, and the expansion sequence of a tube model from its flat folding state I and (b) schematic of the subtraction method in which Tube 2 with a parallelogram cross-section is nested inside Tube 1 with a kite cross-section, and the expansion sequence of a tube model from its flat folding state I to its second flat folding state V.

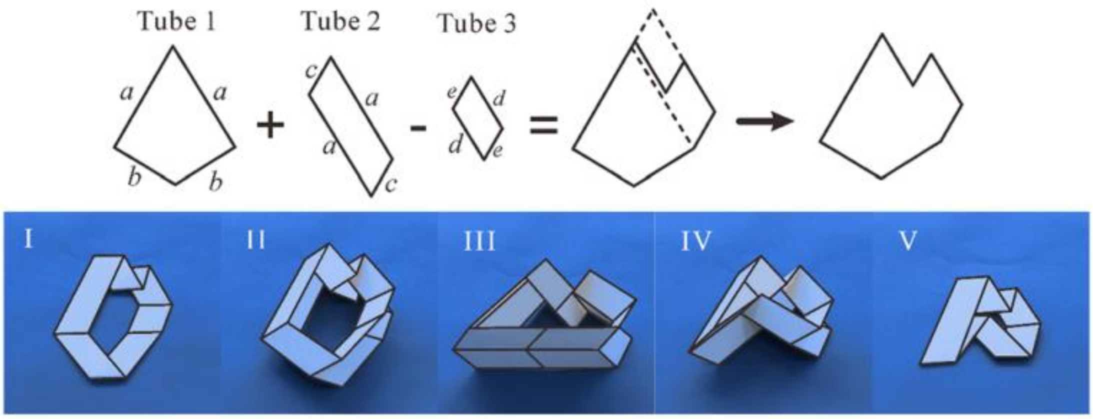

(a)

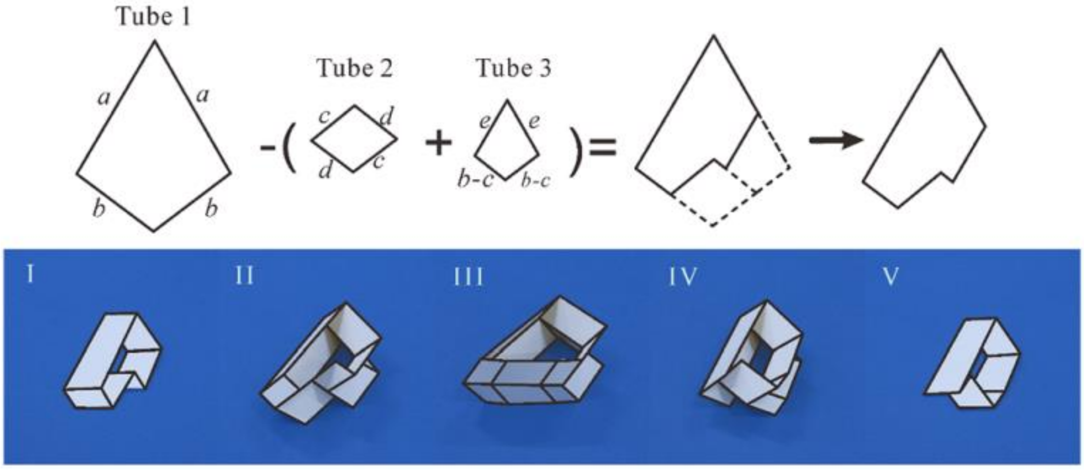

(b)

Fig. 4-6 Combination of three tubes: (a) schematic showing the combination of three tubes, and the folding sequence of a model tube and (b) schematic showing a different way of combining three tubes, and the folding sequence of a model tube.

4.3 Tubes formed by adding transition parts

Transition parts can be added to a rigidly foldable origami tube to produce a new rigidly foldable tube known as a *shifted tube*.

In this section, how a pair of transition parts can be added to a rigidly foldable tube to produce a new tube termed as a shifted tube is demonstrated. Figure 4-7(a) shows a rigidly foldable origami tube with a kite cross-section. This tube is subsequently separated into two parts: blue P1 and yellow P2. A pair of identical transition parts shown in Fig. 4-7(b), T1, is to be added between these parts. All the facets in T1 have a parallelogram shape. The new tube with the added transition parts is illustrated in Fig. 4-7(c). Next, the conditions under which the rigid foldability of the resultant tube can be achieved is identified. Since a tube can be considered as an assembly of spherical 4*R* linkages at each vertex, prior to adding the transition parts, at the vertex A surrounded by twist angles α_{12}, α_{23}, α_{34} and α_{41},

$$\boldsymbol{Q}_{21}\boldsymbol{Q}_{32}\boldsymbol{Q}_{43}\boldsymbol{Q}_{14} = \boldsymbol{I}_3, \tag{4-12}$$

where

$$\boldsymbol{Q}_{(i+1)i} = \begin{bmatrix} \cos\theta_i & -\sin\theta_i\cos\alpha_{i(i+1)} & \sin\theta_i\sin\alpha_{i(i+1)} \\ \sin\theta_i & \cos\theta_i\cos\alpha_{i(i+1)} & -\cos\theta_i\sin\alpha_{i(i+1)} \\ 0 & \sin\alpha_{i(i+1)} & \cos\alpha_{i(i+1)} \end{bmatrix}. \tag{4-13}$$

Merging Eqns. (4-12) and (4-13) yields

$$\cos\alpha_{12}\cos\alpha_{41} - \sin\alpha_{12}\sin\alpha_{41}\cos\theta_1 = \cos\alpha_{23}\cos\alpha_{34} - \sin\alpha_{23}\sin\alpha_{34}\cos\theta_3. \tag{4-14}$$

Once a pair of transition parts T1 has been added, vertex A has two parts: A' with twist angles α_{12}, γ_1, γ_2 and α_{41}, and A" with twist angles $\pi-\gamma_1$, α_{23}, α_{34}, $\pi-\gamma_2$. According to Eqns. (4-12) and (4-13),

$$\cos\alpha_{12}\cos\alpha_{41} - \sin\alpha_{12}\sin\alpha_{41}\cos\theta_1 = \cos\gamma_1\cos\gamma_2 - \sin\gamma_1\sin\gamma_2\cos\theta_\gamma \tag{4-15a}$$

and

$$\begin{aligned} &\cos(\pi-\gamma_1)\cos(\pi-\gamma_2) - \sin(\pi-\gamma_1)\sin(\pi-\gamma_2)\cos\theta_\gamma = \\ &\cos\alpha_{23}\cos\alpha_{34} - \sin\alpha_{23}\sin\alpha_{34}\cos\theta_3 \end{aligned} \tag{4-15b}$$

Merging Eqns. (4-15a) and (4-15b) yields Eqn. (4-14). The same conclusion can be drawn for the two vertices on the back of Fig. 4-7(b) where the other T1 is added. This finding demonstrates that adding a pair of identical transition parts formed by parallelogram facets to an existing tube does not change the relationship among the angles of the original tube. Hence, it can be concluded that the new shifted tube is still rigidly foldable with one-DOF.

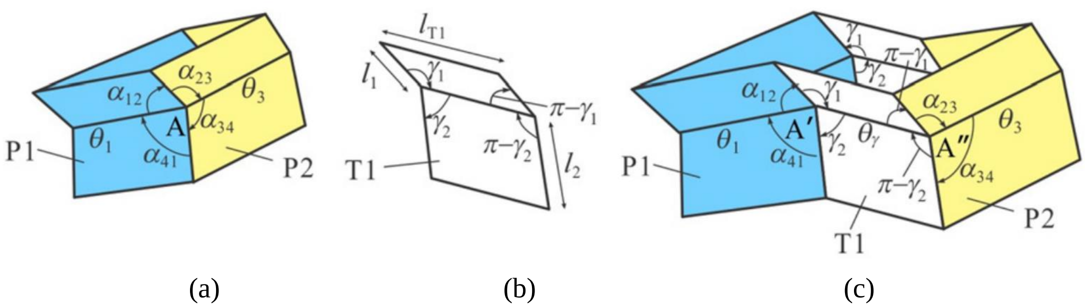

Fig. 4-7 Formation of a shifted tube: (a) original tube, (b) transition part, and (c) shifted tube after insertion of the transition pair.

The addition of a transition pair may alter the foldability of the tube. In general, if

$\gamma_1 \neq \gamma_2$, the resultant cross-sections of the shifted tube are no longer planer, and thus, the shifted tube is not flat-foldable even when the original tube is flat-foldable. Figure 4-8(a) shows an example of this case. However, if the original tube is flat-foldable, and for the added parts $\gamma_1 = \gamma_2$, the shifted tube remains flat-foldable with a planar cross-section. An example of this case is shown in Fig. 4-8(b).

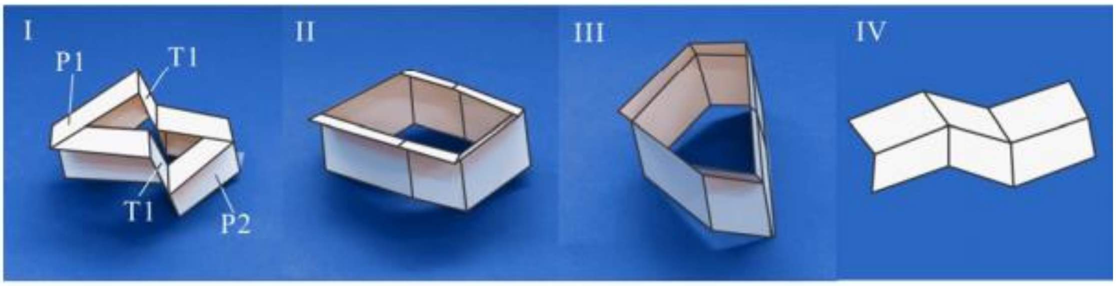

(a)

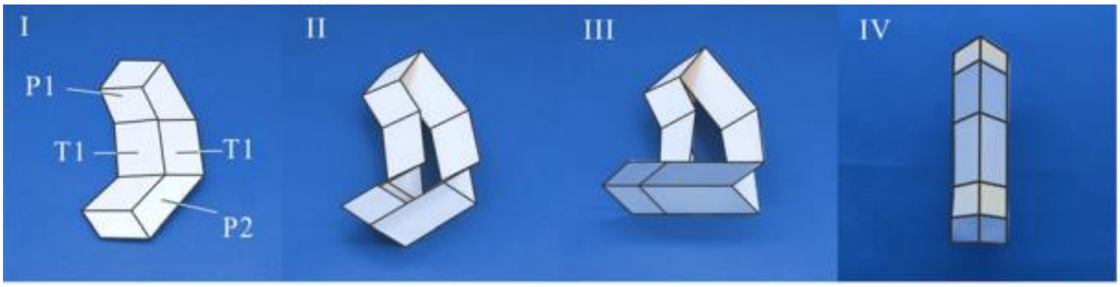

(b)

Fig. 4-8 Two shifted tubes: (a) Folding sequence of a shifted tube, with IV showing the side view of the tube in configuration II, demonstrating a nonplanar cross-section and (b) folding sequence of another shifted tube. The tube is flat-foldable and has a planar cross-section, as demonstrated by IV: side view of the tube in configuration II.

Using this method, more than a pair of transition parts can be added to the original tube without changing its DOF. Each pair must contain two identical parts with parallelogram facets. Figure 4-9 shows the rigid folding sequence of a physical model in which two transition pairs, labelled T1 and T2, are added to a kite tube. Moreover, a pair of transition parts can be added to different locations of the same original tube. Two physical models shown in Figs. 4-10(a) and (b) are used to illustrate this aspect. In the case shown in Fig. 4-10(a), the original tube with a six-sided polygonal cross-section is divided into a four-sided left part and two-sided right part before inserting a pair of transition parts, T1, to form a shifted tube. In the case shown in Fig. 4-10(b), the same six-sided polygonal cross-section of the original tube is partitioned into a three-sided left part and three-sided right part instead, and the transition pair T1 is added. The resultant tubes in Figs. 4-10(a) and 4-10(b) are considerably different but rigidly foldable.

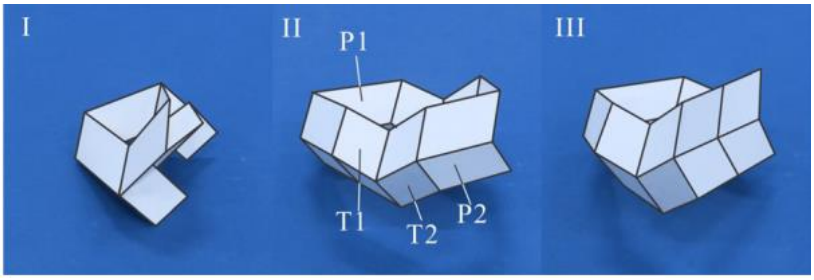

Fig. 4-9 Folding sequence of a shifted tube with two transition pairs T1 and T2 added

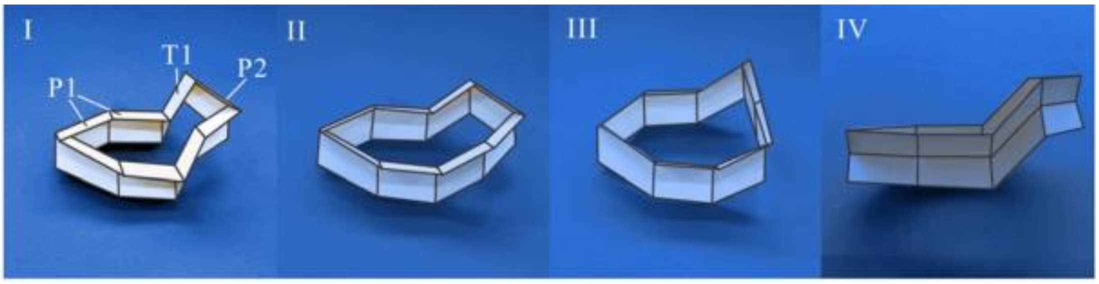

(a)

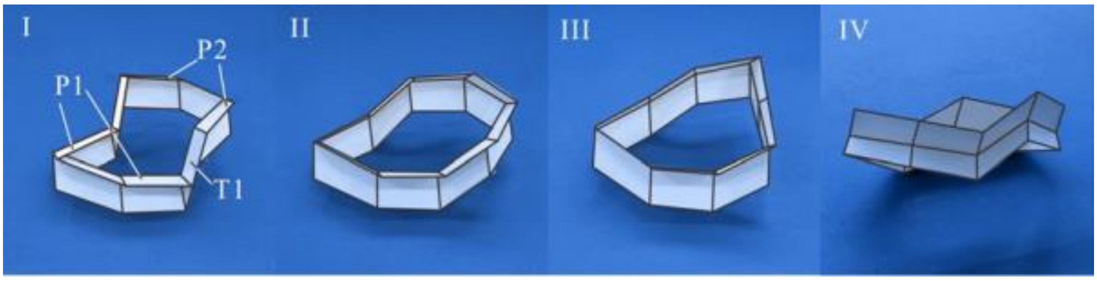

(b)

Fig. 4-10 Two shifted tubes: (a) Folding sequence of a shifted tube with transition pair T1 added. IV shows the side view of configuration II and (b) folding sequence of the other shifted tube with transition pair T1 added at a location different from that in (a). IV shows the side view of configuration II.

4.4 Multi-layered straight and curved tubes

Multi-layered tubes can be obtained by stacking a single-layered tube, as discussed in Chapters 4.2 and 4.3, with parallel or nonparallel cross-sections to form a straight tube or curved tube, respectively. In the latter case, certain parallelogram facets are altered to trapezoid facets.

4.4.1 Multi-layered tubes

Stacking the same single-layered tubes outlined in Chapter 4.3 yields a long multi-layered tube, which has a straight profile, in general. Several examples of such tubes are shown in Fig. 4-11. The single-layered tubes can be combined or shifted tubes.

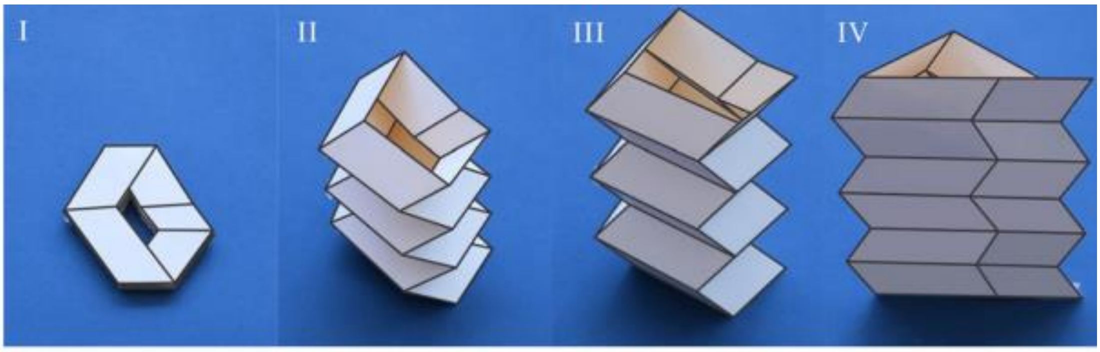

(a)

(b)

Fig. 4-11 Folding sequences of multi-layered straight tubes formed by (a) combination and (b) shifting.

4.4.2 Curved tubes with combined cross-sections

A straight tube with a planar cross-section can be transformed to a curved one by plane slicing a portion of the tube. Figure 4-12 shows two single-layered curved tubes created using this method. In the case of the first tube, shown on the left in Fig 4-12(a), the top and bottom slicing planes have an inclination angle $\varepsilon^{\mathrm{T1}}$ and ν^{T1}, respectively. Consequently, the front and back parallelogram facets become trapezoid facets. If the same approach is applied to the second tube, Tube 2, with slicing plane angles $\varepsilon^{\mathrm{T2}}$ and ν^{T2}, the two tubes can be combined in the same way as those considered in Chapter 4.2. However, certain additional conditions must be satisfied:

$$\alpha^{\mathrm{T1}}=\alpha^{\mathrm{T2}},\beta^{\mathrm{T1}}=\beta^{\mathrm{T2}}, \tag{4-16a}$$

$$\varepsilon^{\mathrm{T1}}=\varepsilon^{\mathrm{T2}},\nu^{\mathrm{T1}}=\nu^{\mathrm{T2}}, \tag{4-16b}$$

and the side lengths of the facets on the commonly shared side must match. After removing the shared facets, a combined curved tube with six sides can be obtained (see the left side of Fig. 4-12(b)). Moreover, if

$$\gamma^{\mathrm{T1}}+\gamma^{\mathrm{T2}}=\pi \text{ and } \delta^{\mathrm{T1}}+\delta^{\mathrm{T2}}=\pi, \tag{4-17}$$

the common creases of the combined tube can be removed, and the two facets on either side can be bonded to a single facet. The resulting tube has five sides (see the right side of Fig. 4-12(b)).

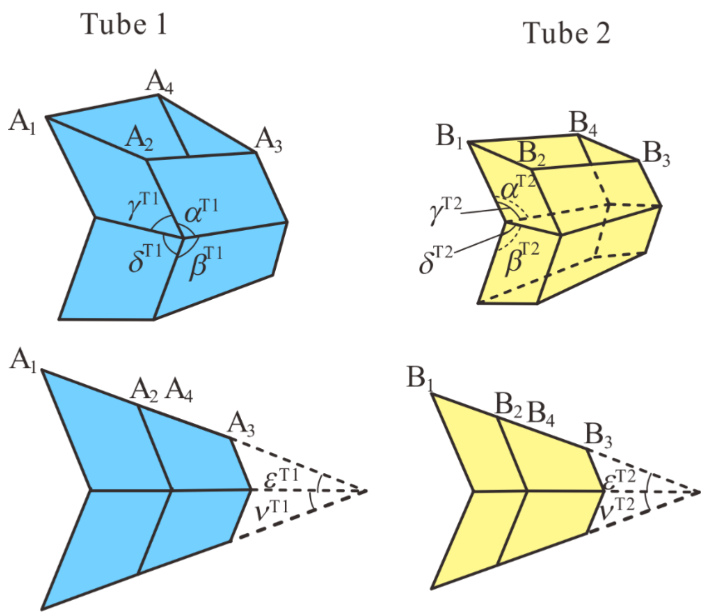

(a)

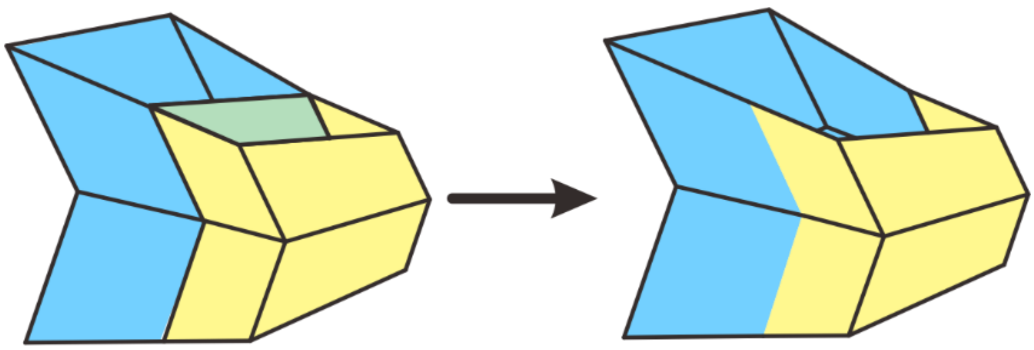

(b)

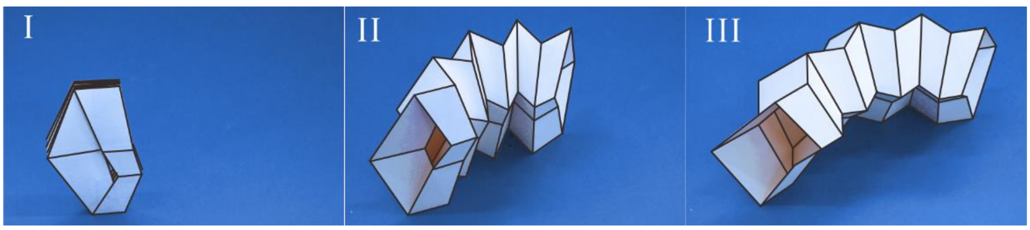

(c)

Fig. 4-12 Curved tube constructed by summation. (a) Two tubes (top) and their side view (bottom), (b) combination of the tubes before and after the removal of the common side, and (c) a multi-layered curved tube that deploys from the flat folding state I.

By stacking multiple such curved tubes, a multi-layered curved tube can be obtained. Figure 4-12(c) shows the folding sequence of a curved combined tube.

4.4.3 Curved shifted tubes

Transition parts can be added to a curved tube while retaining its rigid foldability. Figure 4-13(a) shows a portion of a rigidly foldable curved tube prior to the addition of any transition part. The dihedral angles of the adjacent facets between two neighbouring layers are denoted as η_{L} and η_{R}; according to the spherical cosine formula,

$$\begin{aligned}&\cos\alpha_{12}\cos\alpha_{41}+\sin\alpha_{12}\sin\alpha_{41}\cos\eta_{\mathrm{L}}=\cos\delta_{\mathrm{L}}=\\&\cos\alpha_{23}\cos\alpha_{34}+\sin\alpha_{23}\sin\alpha_{34}\cos\eta_{\mathrm{R}},\end{aligned}\tag{4-18}$$

where δ is the angle between the ridgelines on the left side of the tube. Next, a pair of transition parts made using rectangular facets are added to the tube. Only the front part of the transition pair is shown in Fig. 4-13(b), and $\gamma_1=\gamma_2=(\pi/2)$. Geometrically, for the left side of the transition part,

$$\begin{aligned}&\cos\alpha_{12}\cos\alpha_{41}+\sin\alpha_{12}\sin\alpha_{41}\cos\eta_{\mathrm{L}}=\cos\delta_{\mathrm{L}}=\\&\cos\gamma_1\cos\gamma_2+\sin\gamma_1\sin\gamma_2\cos\delta_{\mathrm{T}}=\cos\delta_{\mathrm{T}}.\end{aligned}\tag{4-19a}$$

For the right side of the transition part,

$$\cos\delta_{\mathrm{T}}=\cos\alpha_{23}\cos\alpha_{34}+\sin\alpha_{23}\sin\alpha_{34}\cos\eta_{\mathrm{R}}.\tag{4-19b}$$

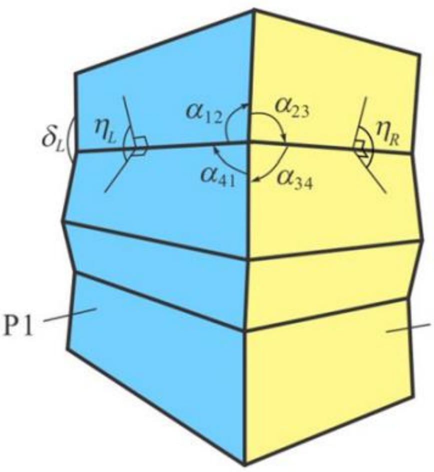

(a)

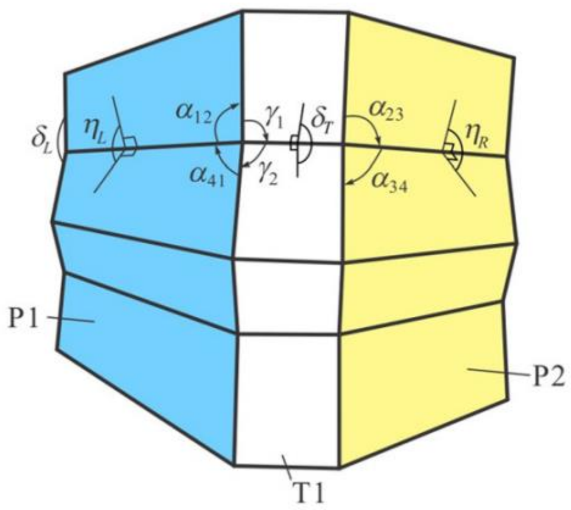

(b)

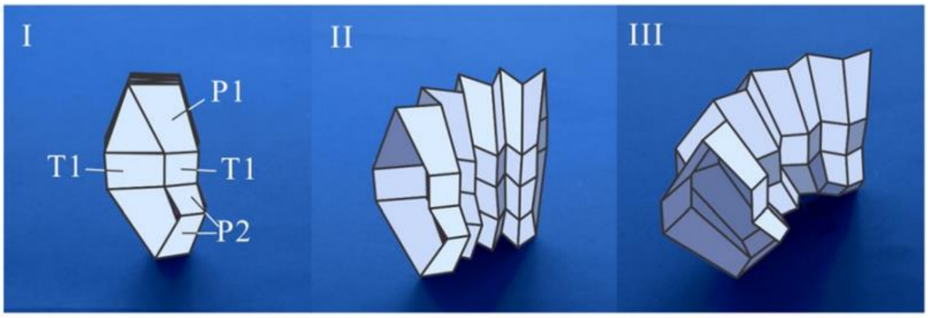

(c)

Fig. 4-13 Multi-layered shifted tube: (a) portion of a curved multi-layered tube; (b) addition of a transition part and (c) folding sequence of a model tube with an added transition pair

Comparing Eqn. (4-19a) with (4-19b) yields the same equation as Eqn. (4-18). Hence, the relationship between two dihedral angles η_{L} and η_{R} is maintained despite the insertion of a transition part made of rectangular facets.

This derivation can also be applied to other facets in the transition part. Consequently, the tube with multiple layers is rigidly foldable when a pair of transition parts consisting of only rectangular facets are appended. A pair is required because in the case, P1 and P2 are only translated.

It remains to be proved whether shifted curved tubes can be produced by adding a transition pair with general parallelogram or trapezoid facets. Figure 4-13(c) shows a curved tube constructed in this manner. The original tube prior to the addition of the transition parts is flat-foldable, and it remains flat-foldable after the addition of a pair of transition parts made of rectangular facets.

4.5 Conclusions

In this chapter, inspired by Goldberg 5*R* and 6*R* linkages, two methods to construct origami tubes using rigid origami tubes are presented. First, several existing tubes are conjoined by merging common sides or corners, resulting in a family of tubes with asymmetric polygonal cross-sections, namely, the combined tubes, which can be constructed by the summation or subtraction of different origami tubes. Next, the transition parts are added into an existing tube, thereby forming shifted tubes in which the crease lines between the neighbouring layers form nonplanar polygons. The combined and shifted tubes are proved to be rigid-foldable and one-DOF according to the kinematical theories of spherical 4*R* linkages. Moreover, these tubes may have an asymmetric planar or nonplanar cross-section. Furthermore, the approach is extended to build multi-layered straight and curved tubes while maintaining the rigid foldability. The proposed approach can be readily utilized to build new structures for engineering applications and offers considerable flexibility to designers in fabricating rigidly foldable tubes to create metamaterials, origami robots, and other devices that require large shape variations. The rigid foldability of these tubes ensures that no facet distortion occurs during the shape change.

Chapter 5 Thick-panel origami tubes

5.1 Introduction

To apply the origami technology to deployable structures where the thickness cannot be disregarded, various methods have been suggested. However, the method of folding rigid origami tubes with thick panels has not been sufficiently investigated. As described in this chapter, a method is developed to fold rigid origami tubes with thick panels, which can reproduce motions identical to those achievable using zero-thickness origami. Moreover, the thick-panel form and zero-thickness form of an origami tube have similar contours.

The layout of this chapter is as follows: Chapter 5.2 induces thick-panel origami tubes with line-symmetric cross-sections, Chapter 5.3 describes planar-symmetric origami tubes, Chapter 5.4 presents multi-layered origami tubes with thick panels, and Chapter 5.5 presents the concluding remarks.

5.2 Line-symmetric tubes

Tubes with parallelogram cross-sections are a type of origami tube with line-symmetric cross-sections. The thick-panel folding technologies of such tubes have been established [80]. However, other line-symmetric rigid origami tubes also exist, such as tubes with hexagonal and octagonal cross-sections, whose thick-panel forms have not been presented yet. A single unit of a zero-thickness origami tube with a line-symmetric hexagonal cross-section is shown in Fig. 5-1, where α and β are considered as the geometrical parameters of the tube. The tube is constructed through parallelogram facets and has six vertexes, A to F, which are divided into three types. The lengths of the sides of the cross-section are $L_{\mathrm{AB}} = L_{\mathrm{DE}}, L_{\mathrm{BC}} = L_{\mathrm{EF}}, L_{\mathrm{CD}} = L_{\mathrm{FA}}$, based on which, the relationships among the lengths of the sides in the thick-panel form can be obtained, since the two forms have similar contours.

The identical vertexes A and D, which contain three mountain crease lines and one valley crease lines, are Miura-ori vertexes. The summation of the sector angles at each Miura-ori vertex equals 2π. Vertexes B and C with four mountain crease lines are convex eggbox-like vertexes. Vertexes E and F with two mountain crease lines and two valley crease lines are concave eggbox-like vertexes. The assignment of the sector angles and mountain-valley crease lines is shown in Fig. 5-1 in which the mountain and valley crease lines are represented by solid and dashed lines, respectively. For different types of vertexes, the thick-panel forms are different.

A Miura-ori vertex, vertex A, and its thick-panel form are shown in Fig. 5-2(a) and (b), respectively, in which the coordinate frames are established according to the D-H notation. The method presented in [80] is used to obtain the form shown in Fig. 5-2(b) in which a Bennett linkage is used to construct the thick-panel form of vertex A, where

$\alpha = 45^{\circ}$ and $\beta = 90^{\circ}$. In the zero-thickness form,

$$\alpha_{12} = \alpha_{41} = \pi - \alpha, \alpha_{23} = \alpha_{34} = \alpha, \tag{5-1a}$$

$$\omega_1 = \pi + \theta_1, \omega_2 = \pi - \theta_2, \omega_3 = \pi - \theta_3, \omega_4 = \pi - \theta_4. \tag{5-1b}$$

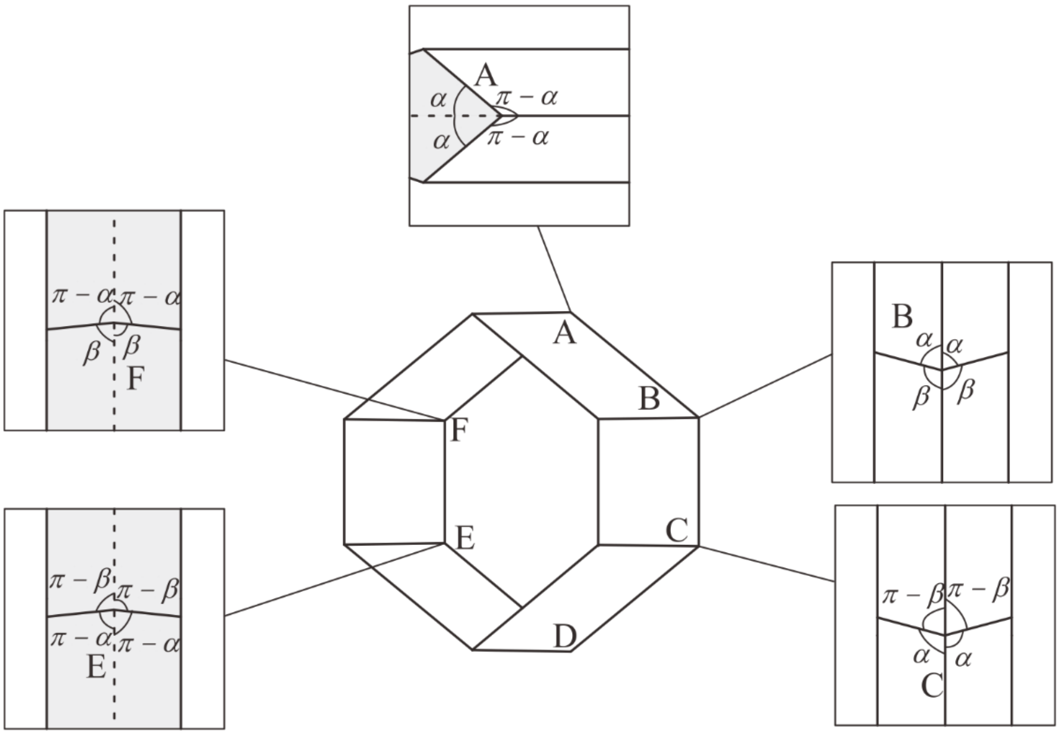

Fig. 5-1 Origami tube with a line-symmetric hexagonal cross-section, and the assignment of the sector angles and mountain-valley crease lines in different types of vertexes.

Here, ω_i represents the dihedral angle between two adjacent panels. Substituting Eqns. (5-1a) and (5-1b) in Eqn. (1-7) yields

$$\omega_1 = \omega_3, \omega_2 = \omega_4, \tag{5-2a}$$

$$\tan(\omega_2 / 2) / \tan(\omega_1 / 2) = \cos\alpha. \tag{5-2b}$$

In the thick-panel form, the following equations are satisfied:

$$\alpha_{12}^{Be} = \alpha, \alpha_{23}^{Be} = \pi - \alpha, \alpha_{34}^{Be} = \alpha, \alpha_{41}^{Be} = \pi - \alpha, \tag{5-3a}$$

$$a_{12} = a_{23} = a_{34} = a_{41} = a, \tag{5-3b}$$

$$\omega_1^{Be} = \theta_1^{Be}, \omega_2^{Be} = \pi - \theta_2^{Be}, \omega_3^{Be} = 2\pi - \theta_3^{Be}, \omega_4^{Be} = \pi + \theta_4^{Be}. \tag{5-3c}$$

Substituting Eqns. (5-3a) to (5-3c) in Eqn. (1-7) yields

$$\omega_1^{Be} = \omega_3^{Be}, \omega_2^{Be} = \omega_4^{Be}, \tag{5-4a}$$

$$\tan(\omega_2^{Be} / 2) / \tan(\omega_1^{Be} / 2) = \cos\alpha. \tag{5-4b}$$

Eqns. (5-2) and (5-4) show that the closure equations for the thick-panel form match those for the zero-thickness form at Miura-ori vertexes A and D.

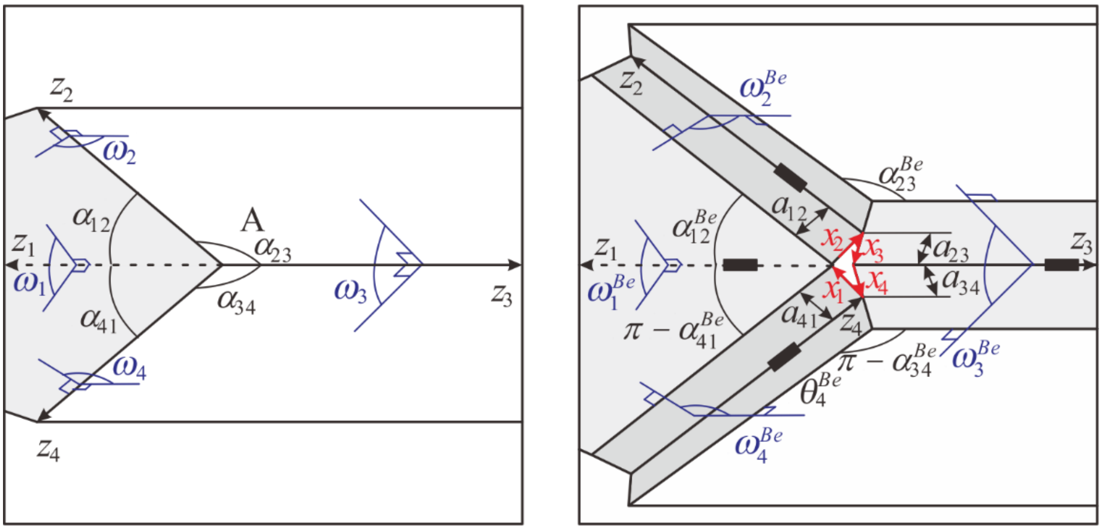

(a) (b)

Fig. 5-2 Miura-ori vertex A: (a) vertex of zero-thickness origami and (b) its corresponding thick-panel form.

For convex eggbox-like vertexes B and C, I adopt spherical 4R linkages in their thick-panel form. Consider vertex B as an example; vertex B and its thick-panel form are shown in Fig. 5-3. The following equations can be obtained in both the zero-thickness form and thick-panel form:

$$\alpha_{12} = \alpha_{41} = \alpha, \alpha_{23} = \alpha_{34} = \beta, \tag{5-5a}$$

$$\omega_1 = \pi - \theta_1, \omega_2 = \pi - \theta_2, \omega_3 = \pi - \theta_3, \omega_4 = \pi - \theta_4. \tag{5-5b}$$

Merging Eqn. (5-5) with Eqn. (1-7) yields

$$\omega_2 = \omega_4, \tag{5-6a}$$

$$\cos^2\alpha + \sin^2\alpha\cos\omega_1 = \cos^2\beta + \sin^2\beta\cos\omega_3, \tag{5-6b}$$

$$\begin{aligned} &\sin^2\alpha\cos\beta\cos\omega_1 + \sin\alpha\sin\beta\cos\alpha\cos\omega_2 \\ &-\sin\alpha\sin\beta\cos\alpha\cos\omega_1\cos\omega_2 \\ &+\sin\alpha\sin\beta\sin\omega_1\sin\omega_2 + \cos^2\alpha\cos\beta - \cos\beta = 0. \end{aligned} \tag{5-6c}$$

Eqns. (5-6a) to (5-6c) are satisfied in both the zero-thickness form and thick-panel form of vertex B. From Eqn. (5-6), it can be infered that the relationships among the dihedral angles in the thick-panel form and zero-thickness form at convex eggbox-like vertexes B and C are identical.

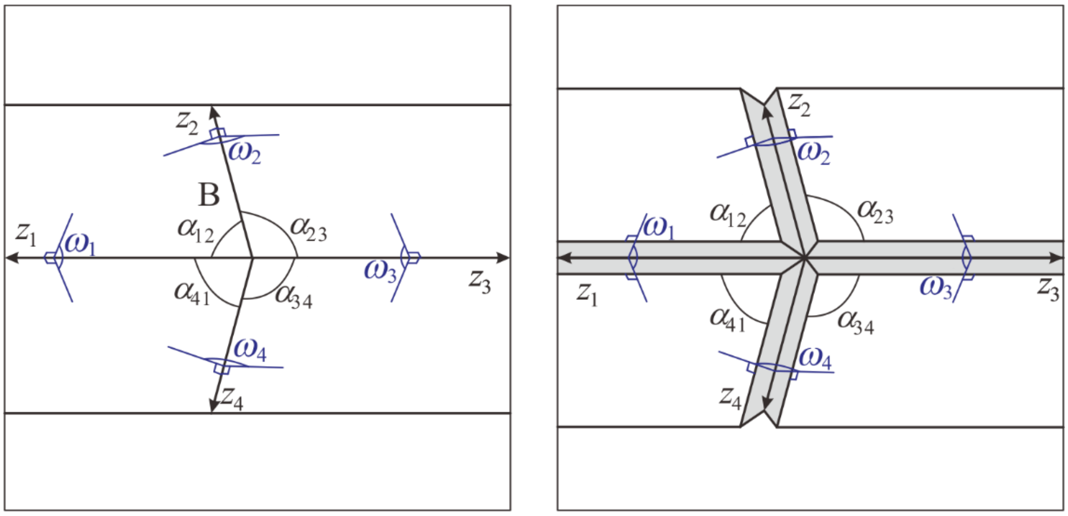

(a) (b)

Fig. 5-3 Convex eggbox-like vertex B: (a) vertex of zero-thickness origami and (b) its corresponding thick-panel form.

For vertexes E and F, since the summation of the sector angles does not equal 2π, the spherical 4*R* linkages cannot be replaced by Bennett linkages [107]. The zero-thickness form and thick-panel form of vertex F are shown in Fig. 5-4. In the zero-thickness form of vertex F (see Fig. 5-4(a)),

$$\alpha_{12} = \alpha_{41} = \beta, \alpha_{23} = \alpha_{34} = \pi - \alpha, \tag{5-7a}$$

$$\omega_1 = \pi + \theta_1, \omega_2 = \pi - \theta_2, \omega_3 = \pi + \theta_3, \omega_4 = \pi - \theta_4. \tag{5-7b}$$

Substituting Eqn. (5-7) in Eqn. (1-8) yields

$$\omega_2 = \omega_4, \tag{5-8a}$$

$$\cos^2\beta + \sin^2\beta\cos\omega_1 = \cos^2\alpha + \sin^2\alpha\cos\omega_3, \tag{5-8b}$$

$$\begin{aligned} &\sin\alpha\sin\beta\cos\alpha\cos\omega_2 - \sin^2\alpha\cos\beta\cos\omega_3 \\ &-\sin\alpha\sin\beta\cos\alpha\cos\omega_2\cos\omega_3 \\ &+\sin\alpha\sin\beta\sin\omega_2\sin\omega_3 - \cos^2\alpha\cos\beta + \cos\beta = 0. \end{aligned} \tag{5-8c}$$

For the thick-panel form (see Fig. 5-4(b)), I use Bricard linkages to replace the spherical 4*R* linkages in the original zero-thickness form, and two links are added to form the plane-symmetric Bricard linkage in which

$$a_{12} = a_{61} = b, \alpha_{23} = \alpha_{34} = \alpha_{45} = \alpha_{56} = 2a, \tag{5-9a}$$

$$\begin{aligned} \alpha_{12}^{Br} &= 2\pi - \alpha_{61}^{Br} = 0, \\ \alpha_{56}^{Br} &= 2\pi - \alpha_{23}^{Br} = \beta, \\ \alpha_{34}^{Br} &= 2\pi - \alpha_{45}^{Br} = \pi - \alpha, \end{aligned} \tag{5-9b}$$

$$\begin{aligned} R_1 &= R_2 = R_4 = R_6 = 0, \\ R_3 &= -R_5 = R. \end{aligned} \tag{5-9c}$$

The kinematics of the plane-symmetric Bricard linkages have been analysed in [120]. In a plane-symmetric Bricard linkage where the z_1 and z_4-axes are on the symmetric plane, the following equations should be satisfied:

$$\theta_3 = \theta_5, \theta_2 = \theta_6, \tag{5-10a}$$

$$a_{12} = a_{61} = a_1, a_{23} = a_{56} = a_2, a_{34} = a_{45} = a_3, \tag{5-10b}$$

$$\begin{aligned} \alpha_{12}^{Br} &= 2\pi - \alpha_{61}^{Br} = 0, \\ \alpha_{56}^{Br} &= 2\pi - \alpha_{23}^{Br} = \beta, \\ \alpha_{34}^{Br} &= 2\pi - \alpha_{45}^{Br} = \pi - \alpha, \end{aligned} \tag{5-10c}$$

$$A\tan^2(\theta_3/2) + B\tan(\theta_3/2) + C = 0. \tag{5-10d}$$

Moreover,

$$\begin{aligned} A = &(a_1 - a_2 + a_3)\sin(\beta_1 - \beta_2 + \beta_3)\tan^2(\theta_2/2) \\ &+2\sin\beta_1(R_3\sin\beta_3 + R_2\sin(\beta_3 - \beta_2))\tan(\theta_2/2) \\ &+(a_1 + a_2 - a_3)\sin(\beta_1 + \beta_2 - \beta_3), \end{aligned} \tag{5-10e}$$

$$\begin{aligned} B = &2\sin\beta_3(R_2\sin\beta_1 + R_3\sin(\beta_1 - \beta_2))\tan^2(\theta_2/2) \\ &+2((a_1 - a_3)\sin(\beta_1 - \beta_3) \\ &-(a_1 + a_3)\sin(\beta_1 + \beta_3))\tan(\theta_2/2) \\ &-2\sin\beta_3(R_2\sin\beta_1 + R_3\sin(\beta_1 + \beta_2)) \end{aligned} \tag{5-10f}$$

$$\begin{aligned} C = &(a_1 - a_2 - a_3)\sin(\beta_1 - \beta_2 - \beta_3)\tan^2(\theta_2/2) \\ &+2\sin\beta_1(R_3\sin\beta_3 + R_2\sin(\beta_3 + \beta_2))\tan(\theta_2/2) \\ &+(a_1 + a_2 + a_3)\sin(\beta_1 + \beta_2 + \beta_3), \end{aligned} \tag{5-10g}$$

and

$$\begin{aligned} \tan(\theta_1/2) = &(\sin\beta_3(\cos\theta_2\sin\theta_3 + \cos\beta_2\sin\theta_2\cos\theta_3) + \cos\beta_3\sin\beta_2\sin\theta_2) \\ &/(\sin\beta_1\sin\beta_2\sin\beta_3\cos\theta_3 - \cos\beta_1\sin\beta_2\cos\beta_3\cos\theta_2 - \sin\beta_1\cos\beta_2\cos\beta_3 \\ &-\cos\beta_1\cos\beta_2\sin\beta_3\cos\theta_2\cos\theta_3 + \cos\beta_1\sin\beta_3\sin\theta_2\sin\theta_3), \end{aligned} \tag{5-10h}$$

$$\begin{aligned} \tan(\theta_4/2) = &(\sin\beta_1\sin\theta_2\cos\theta_3 + \sin\theta_3(\sin\beta_1\cos\beta_2\cos\theta_2 + \cos\beta_1\sin\beta_2)) \\ &/(\cos\beta_3(\sin\beta_1\sin\theta_2\sin\theta_3 - \sin\beta_1\cos\beta_2\cos\theta_2\cos\theta_3 - \cos\beta_1\sin\beta_2\cos\theta_3) \\ &+\sin\beta_3(\sin\beta_1\sin\beta_2\cos\theta_2 - \cos\beta_1\cos\beta_2)). \end{aligned} \tag{5-10i}$$

Substituting Eqn. (5-9) in (5-10) yields

$$\theta_3^{Br} = \theta_5^{Br}, \theta_2^{Br} = \theta_6^{Br}, \tag{5-11a}$$

$$A\tan^2(\theta_3^{Br}/2) + B\tan(\theta_3^{Br}/2) + C = 0. \tag{5-11b}$$

In this case,

$$A = b\sin(\alpha-\beta)\tan^2(\theta_2^{Br}/2) - b\sin(\alpha-\beta), \tag{5-12a}$$

$$B = 2R\sin\alpha\sin\beta\tan^2(\theta_2^{Br}/2) - 4b\sin\alpha\tan(\theta_2^{Br}/2) + 2R\sin\alpha\sin\beta, \tag{5-12b}$$

$$C = (4a-b)\sin(\alpha+\beta)\tan^2(\theta_2^{Br}/2) + 4a\sin(\alpha+\beta), \tag{5-12c}$$

and

$$\tan(\theta_3^{Br}/2) = (-B \pm \sqrt{B^2-4AC})/(2A), \tag{5-13a}$$

$$\begin{aligned}\tan(\theta_1^{Br}/2) = &(\sin\alpha(\cos\theta_2^{Br}\sin\theta_3^{Br} + \cos\beta\sin\theta_2^{Br}\cos\theta_3^{Br}) + \cos\alpha\sin\beta\sin\theta_2^{Br}) \\ &/(\sin\alpha\sin\theta_2^{Br}\sin\theta_3^{Br} - \cos\alpha\sin\beta\cos\theta_2^{Br} - \sin\alpha\cos\beta\cos\theta_2^{Br}\cos\theta_3^{Br}),\end{aligned} \tag{5-13b}$$

$$\tan(\theta_4^{Br}/2) = \sin\beta\sin\theta_3^{Br}/(\cos\alpha\sin\beta\cos\theta_3^{Br} - \sin\alpha\cos\beta). \tag{5-13c}$$

According to the spherical cosine formula,

$$\cos^2\beta + \sin^2\beta\cos\omega_1^{Br} = \cos^2\alpha + \sin^2\alpha\cos\omega_3^{Br}. \tag{5-14}$$

The relationships among the dihedral angles and twist angles are as follows:

$$\omega_2^{Br} = \theta_3^{Br}, \omega_3^{Br} = 2\pi - \theta_4^{Br}, \omega_4^{Br} = \theta_5^{Br}. \tag{5-15}$$

Substituting Eqn. (5-15) in Eqns. (5-13) yields

$$\omega_2^{Br} = \omega_4^{Br}, \tag{5-16a}$$

$$\begin{aligned}&\sin\alpha\sin\beta\cos\alpha\cos\omega_2^{Br} - \sin^2\alpha\cos\beta\cos\omega_3^{Br} \\ &-\sin\alpha\sin\beta\cos\alpha\cos\omega_2^{Br}\cos\omega_3^{Br} \\ &+\sin\alpha\sin\beta\sin\omega_2^{Br}\sin\omega_3^{Br} - \cos^2\alpha\cos\beta + \cos\beta = 0.\end{aligned} \tag{5-16b}$$

According to Eqns. (5-14) and (5-16), the closure equations for the thick-panel form match those for the zero-thickness form at concave eggbox-like vertexes E and F, as illustrated in Fig. 5-4(c).

It can be concluded that in the thick-panel form, the closure equations at each type of vertex match those for the zero-thickness form, which indicates that the thick-panel form of the origami tube with a line-symmetric hexagonal cross-section can reproduce the motions achievable using the original zero-thickness form. Figure 5-5 shows the deployment process of a unit of the origami tube with a line-symmetric hexagonal cross-section in which $\alpha = 45^{\circ}$ and $\beta = 90^{\circ}$.

Moreover, thick-panel origami tubes whose cross-sections are line-symmetric concave polygons can be obtained. Figure 5-6 shows a single unit of a tube with concave hexagonal cross-section as well as the assignment of sector angles and mountain-valley crease lines at each vertex. In contrast to the tube shown in Fig. 5-1, this tube does not have any convex and concave eggbox-like vertexes.

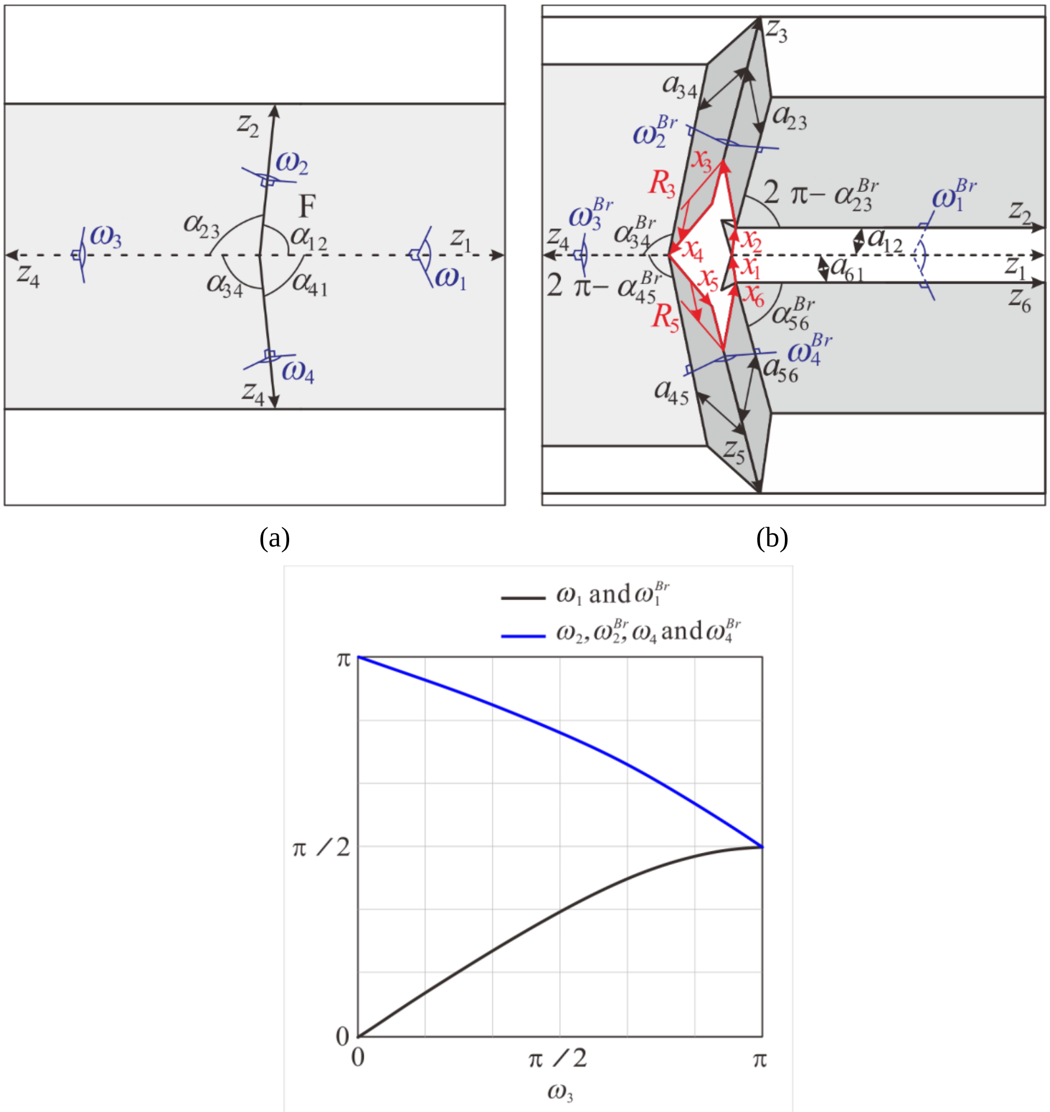

Fig. 5-4 Concave eggbox-like vertex F: (a) vertex of zero-thickness origami; (b) its corresponding thick-panel form and (c) the relationships among the dihedral angles.

The identical Miura-ori vertexes A and D have one mountain crease lines and three valley crease lines. Vertexes B, C, E and F have three mountain crease lines and one valley crease lines and are known as Miura-like vertexes since the summation of the sector angles does not equal 2π.

It has been proved that for the Miura-ori vertexes A and D, the closure equations match those for the zero-thickness form. The link lengths of the Bennett linkages are *a*. For the thick-panel form of vertexes B, C, E and F, Bricard linkages are used instead of the original spherical 4*R* linkages.

Two links are added to one valley crease line in the thick-panel form of vertexes B and C. Considering vertex B as an example, the zero-thickness form and its corresponding thick-panel form are illustrated in Fig. 5-7, in which $\alpha = 75^{\circ}$ and

$\beta = 90^{\circ}$.

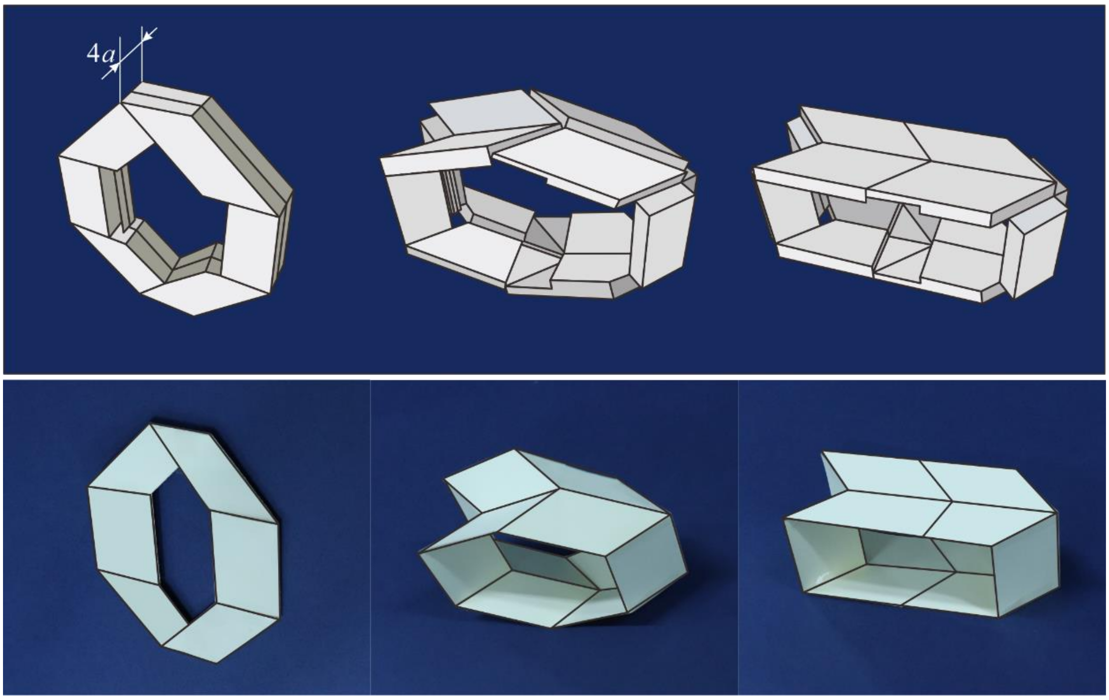

Fig. 5-5 Deployment process of a single unit of the thick-panel form (top) and its corresponding zero-thickness form (bottom) of an origami tube with a line-symmetric hexagonal cross-section.

In the zero-thickness form (Fig. 5-7(a)),

$$\alpha_{12} = \alpha_{41} = \beta, \alpha_{23} = \alpha_{34} = \pi - \alpha, \tag{5-17a}$$

$$\omega_1 = \pi + \theta_1, \omega_2 = \pi - \theta_2, \omega_3 = \pi - \theta_3, \omega_4 = \pi - \theta_4. \tag{5-17b}$$

Substituting Eqn. (5-17) in Eqn. (1-7) yields

$$\omega_2 = \omega_4, \tag{5-18a}$$

$$\cos^2\beta + \sin^2\beta\cos\omega_1 = \cos^2\alpha + \sin^2\alpha\cos\omega_3, \tag{5-18b}$$

$$\begin{aligned}&\sin\alpha\sin\beta\cos\alpha\cos\omega_2 - \sin^2\alpha\cos\beta\cos\omega_3\\&-\sin\alpha\sin\beta\cos\alpha\cos\omega_2\cos\omega_3\\&-\sin\alpha\sin\beta\sin\omega_2\sin\omega_3 - \cos^2\alpha\cos\beta + \cos\beta = 0,\end{aligned} \tag{5-18c}$$

For the thick-panel form (Fig. 5-7(b)), the following equations can be obtained:

$$a_{12} = a_{61} = b, a_{23} = a_{56} = a/2, a_{34} = a_{45} = a, \tag{5-19a}$$

$$\begin{aligned}&\alpha_{12}^{Br} = 2\pi - \alpha_{61}^{Br} = 0,\\&\alpha_{56}^{Br} = 2\pi - \alpha_{23}^{Br} = \beta,\\&\alpha_{45}^{Br} = 2\pi - \alpha_{34}^{Br} = \pi - \alpha,\end{aligned} \tag{5-19b}$$

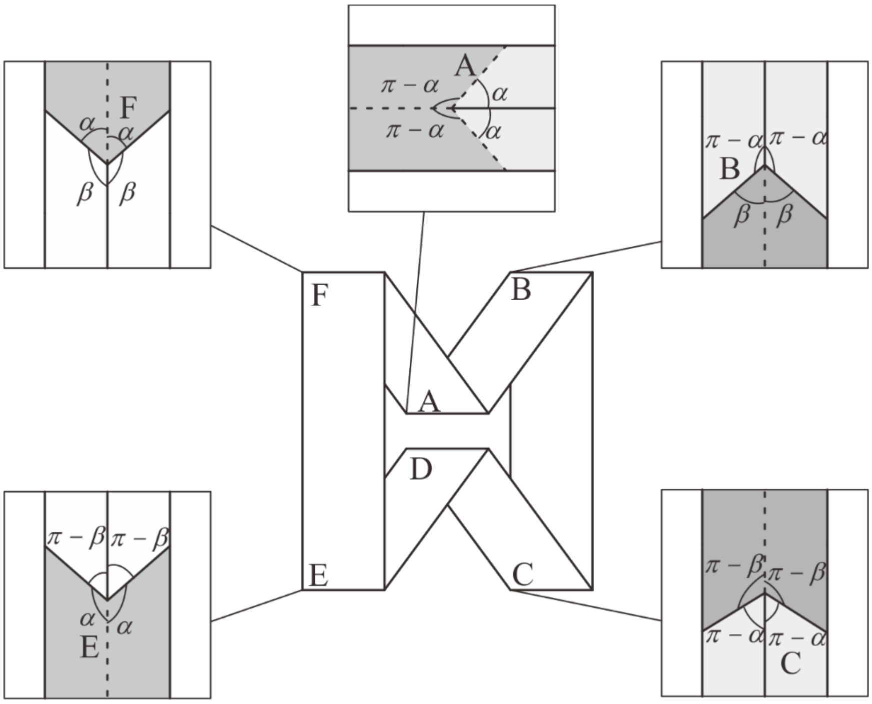

Fig. 5-6 Origami tube with line-symmetric concave cross-sections, and the assignment of the sector angles in different types of vertexes.

$$\begin{aligned} &R_1 = R_2 = R_4 = R_6 = 0, \\ &R_3 = -R_5 = R, \end{aligned} \tag{5-19c}$$

$$\omega_2^{Br} = \theta_3^{Br} - \pi, \omega_3^{Br} = \theta_4^{Br}, \omega_4^{Br} = \theta_5^{Br} - \pi. \tag{5-19d}$$

Merging Eqn. (5-19) with Eqn. (5-10) yields

$$\omega_2^{Br} = \omega_4^{Br}, \tag{5-20a}$$

$$\begin{aligned} &\sin\alpha\sin\beta\cos\alpha\cos\omega_2^{Br} - \sin^2\alpha\cos\beta\cos\omega_3^{Br} \\ &-\sin\alpha\sin\beta\cos\alpha\cos\omega_2^{Br}\cos\omega_3^{Br} \\ &-\sin\alpha\sin\beta\sin\omega_2^{Br}\sin\omega_3^{Br} - \cos^2\alpha\cos\beta + \cos\beta = 0, \end{aligned} \tag{5-20b}$$

According to the spherical cosine formula,

$$\cos^2\beta + \sin^2\beta\cos\omega_1^{Br} = \cos^2\alpha + \sin^2\alpha\cos\omega_3^{Br}, \tag{5-21}$$

According to Eqns. (5-20) and (5-21), the closure equations for the thick-panel form match those for the zero-thickness form at Miura-like vertexes B and C, as illustrated in Fig. 5-7(c).

For Miura-like vertexes E and F, two links are added to one mountain crease line in the thick-panel form. The zero-thickness form and thick-panel form of vertex F, which is considered as an example, are illustrated in Fig. 5-8 wherein the axes in grey are the two axes that cannot be seen from the point of view.

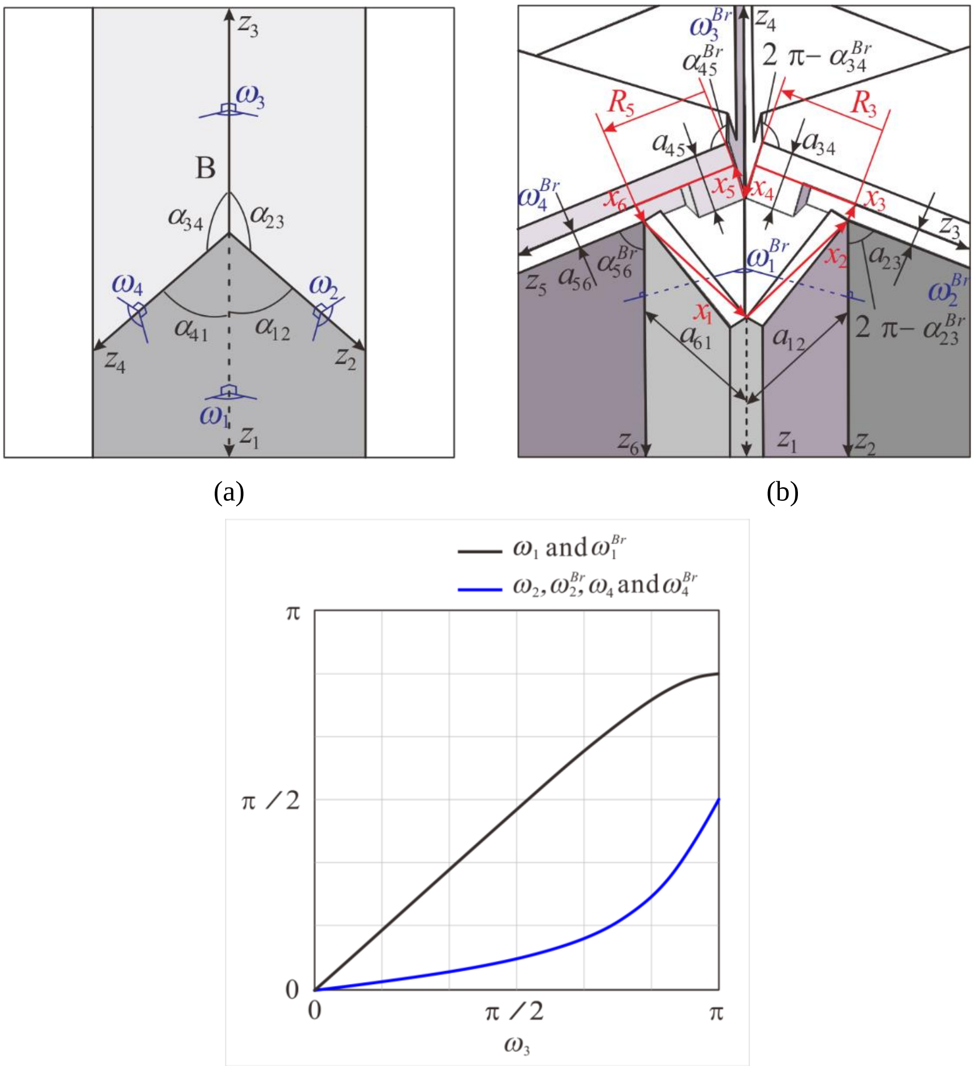

Fig. 5-7 Miura-like vertex B: (a) vertex of zero-thickness origami; (b) its corresponding thick-panel form and (c) the relationships among the dihedral angles.

For the zero-thickness form (Fig. 5-8(a)),

$$\alpha_{12} = \alpha_{41} = \beta, \alpha_{23} = \alpha_{34} = \alpha, \tag{5-22a}$$

$$\omega_1 = \pi - \theta_1, \omega_2 = \pi - \theta_2, \omega_3 = \pi + \theta_3, \omega_4 = \pi - \theta_4. \tag{5-22b}$$

Merging Eqns. (5-22) and (1-7) yields

$$\omega_2 = \omega_4, \tag{5-23a}$$

$$\cos^2\beta + \sin^2\beta\cos\omega_1 = \cos^2\alpha + \sin^2\alpha\cos\omega_3, \tag{5-23b}$$

$$\begin{aligned} &\sin\alpha\sin\beta\cos\alpha\cos\omega_2 + \sin^2\alpha\cos\beta\cos\omega_3 \\ &-\sin\alpha\sin\beta\cos\alpha\cos\omega_2\cos\omega_3 \\ &-\sin\alpha\sin\beta\sin\omega_2\sin\omega_3 + \cos^2\alpha\cos\beta - \cos\beta = 0, \end{aligned} \tag{5-23c}$$

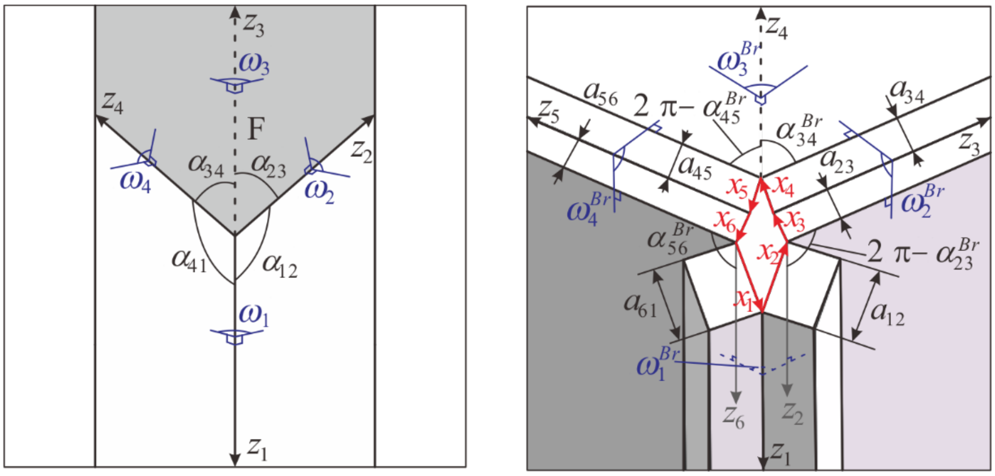

(a) (b)

Fig. 5-8 Miura-like vertex F: (a) vertex of zero-thickness origami and (b) its corresponding thick-panel form.

In the thick-panel form (Fig. 5-8(b)), the following equations are satisfied:

$$a_{12} = a_{61} = c, a_{23} = a_{56} = a/2, a_{34} = a_{45} = a, \tag{5-24a}$$

$$\begin{aligned} \alpha_{12}^{Br} &= 2\pi - \alpha_{61}^{Br} = 0, \\ \alpha_{56}^{Br} &= 2\pi - \alpha_{23}^{Br} = \beta, \\ \alpha_{34}^{Br} &= 2\pi - \alpha_{45}^{Br} = \alpha, \end{aligned} \tag{5-24b}$$

$$R_1 = R_2 = R_3 = R_4 = R_5 = R_6 = 0, \tag{5-24c}$$

$$\omega_2^{Br} = \theta_3^{Br}, \omega_3^{Br} = \theta_4^{Br}, \omega_4^{Br} = \theta_5^{Br}. \tag{5-24d}$$

According to the spherical cosine formula,

$$\cos^2\beta + \sin^2\beta\cos\omega_1^{Br} = \cos^2\alpha + \sin^2\alpha\cos\omega_3^{Br}, \tag{5-25}$$

Substituting Eqn. (5-24) in Eqn. (5-10) yields

$$\omega_2^{Br} = \omega_4^{Br}, \tag{5-26a}$$

$$\begin{aligned} &\sin\alpha\sin\beta\cos\alpha\cos\omega_2^{Br} + \sin^2\alpha\cos\beta\cos\omega_3^{Br} \\ &-\sin\alpha\sin\beta\cos\alpha\cos\omega_2^{Br}\cos\omega_3^{Br} \\ &-\sin\alpha\sin\beta\sin\omega_2^{Br}\sin\omega_3^{Br} + \cos^2\alpha\cos\beta - \cos\beta = 0, \end{aligned} \tag{5-26b}$$

Equations (5-25) and (5-26), which match Eqn. (5-23), indicate that the motion of the thick-panel form of vertex F matches that of the zero-thickness form. Since the thick-panel form of vertex E is similar to that of vertex F, at both Miura-like vertexes E and F, the motion in the thick-panel form matches that of the zero-thickness form.

In the concave tube, the motions of each vertex match those of the zero-thickness form; hence, this tube can reproduce the motions achievable using the original zero-thickness form. The deployment process of a thick-panel concave line-symmetric tube along with its zero-thickness form are illustrated in Fig. 5-9, where $\alpha = 75^{\circ}$ and $\beta = 90^{\circ}$.

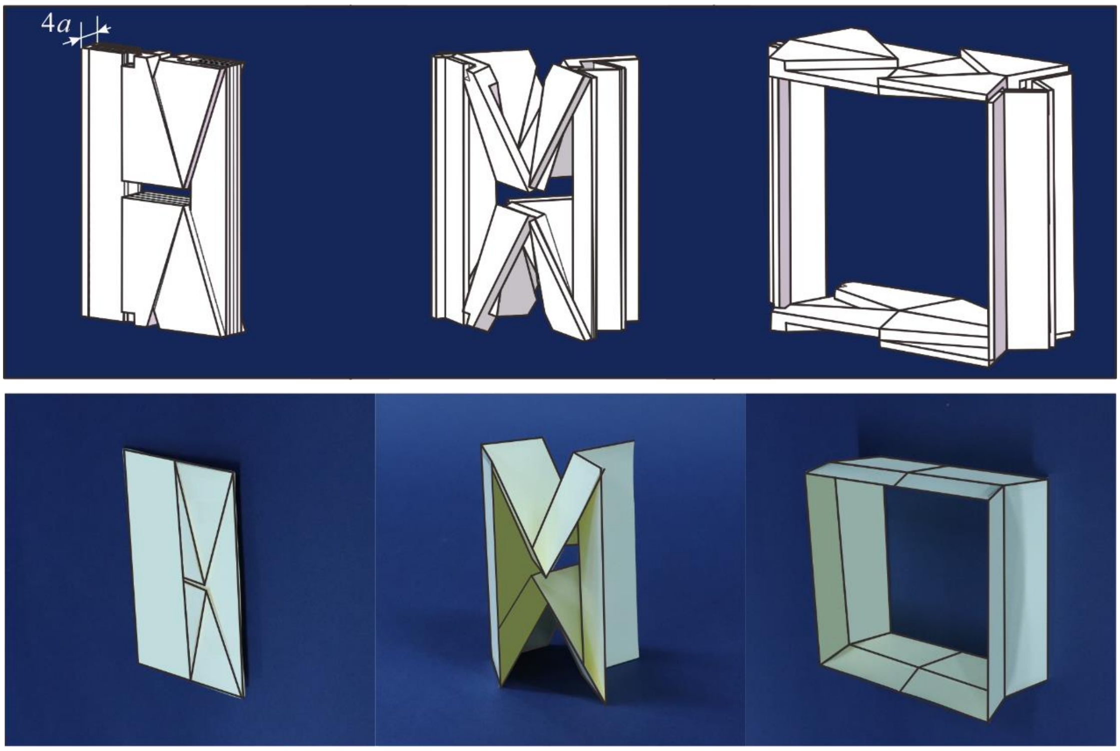

Fig. 5-9 Folding process of a thick-panel tube with concave hexagonal cross-sections (top) and its zero-thickness form (bottom).

5.3 Planer symmetric tubes

Thick-panel origami tubes with planar-symmetric hexagonal cross-sections can be constructed using a method similar to that described in Chapter 5.2. Figure 5-10 shows an origami tube with a planar-symmetric convex hexagonal cross-section, along with the assignment of the sector angles and mountain-valley crease lines at each vertex. The relationships among the lengths of the sides of the cross-section are $L_{\mathrm{AB}} = L_{\mathrm{AF}}, L_{\mathrm{BC}} = L_{\mathrm{FE}}, L_{\mathrm{CD}} = L_{\mathrm{ED}}$.

For a line-symmetric origami tube, the tube has a thick-panel form only when the two Miura-ori vertexes are identical.

To fold a thick-panel origami tube with planar-symmetric hexagonal cross-sections, the two Miura-ori vertexes of the original tube should be identical, and the lengths of the tube should satisfy the following equation:

$$L_{\mathrm{AB}} \cos\alpha + L_{\mathrm{BC}} \cos\beta = L_{\mathrm{CD}} \cos\alpha \tag{5-27}$$

The tube has three types of vertexes, identical Miura-ori vertexes A and D, convex eggbox-like vertexes B and C, and concave eggbox-like vertexes E and F. This tube can be constructed using the method described in Chapter 5.2, and the motion of the thick-panel form matches that of the original zero-thickness form. The deployment process of both the thick-panel form and zero-thickness form of a tube with a planar-symmetric hexagonal cross-section is illustrated in Fig. 5-11

An origami tube with concave hexagonal cross-sections and the assignment of the sector angles and mountain-valley crease lines are shown in Fig. 5-12. To obtain the corresponding thick-panel form, Eqn. (5-27) is satisfied in the tube. In this tube, vertexes A and D are identical Miura-ori vertexes, vertex F is a concave eggbox-like vertex, vertexes C and E are Miura-like vertexes, and vertex B is a convex eggbox-like vertex. The methods of constructing the thick-panel forms of vertexes A, C, D, E and F are similar to those mentioned previously in this chapter, owing to which, the thick-panel forms exhibit equivalent motions as those achievable using the zero-thickness forms. However, the construction method of the thick-panel form at vertex B is different from the method described in Chapter 5.2.

The zero-thickness form and thick-panel form of vertex B are illustrated in Fig. 5-13. Though vertex B is a convex eggbox-like vertex, it is connected to vertex E, at which two links are added to the mountain crease line to construct a Bricard linkage. Consequently, a spherical 4*R* linkage cannot be used to establish the thick-panel form of vertex B. Hence, a Bricard linkage is adopted. The coordinate frames are established according to the D-H notation shown in Fig. 5-13, where $\alpha = 75^{\circ}$ and $\beta = 105^{\circ}$. In the zero-thickness form (see Fig. 5-13(a)),

$$\alpha_{12} = \alpha_{41} = \alpha, \alpha_{23} = \alpha_{34} = \beta, \tag{5-28a}$$

$$\omega_1 = \pi - \theta_1, \omega_2 = \pi - \theta_2, \omega_3 = \pi - \theta_3, \omega_4 = \pi - \theta_4. \tag{5-28b}$$

Merging Eqn. (5-28) with Eqn. (1-7) yields

$$\omega_2 = \omega_4, \tag{5-29a}$$

$$\cos^2\beta + \sin^2\beta\cos\omega_1 = \cos^2\alpha + \sin^2\alpha\cos\omega_3, \tag{5-29b}$$

$$\begin{aligned} &\sin^2\alpha\cos\beta\cos\omega_3 + \sin\alpha\sin\beta\cos\alpha\cos\omega_2 \\ &-\sin\alpha\sin\beta\cos\alpha\cos\omega_3\cos\omega_2 \\ &+\sin\alpha\sin\beta\sin\omega_3\sin\omega_2 + \cos^2\alpha\cos\beta - \cos\beta = 0. \end{aligned} \tag{5-29c}$$

In the thick-panel form, which is shown in Fig. 5-13(b), links 12 and 61 are the two added links, and

$$a_{12} = a_{61} = c, a_{23} = a_{56} = a/2, a_{34} = a_{45} = a/2, \tag{5-30a}$$

$$\begin{aligned} \alpha_{12}^{Br} &= 2\pi - \alpha_{61}^{Br} = 0, \\ \alpha_{56}^{Br} &= 2\pi - \alpha_{23}^{Br} = \beta, \\ \alpha_{45}^{Br} &= 2\pi - \alpha_{34}^{Br} = \alpha, \end{aligned} \tag{5-30b}$$

$$R_1 = R_3 = R_4 = R_5 = 0, R_2 = -R_6 \tag{5-30c}$$

$$\omega_2^{Br} = \theta_3^{Br} - \pi, \omega_3^{Br} = \theta_4^{Br}, \omega_4^{Br} = \theta_5^{Br} - \pi. \tag{5-30d}$$

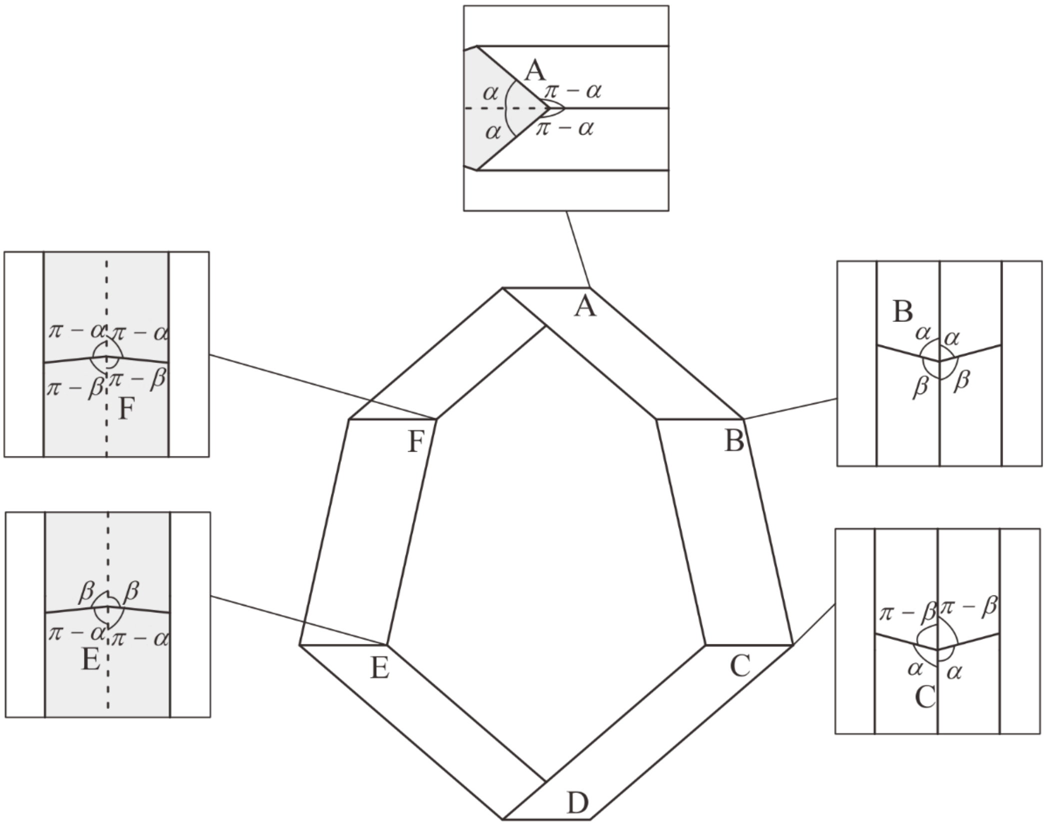

Fig. 5-10 Origami tube with planar-symmetric hexagonal cross-sections, and the assignment of the sector angles and mountain-valley crease lines in different types of vertexes.

According to the spherical cosine formula,

$$\cos^2\beta + \sin^2\beta\cos\omega_1^{Br} = \cos^2\alpha + \sin^2\alpha\cos\omega_3^{Br}, \tag{5-31}$$

Substituting Eqn. (5-24) in Eqn. (5-10) yields

$$\omega_2^{Br} = \omega_4^{Br}, \tag{5-32a}$$

$$\begin{aligned}&\sin\alpha\sin\beta\cos\alpha\cos\omega_3^{Br} + \sin^2\alpha\cos\beta\cos\omega_2^{Br}\\ &-\sin\alpha\sin\beta\cos\alpha\cos\omega_3^{Br}\cos\omega_2^{Br}\\ &+\sin\alpha\sin\beta\sin\omega_2^{Br}\sin\omega_3^{Br} + \cos^2\alpha\cos\beta - \cos\beta = 0.\end{aligned} \tag{5-32b}$$

It can be noted that Eqns. (5-31) and (5-32) match Eqn. (5-29), which indicates that the motions of the two forms of vertex B also match, as illustrated in Fig. 5-13(c). The deployment process of a concave tube with planar-symmetric hexagonal cross-sections is shown in Fig. 5-14, where $\alpha = 75^{\circ}$ and $\beta = 105^{\circ}$.

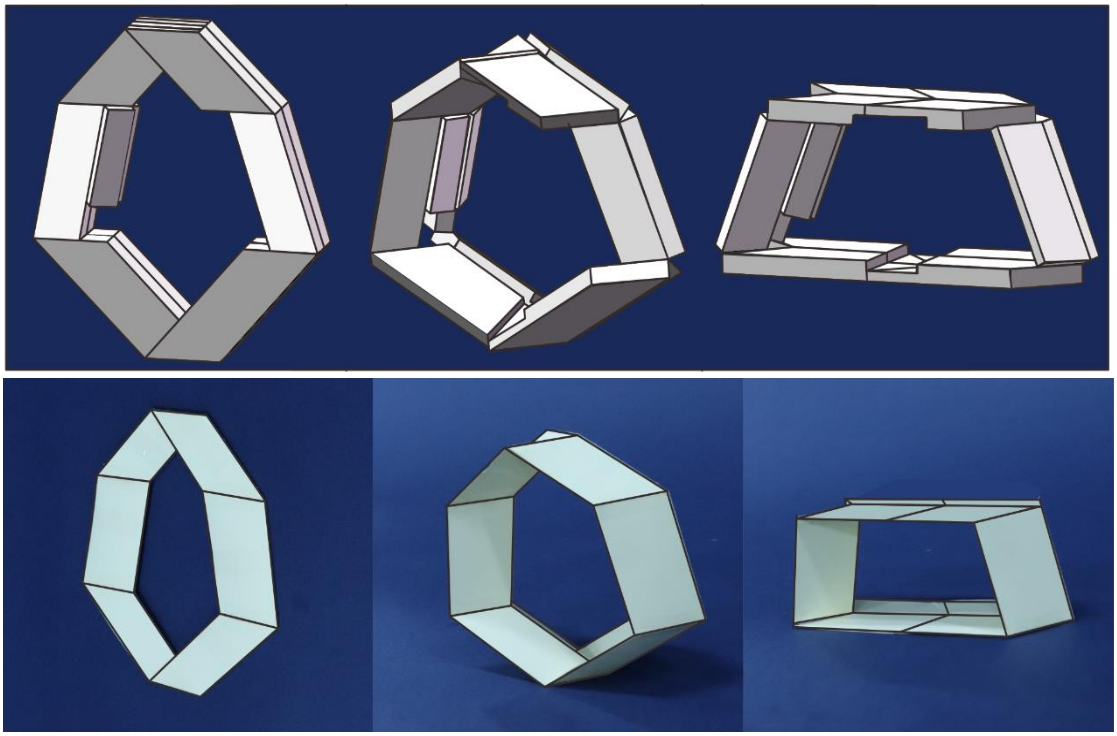

Fig. 5-11 Thick-panel form of an origami tube with planar-symmetric hexagonal cross-sections (top) and its zero-thickness form (bottom).

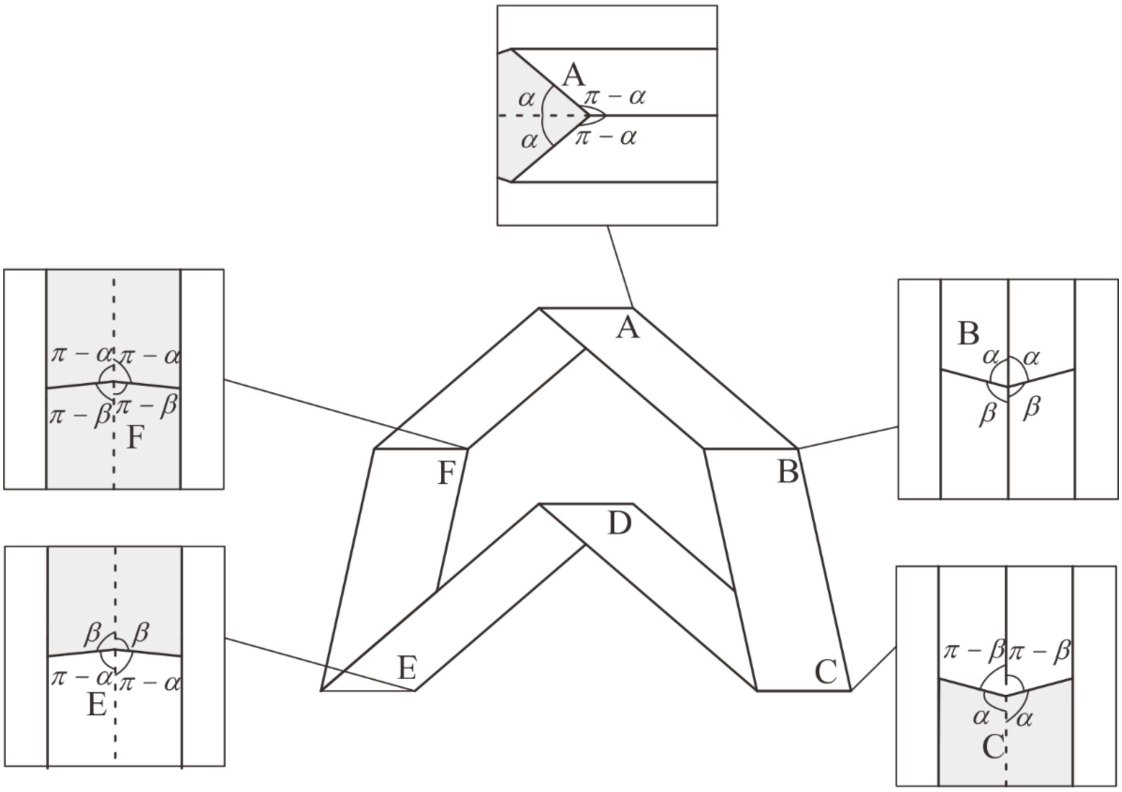

Fig. 5-12 Origami tube with concave planar-symmetric hexagonal cross-sections, and the assignment of sector angles and mountain-valley crease lines in different types of vertexes.

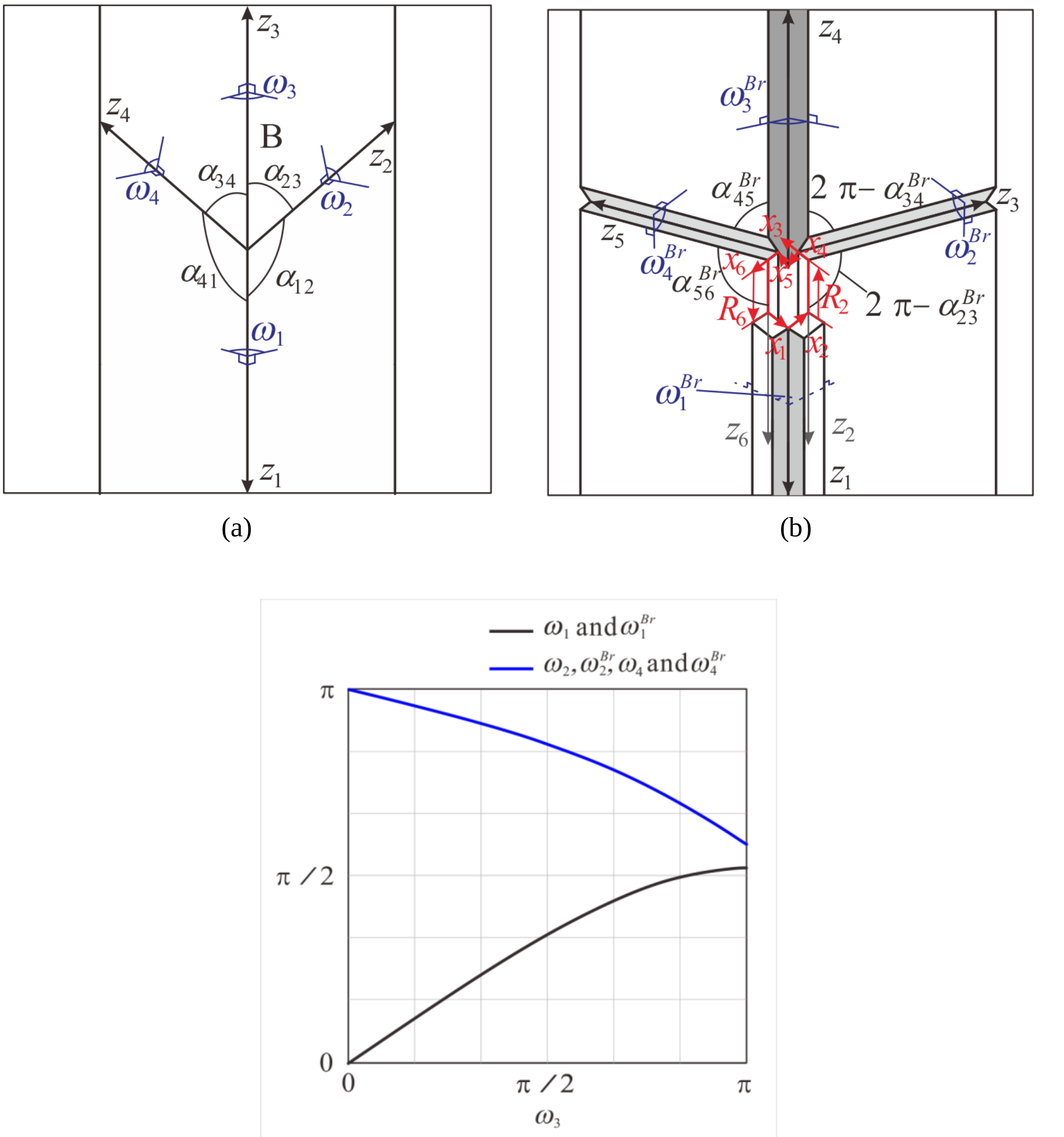

(a) (b)

(c)

Fig. 5-13 Convex eggbos-like vertex B: (a) vertex of zero-thickness origami; (b) its corresponding thick-panel form and (c) the relationships among the dihedral angles.

5.4 Discussion of thick-panel origami tubes

The method of constructing the thick-panel form of each type of vertex in an origami tube has been introduced. Next, the thick-panel form of multi-layered and curved tubes will be examined.

5.4.1 Multi-layered tubes

The tubes described in Chapters 5.2 and 5.3 can be repeated in the axial direction to construct multi-layered thick-panel origami tubes.

To construct the Bricard linkages in the multi-layered thick-panel origami tube, extra links must be added. To facilitate the manufacturing of the thick-panel tube, the simplification of the thick-panel form is considered. In the connection between two concave eggbox-like vertexes, the extra links added to the common valley crease lines can be removed. As illustrated in Fig. 5-15(a), vertexes E and F are two connected concave eggbox-like vertexes in the tube shown in Fig. 5-10, and Fig. 5-15(b) shows the process of removing the extra links. After removing the two links, the connected two Bricard linkages become a single Bricard linkage in which

$$a_{12} = a_{61}, a_{23} = a_{56} = L_{\mathrm{EF}} \cos(\pi - \beta), a_{34} = a_{45}, \tag{5-33a}$$

$$\begin{aligned} \alpha_{61}^{Br} &= 2\pi - \alpha_{12}^{Br} = \pi - \alpha, \\ \alpha_{56}^{Br} &= 2\pi - \alpha_{23}^{Br} = 0, \\ \alpha_{34}^{Br} &= 2\pi - \alpha_{45}^{Br} = \pi - \alpha, \end{aligned} \tag{5-33b}$$

$$R_1 = R_2 = R_4 = R_6 = 0, R_3 = -R_5. \tag{5-33c}$$

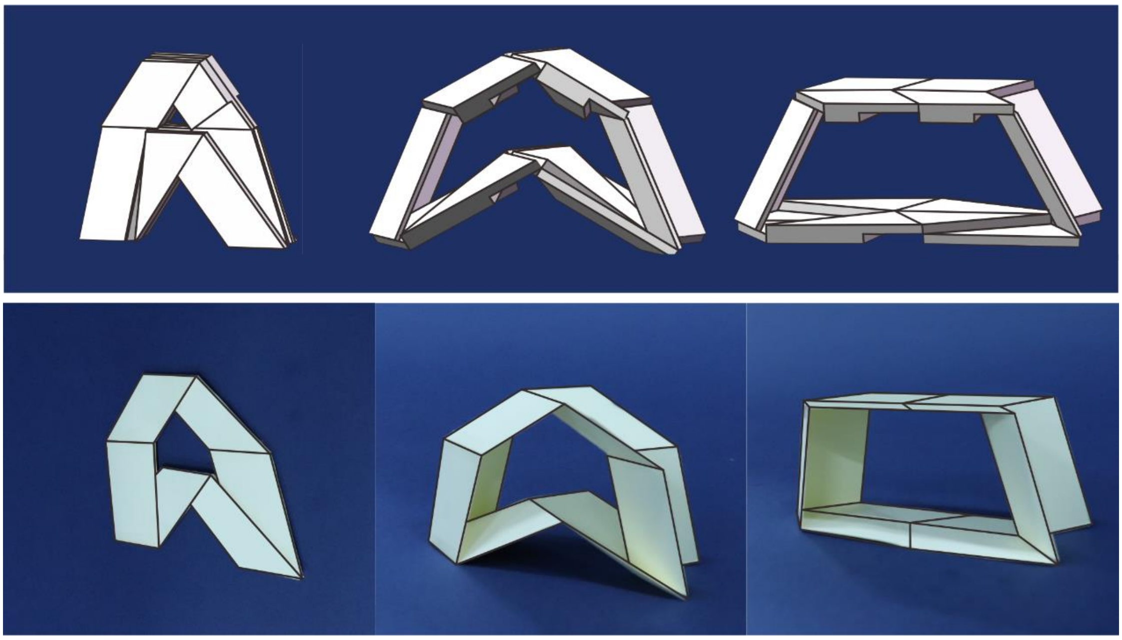

Fig. 5-14 Thick-panel form of an origami tube with concave planar-symmetric hexagonal cross-sections (top) and its zero-thickness form (bottom).

Since the thick-panel form of the origami tube has no bifurcation, removing the two extra links does not change the motion of the thick-panel origami tube. The deployment process of two multi-layered tubes with planar-symmetric hexagonal cross-sections are shown in Fig. 5-16 in which the extra links between the concave eggbox-like vertexes are removed.

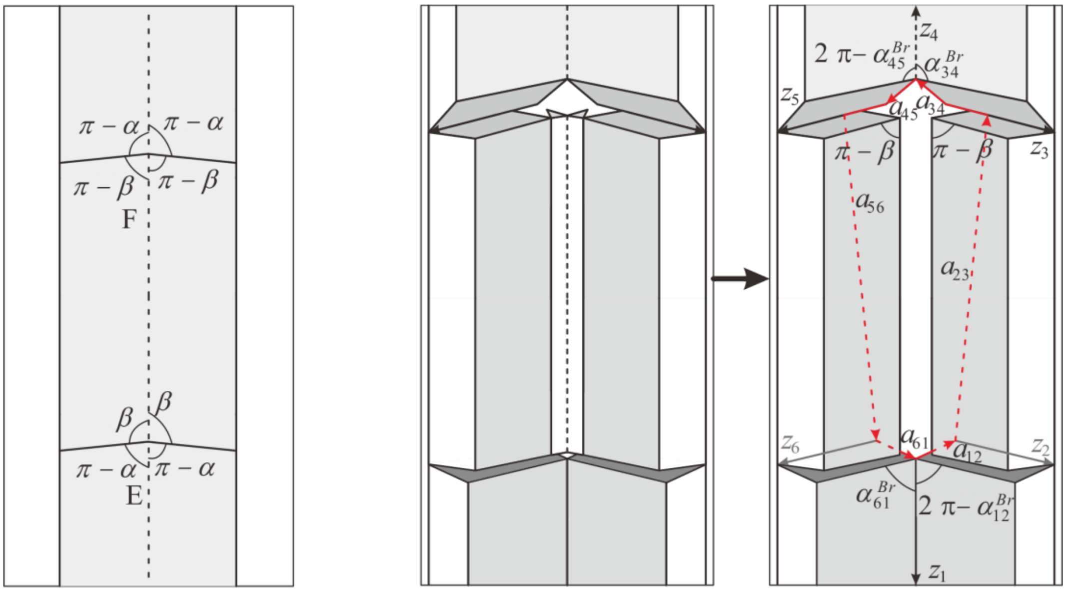

(a) (b)

Fig. 5-15 Construction of two connected concave eggbox-like vertexes: (a) zero-thickness form and (b) thick-panel form.

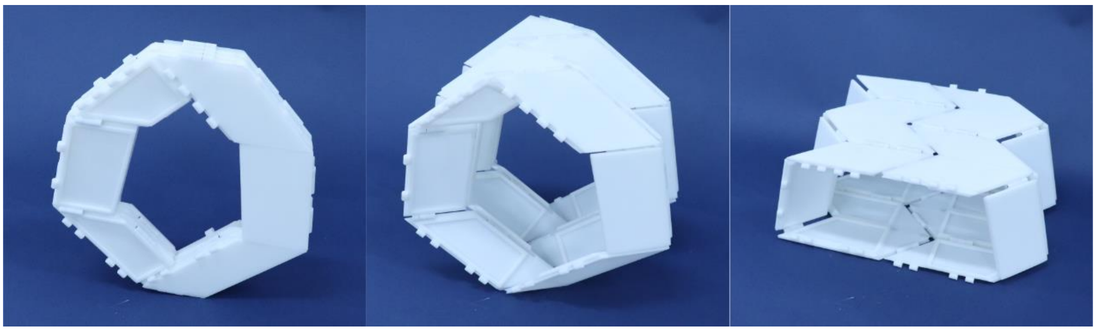

(a)

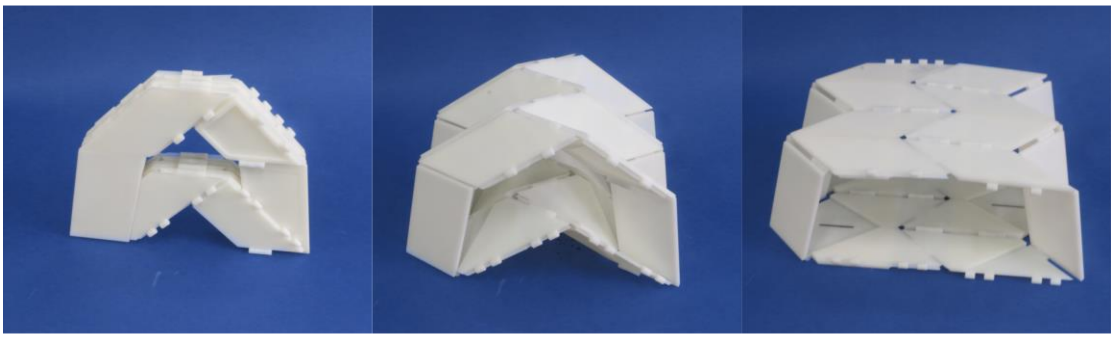

(b)

Fig. 5-16 Deployment process of multi-layered thick-panel origami tubes: (a) tube with convex cross-sections and (b) tube with concave cross-sections.

5.4.2 Curved tubes

The construction of a curved tube is described in Chapters 1 and 4. Curved tubes also have thick-panel forms. The construction of a curved tube is described in Chapters 1 and 4. It can be inferred that a curved tube also has Miura-ori vertexes, eggbox-like vertexes and Miura-like vertexes, and the method described in this chapter can be used to construct the thick-panel forms of these vertexes. If a curved tube with hexagonal cross-sections has two identical Miura-ori vertexes, it can be changed to a thick-panel form.

Figure 5-17 illustrates a curved tube with convex line-symmetric hexagonal cross-sections and the assignment of its sector angles and mountain-valley crease lines. Vertexes A and D are identical Miura-ori vertexes, vertexes B and C are convex eggbox-like vertexes and vertexes E and F are concave eggbox-like vertexes. The methods of constructing the thick-panel forms of vertexes A, B, C and D have been introduced in Chapters 5.2 and 5.3.

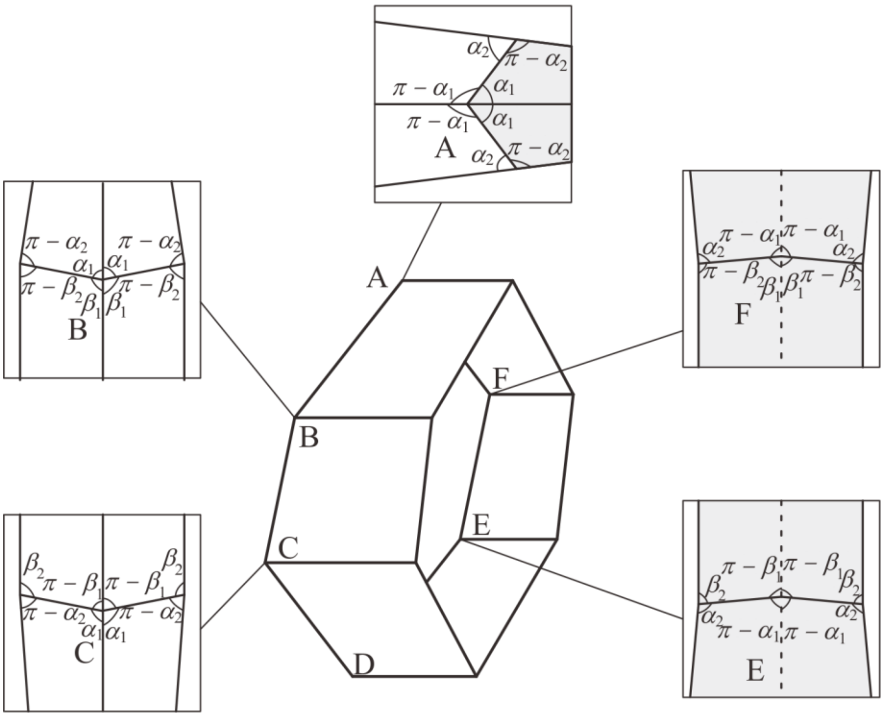

Fig. 5-17 Curved tube with convex line-symmetric hexagonal cross-sections, and the assignment of the sector angles and mountain-valley crease lines in different types of vertexes.

The zero-thickness form and thick-panel form of vertexes E and F are illustrated in Figs. 5-18(a) and (b). According to Chapter 5.4.1, the added links in the Bricard linkages of the thick-panel form can be removed, and vertexes E and F can be merged to one Bricard linkage in which the following equations are satisfied:

$$\begin{aligned} &a_{12} = a_{61} = \alpha_{34} = \alpha_{45} = 2a, \\ &\alpha_{23} = \alpha_{56} = L_{\mathrm{EF}} \cos(\pi - \beta), \end{aligned} \tag{5-34a}$$

$$\alpha_{61}^{Br} = 2\pi - \alpha_{12}^{Br} = \pi - \alpha,$$
$$\alpha_{56}^{Br} = 2\pi - \alpha_{23}^{Br} = 0, \tag{5-34b}$$
$$\alpha_{34}^{Br} = 2\pi - \alpha_{45}^{Br} = \pi - \alpha,$$

$$R_1 = R_4 = 0, R_3 = -R_5, R_2 = -R_6. \tag{5-34c}$$

where a is the link length in Bennett linkages A and D. Since the added links are removed, the angle β has an arbitrary value, and in Fig. 5-18, $\beta = \pi - \beta_2$. The deployment process of a multi-layered curved tube with line-symmetric cross-sections is shown in Fig. 5-19.

Figure 5-20 shows a curved tube with convex planar-symmetric hexagonal cross-sections and the assignment of its sector angles and mountain-valley crease lines. Vertexes A and D are identical Miura-ori vertexes, vertexes B and C are convex eggbox-like vertexes and vertexes E and F are concave eggbox-like vertexes. Similarly, the thick-panel forms of vertexes A to F can be obtained using the aforementioned method. Moreover, the deployment process of a multi-layered curved tube with planar-symmetric cross-sections is illustrated in Fig. 5-21.

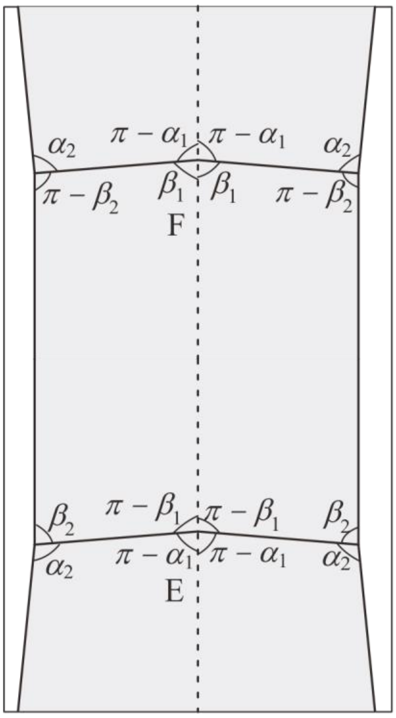

(a)

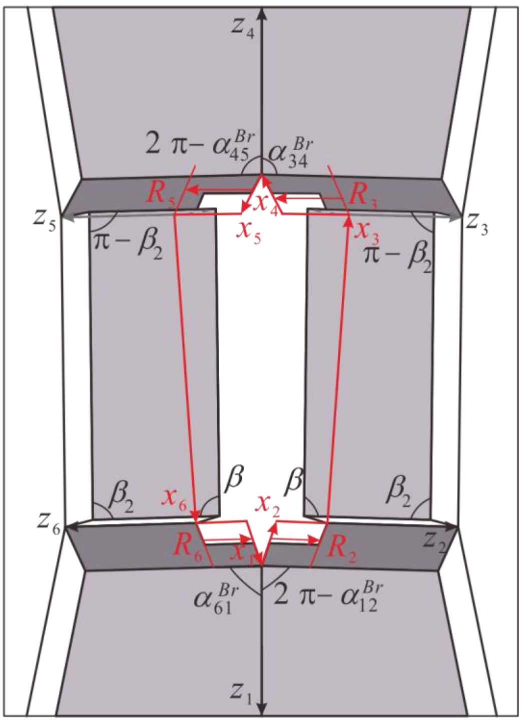

(b)

Fig. 5-18 Construction of two merged vertexes in a curved origami tube: (a) zero-thickness form and (b) thick-panel form.

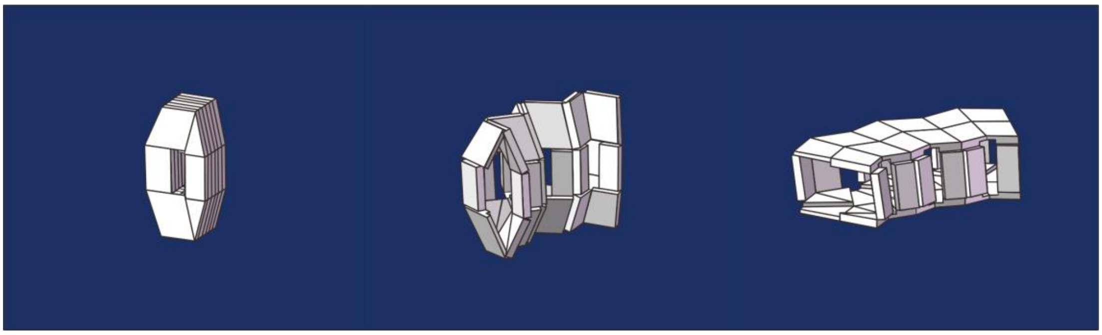

Fig. 5-19 Deployment process of a curved tube with line-symmetric cross-sections.

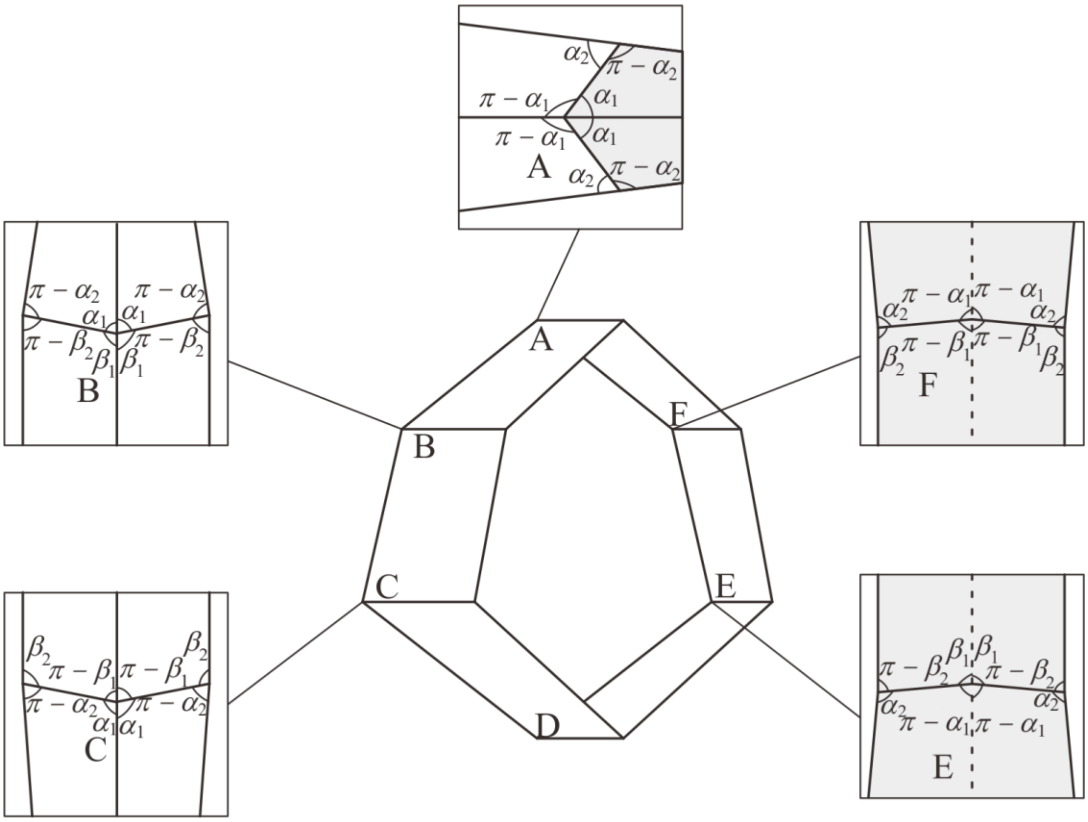

Fig. 5-20 Curved tube with convex planar-symmetric hexagonal cross-sections, and the assignment of sector angles and mountain-valley crease lines in different types of vertexes.

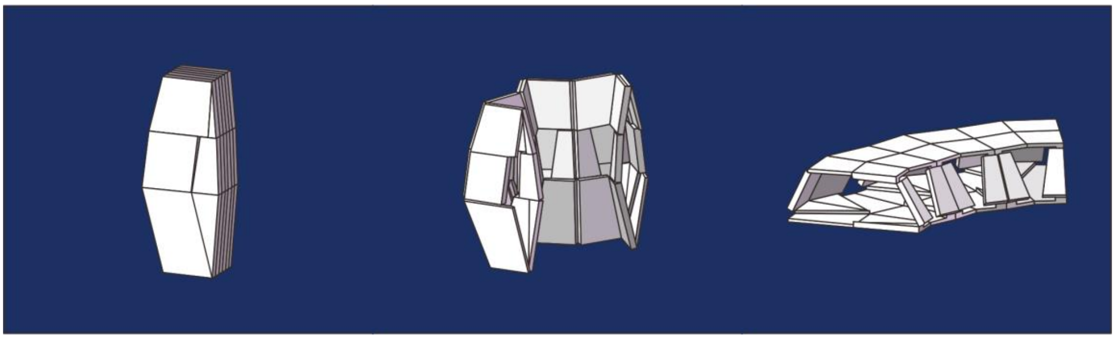

Fig. 5-21 Deployment process of a curved tube with planar-symmetric cross-sections.

5.5 Conclusions

This chapter describes the method of constructing a thick-panel origami tube with symmetric hexagonal cross-sections. The zero-thickness forms of these tubes are one-DOF and constructed using parallelogram facets. The thick-panel forms and zero-thickness forms of these origami tubes have equivalent motions. The vertexes of these tubes can be divided into four types, specifically, the Miura-ori vertexes, convex eggbox-vertexes, concave eggbox-like vertexes and Miura-like vertexes. The thick-panel form of origami tubes with line-symmetric and planar-symmetric cross-sections were examined. The linkages at each type of vertex were analysed. The tubes were repeated in the axial direction to form multi-layered tubes. The extra links between two concave eggbox-like vertexes could be removed to simplify the thick-panel tubes. Moreover, multi-layered curved thick-panel tubes were developed. These findings can help apply origami technology to deployable structures in which the thickness cannot be disregarded.

Chapter 6 Conclusions and future work

6.1 Conclusions

In this thesis, I examine networks of spherical linkages based on rigid origami and their applications. First, I assemble origami-inspired units in series and present a helical structure with switchable and hierarchical chirality. Next, the planar network of spherical linkages, known as a morphing surface, is introduced. Finally, an extended family of rigid origami tubes, pertaining to the spatial networks of spherical $4R$ linkages, is presented. Moreover, the method of constructing thick-panel origami tubes is examined. Kinematic theory is used to analyse the aforementioned networks. This chapter concludes the whole thesis:

(1) Helical structure with switchable and hierarchical chirality

First, a twisted chiral origami unit inspired by the famous eggbox pattern is constructed. Owing to different geometries, the origami unit can exhibit a different chirality. By connecting identical chiral units, I obtain homogeneous chiral structures; an achiral structure is obtained when the number of two different units is identical. In addition, I analyse the relationship between different design parameters according to the geometry of the chiral units. Next, I demonstrate that the chirality of single chiral structures can be tuned by adjusting the design parameters. Three different chiral structures with different design parameters are established, and their chirality is studied. To realize chirality switching, the chiral structure is regarded as a network of spherical 4R and planar 4R linkages, and the different chirality corresponds to different motion branches of the whole linkage network. This study represents the first attempt to realize chirality switching through mechanism bifurcation. Furthermore, I design hierarchically chiral structures with major and minor helices at the same macroscale in which the winding of the minor helix drives the unwinding of the major helix, resulting in two compact folding configurations. The proposed theory provides an opportunity to design multi-functional morphing structures in aerospace engineering applications. Moreover, due to their single degree-of-freedom characteristic, the proposed chiral structures can be applied to bionic robots with a simple control system.

(2) Morphing surfaces

First a one-DOF mobile assembly of spherical $4R$ linkages inspired by origami is presented and extended to a morphing surface, which is also one-DOF, by adding spherical $6R$ and $8R$ linkages. The morphing surface can transform through the motion of the spherical linkages. The shape of the above-mentioned morphing surface is determined by two shape-lines, and the shape of the morphing surface can be changed by tuning the two shape-lines. An example of the morphing surface that can transform from a parabolic cylinder to a paraboloid is presented, which may provide reference to develop flexible antennas in aerospace applications.

(3) Extended family of rigid origami tubes.

Inspired by Goldberg 5R and 6R linkages, I demonstrate that the existing origami tubes can be regarded as building blocks to construct new tubes. First, I conjoin several existing tubes by merging common sides or corners, thereby obtaining a family of tube with asymmetric polygonal cross-sections, namely, combined tubes. Next, I add transition parts to an existing tube, obtaining shifted tubes in which the crease lines between the neighbouring layers form nonplanar polygons. Using the kinematics theories of spherical 4*R* linkages, the combined tubes and shifted tubes are proved to be one-DOF. Finally, the formation of multi-layered and curved tubes based on the above-mentioned tubes is discussed.

(4) Thick-panel origami tubes

By replacing the spherical 4*R* linkages in the original zero-thickness origami tubes with spatial linkages such as Bennett and Bricard linkages, I establish a method to construct thick-panel origami tubes. The vertexes in zero-thickness origami tubes are divided into four types, namely, Miura-ori vertexes, convex eggbox-like vertexes, concave eggbox-like vertexes and Miura-like vertexes. For different types of vertexes, the thick-panel forms are different. In the thick-panel form of the vertexes, different kinds of spatial overconstrained linkages are used to replace the original spherical 4*R* linkages in the zero-thickness form. I present thick-panel origami tubes with line-symmetric and planar-symmetric hexagonal cross-sections, which can reproduce motions identical to those achievable using zero-thickness origami. Moreover, the characteristics of multi-layered tubes and curved tubes are discussed.

6.2 Future work

This dissertation systemically presents the theories of using the network of spherical linkages to construct deployable structures. To enhance the performance of the deployable structure, several potential research directions can be considered:

(1) First, origami techniques can be effectively applied to design chiral or hierarchical structures and metamaterials. In addition to the eggbox pattern, many other typical patterns exist, several of which demonstrate chiral behaviour during folding. Moreover, tessellation plays a key role in the construction of hierarchical structures. In general, a rigid pattern is preferred to reliably implement deformation, and a non-rigid pattern is used to achieve bistability. The present approach can likely be applied to origami units for different objectives, not limited to chirality.

(2) Second, the proposed approach of constructing combined and shifted tubes offers considerable flexibility to designers when fabricating rigidly foldable tubes to create metamaterials, origami robots, and other devices that require large shape variations. The rigid foldability of these tubes ensures that no facet distortion occurs during the shape change. I intend to identify more novel origami tubes in future research.

(3) Third, although the approaches of constructing thick-panel straight and curved tubes have been reported, methods to form thick-panel combined and shifted tubes have not been examined yet, and I intend to establish such methods in future work. The combined and shifted tubes are promising alternative options for designers when developing deployable structures; thus, it is necessary to obtain the thick-panel form of these two types of rigid origami tubes.

(4) Finally, I intend to establish a method of constructing thick-panel origami tubes with more complicated cross-sections, for example, octagonal cross-sections. In this thesis, the method of constructing origami tubes with hexagonal cross-sections was considered. Nevertheless, other rigid origami tubes with more complicated cross-sections exist, which can also be used in deployable structures. Consequently, it is desirable to derive the thick-panel forms of these tubes.

References

[1] 邓宗全. 空间折展机构设计 [M]. 哈尔滨：哈尔滨工业大学出版社, 2013.

[2] Gruber P, Häuplik S, et al. Deployable structures for a human lunar base [J]. Acta Astronautica, 2007, 61(1–6): 484-495

[3] Kiper G, Soylemez E. Deployable space structures [C]. International Conference on Recent Advances in Space Technologies. IEEE, 2009.

[4] Thrall A P, Quaglia C P. Accordion shelters: A historical review of origami-like deployable shelters developed by the US military [J]. Engineering structures, 2014, 59: 686-692

[5] Cai J, Deng X, Xu Y, et al. Geometry and motion analysis of origami-based deployable shelter structures [J]. Journal of Structural Engineering, 2015, 141(10):06015001

[6] Ma J, You Z. Energy absorption of thin-walled square tubes with a prefolded origami pattern—part I: geometry and numerical simulation [J]. Journal of Applied Mechanics, 2014, 81(1):1003.

[7] Zhang X, Cheng G, You Z, et al. Energy absorption of axially compressed thin-walled square tubes with patterns [J]. Steel Construction, 2007, 45(9):737-746.

[8] Chiang C H. On the classification of spherical four-bar linkages [J]. Mechanism & Machine Theory, 1984, 19(3):283-287.

[9] Tsai L W. Robot analysis: the mechanics of serial and parallel manipulators [M]. John Wiley & Sons, 1999.

[10] Chiang C H. Kinematics of spherical mechanisms [M]. Cambridge: Cambridge University Press, 1988.

[11] Gogu G. Structural synthesis of parallel robots [M]. Dordrecht: Springer, 2008.

[12] Dai J S. Geometrical foundations and screw algebra for mechanisms and robotics [M]. Beijing: Higher Education Press, ISBN: 9787040334838, 2014.

[13] Ball R S. A treatise on the theory of screws [M]. Cambridge: Cambridge University Press, 1900.

[14] Hunt K H. Kinematic geometry of mechanisms [M]. Clarendon Press, 1978.

[15] Hartenberg R S, Denavit J. Kinematic synthesis of linkages [M]. McGraw-Hill, 1964.

[16] Hawkins T. Emergence of the Theory of Lie Groups [M]. Berlin, New York: Springer-Verlag, 2000.

[17] Murray R M, Li Z X, Sastry S S. A Mathematical Introduction to Robotic Manipulation [M]. Boca Raton: CRC Press, 1994. Doctoral Dissertation of Tianjin University 120

[18] Hervé J M. The Lie group of rigid body displacements, a fundamental tool for mechanism design [J]. Mechanism and Machine Theory, 1999, 34(5): 719-730.

[19] Hegedüs G, Schicho J, Schröcker H-P. Bond Theory and Closed 5R Linkages [M]//Jadran Lenarcic M H. Latest Advances in Robot Kinematics. Springer. 2012: 221-228.

[20] Hegedüs G, Schicho J, Schröcker H-P. Construction of Overconstrained Linkages by Factorization of Rational Motions [M]//Lenarcic J, Husty M. Latest Advances in Robot Kinematics. Springer. 2012: 213-220.

[21] Hegedüs G, Schicho J, Schröcker H-P. The theory of bonds: A new method for the analysis of linkages [J]. Mechanism and Machine Theory, 2013, 70: 407-424.

[22] Nawratil G. Introducing the theory of bonds for Stewart Gough platforms with self-motions [J]. Journal of Mechanisms and Robotics, 2013, 6(1): 011004.

[23] Hegedüs G, Li Z, Schicho J, et al. The theory of bonds II: Closed 6R linkages with maximal genus [J]. Journal of Symbolic Computation, 2015, 68: 167-180.

[24] Chiang C H. Spherical kinematics in contrast to planar kinematics [J]. Mechanism and Machine Theory, 1992, 27(3):243-250.

[25] Schena B M. Center robotic arm with five-bar spherical linkage for endoscopic camera: JP20130253809.

[26] Schena B M. Robotic arm with five-bar spherical linkage: US20070623292.

[27] Mccarthy M. The design of spherical 4R linkages for four specified orientations [J]. Mechanism and Machine Theory, 1999.

[28] Burmester L, Lehrbuch der Kinematik. Verlag Von Arthur Felix, Leipzig, Germany, 1886.

[29] Michael J, McCarthy M, et al. Avoiding singular configurations in finite position synthesis of spherical 4R linkages [J]. Mechanism & Machine Theory, 2000, 35(3):451-462.

[30] Soh G S, Mccarthy M. Parametric design of a spherical eight-bar linkage based on a spherical parallel manipulator [J]. Journal of Mechanisms & Robotics, 2009, 1(1):212-240.

[31] Wei G, Dai J S. Origami-inspired integrated planar-spherical overconstrained mechanisms [J]. Journal of Mechanical Design, 2014, 136(5): 051003.

[32] Liu W, Chen Y. A double spherical 6R linkage with spatial crank-rocker characteristics inspired by kirigami [J]. Mechanism and Machine Theory, 2020, 153:103995.

[33] Bern M, Hayes B. The complexity of flat origami [C]. Proceedings of the seventh annual ACM-SIAM symposium on Discrete algorithms. Atlanta, Georgia, United States, Society for Industrial and Applied Mathematics, 1996, 175-183.

[34] Watanabe N, Kawaguchi K. The method for judging rigid foldability [C]. Origami 4, A K Peters/CRC Press, 2009, 165-174.

[35] Lang R J. Twists, tilings, and tessellations: mathematical methods for geometric origami [M]. Boca Raton: CRC Press, 2017.

[36] Onal C D, Wood R J, Rus D. Towards printable robotics: origami-inspired planar fabrication of three-dimensional mechanisms [C]. In Robotics and Automation (ICRA), 2011 IEEE International Conference on, pp. 4608-4613. May 9-13, 2011, Shanghai, China.

[37] Onal C D, Wood R J, Rus D. An origami-inspired approach to worm robots [J]. IEEE/ASME Transactions on Mechatronics, 2013, 18(2):430-438.

[38] Zirbel S A, Lang R J, Thomson M W. Accommodating thickness in origami-based deployable arrays [C]. In ASME 2013 international Design Engineering Technical Conferences and Computers and Information in Engineering Conference. 4-7 August 2013, Portland, Oregon, USA.

[39] Miyashita S, Onal C D, Rus D. Self-pop-up cylindrical structure by global heating [C]. In 2013 IEEE/RSJ International Conference on Intelligent Robots and Systems (IROS), pp. 4065-4071. 3-7 Nov 2013, Tokyo, Japan.

[40] Evans T A, Lang R J, Magleby S P, et al. Rigidly foldable origami gadgets and tessellations [J]. Royal Society Open Science, 2015, 2(9):150067.

[41] Huffman D A. Curvature and creases: a primer on paper [J]. IEEE Transactions on Computers, 1976, C-25(10):1010-1019.

[42] Miura K. Proposition of pseudo-cylindrical concave polyhedral shells [J]. Isas Report, 1969, 34:141-163.

[43] Barreto P T. Lines meeting on a surface: the 'Mars' paperfolding [C]. In Origami Science and Art: Proc. of the Second Int. Meeting of Origami Science and Scientific Origami, 29 November–2 December 1994, Otsu, Japan.

[44] Miura K. Method of packaging and deployment of large membranes in space [C]. Congress of International Astronautical Federation. 1980.

[45] Tachi T. Generalization of rigid foldable quadrilateral mesh origami [J]. Journal of the International Association for Shell & Spatial Structures, 2009, 50(3):173-179.

[46] Miura K. A Note on the Intrinsic Geometry of Origami [M]. I Research of Pattern Formation, KTK Scientific Publishers, 1989 Tokyo, Japan: 91-102

[47] Hull T C, Tachi T. Double-line rigid origami. arXiv, 2017 preprint arXiv:1709.03210.

[48] He Z, Guest S D. On Rigid Origami II: Quadrilateral Creased Papers. arXiv, 2018 preprint arXiv:1804.06483

[49] Wu W, You Z. A solution for folding rigid tall shopping bags [J]. Proceedings of the Royal Society A: Mathematical, Physical and Engineering Sciences, 2011, 467(2133):2561-2574.

[50] Cundy H M, Rollett A P. Mathematical Models [M]. Oxford University Press, New York, 2013.

[51] Dai J S, Jones J R. Mobility in metamorphic mechanisms of foldable/erectable kinds [J]. Journal of Mechanical Design, 1999, 121(3):375-382.

[52] Wei G, Dai J S. Geometry and kinematic analysis of an origami-evolved mechanism based on artmimetics [C] ASME/IFToMM International Conference on Reconfigurable Mechanisms and Robots ReMAR 2009. pp. 450-455.

[53] Zhang K, Dai J S. Classification of origami-enabled foldable linkages and emerging applications [C]. ASME 2013 International Design Engineering Technical Conferences and Computers and Information in Engineering Conference. 2013.

[54] Wei G, Dai J S. Origami-inspired integrated planar-spherical overconstrained mechanisms [J]. Journal of Mechanical Design, 2014, 136(5):258-265.

[55] Chen Y, You Z. Mobile assemblies based on the Bennett Linkage [J]. In Proceedings of the Royal Society of London A: Mathematical, Physical and Engineering Sciences, 2005, 461(2056), pp. 1229-1245. The Royal Society.

[56] Chen Y, You Z. On mobile assemblies of Bennett linkages [J]. In Proceedings of the Royal Society of London A: Mathematical, Physical and Engineering Sciences, 2008, 464(2093), pp. 1275-1293, The Royal Society.

[57] Liu S Y, Chen Y. Myard linkage and its mobile assemblies [J]. Mechanism and Machine Theory, 2009, 44(10):1950-1963.

[58] Wang K F, Chen Y. Rigid origami to fold a flat paper into a patterned cylinder [C]. Origami 5: Fifth International Meeting of Origami Science, Mathematics, and Education, Singapore, 2008.

[59] Liu S. Deployable structure associated with rigid origami and its mechanics [D]. School of Mechanical and Aerospace Engineering, Nanyang Technological University, Singapore, 2014.

[60] Gu Y, Chen Y. Origami cubes with one-DOF rigid and flat foldability [J]. International Journal of Solids and Structures, 2020 (207): 250-261.

[61] Kuribayashi K, Tsuchiya K, You Z, et al. Self-deployable origami stent grafts as a biomedical application of Ni-rich TiNi shape memory alloy foil [J]. Materials Science and Engineering: A, 2006.

[62] Guest S D, Pellegrino S. The folding of triangulated cylinders, part I: geometric considerations [J]. Journal of Applied Mechanics, 1994, 61(4):773.

[63] Nojima T. Modelling of folding patterns in flat membranes and cylinders by using origami [J]. 日本機械学会論文集. C 編, 2000, 66(643):p.354-360.

[64] Nojima T. Origami modeling of functional structures based on organic patterns [D]. Graduate School of Kyoto University, 336 Kyoto, Japan. 337, 2002.

[65] Connelly R, Sabitov I, Walz A. The bellows conjuncture [J]. Beitr. Algebra Geom., 1997, 38(1), pp. 1–10.

[66] Tachi T. One-DOF cylindrical deployable structures with rigid quadrilateral panels [C]. International Association for Shell and Spatial Structures (IASS) Symposium, Universidad Politecnica de Valencia, Spain, Sept. 28–Oct. 341 2, 2009, pp. 2295–2305.

[67] Tachi T. Freeform rigid-foldable structure using bidirectionally flat-foldable planar quadrilateral mesh [M]. Advances in Architectural Geometry 2010. Springer Vienna, 2010.

[68] Miura K, Tachi T. "Synthesis of rigid-foldable cylindrical polyhedra [M]. Symmetry: Art and Science, 2010, 204-213.

[69] Yasuda H, Yein T, Tachi T, et al. Folding behaviour of Tachi-Miura polyhedron bellows [J]. Proc Math Phys Eng, 2013, 469(2159):20130351.

[70] Liu S, Lv W, Chen Y, et al. Deployable prismatic structures with rigid origami patterns [J]. Journal of Mechanisms and Robotics, 2016.

[71] Schenk M, Guest S D. Geometry of miura-folded metamaterials [J]. Proceedings of the National Academy of Sciences, 2013, 110(9):3276-3281.

[72] Filipov E T, Tomohiro T, Paulino G H. Origami tubes assembled into stiff, yet reconfigurable structures and metamaterials [J]. Proceedings of the National Academy of Sciences of the United States of America, 2015, 112(40): pp. 12321–12326.

[73] Filipov E T, Paulino G H, Tachi T. Origami tubes with reconfigurable polygonal cross-sections [J]. Proc Math Phys Eng, 2016, 472(2185):20150607.

[74] Tachi T. Rigid-foldable thick origami [J]. Origami, 2011, 5: 253-264

[75] Edmondson B J, Lang R J, Magleby S P, Howell L L. An offset panel technique for thick rigidily foldable origami [C]. Proceedings of the ASME 2014 International Design Engineering Technical Conferences and Computers and Information in Engineering Conference, American Society of Mechanical Engineers, 2014: V05BT08A054

[76] Ku J S, Demaine E D. Folding flat crease patterns with thick materials [J]. Journal of Mechanisms and Robotics, 2016, 8(3): 031003.

[77] Hoberman C S. Reversibly expandable three-dimensional structure: US, US4780344 [P]. 1988.

[78] De Temmerman I, Mollaert M, Van Mele T, et al. Design and analysis of a foldable mobile shelter system [J]. International Journal of Space Structures, 2009, 22(3):161-168.

[79] Chen Y, Peng R, You Z. Origami of thick panels [J]. Science, 2015, 349(6246): 396-400.

[80] Peng R, Analysis of Mobile Network of Spherical 4R Linkages and Kinematics of Rigid Origami [D]. Tianjin University, 2016.

[81] Miura K. Method of packaging and deployment of large membranes in space [J]. Institute of Space & Astronautical Science Report, 1985, 618:1-9.

[82] Natori M C, Katsumata N, Yamakawa H, et al. Conceptual model study using origami for membrane space structures [C]. ASME 2013 International Design Engineering Technical Conferences and Computers and Information in Engineering Conference. 2013: V06BT07A047.

[83] Miura K. Triangles and quadrangles in space [C]. Proceedings of the 50th Symposium of the International Association for Shell and Spatial Structures, Valencia, 2009.

[84] Morgan J, Magleby S P, Howell L L. An approach to designing origami-adapted aerospace mechanisms [J]. Journal of Mechanical Design, 2016, 138(5): 052301.

[85] Debnath S, Fei L J. Origami theory and its applications: a literature review [J]. World Academy of Science, Engineering and Technology, 2013: 1131-1135.

[86] Zirbel S A, Lang R J, Thomson M W, et al. Accommodating thickness in origami-based deployable arrays [J]. Journal of Mechanical Design, 2013, 135(11): 111005.

[87] Felton S, Tolley M, Demaine E, et al. A method for building self-folding machines [J]. Science, 2014, 345(6197): 644-646.

[88] Miyashita S, Guitron S, Ludersdorfer M, et al. An untethered miniature origami robot that self-folds, walks, swims, and degrades [C]. International Conference on Robotics and Automation, 2015: 1490-1496.

[89] Zhang K, Fang Y, Fang H, et al. Geometry and constraint analysis of the three spherical kinematic chain based parallel mechanism [J]. Journal of Mechanisms and Robotics, 2010, 2(3): 031014.

[90] Onal C D, Wood R J, Rus D. An origami-inspired approach to worm robots [J]. IEEE/ASME Transactions on Mechatronics, 2013, 18(2): 430-438.

[91] Li S, Vogt D M, Rus D, et al. Fluid-driven origami-inspired artificial muscles [J]. Proceedings of the National Academy of Sciences of the United States of America, 2017, 114(50): 13132.

[92] Le P, Molina J, Hirai S. Application of Japanese origami ball for floating multirotor aerial robot [J]. World Academy of Science, Engineering and Technology, International Journal of Mechanical, Aerospace, Industrial, Mechatronic and Manufacturing Engineering, 2014, 8(10): 1747-1750.

[93] Lee D Y, Kim J S, Kim S R, et al. The deformable wheel robot using magic-ball origami structure [C]. ASME 2013 International Design Engineering Technical Conferences and Computers and Information in Engineering Conference. 2013: V06BT07A040.

[94] Wang Z, Jing L, Yao K, et al. Origami-based reconfigurable metamaterials for tunable chirality. Advanced Materials, 2017, 29(27), 1700412.

[95] Yasuda H, Tachi T, Lee M, et al. Origami-based tunable truss structures for non-volatile mechanical memory operation. Nature Communications, 2017, 8(1), 962.

[96] Frenzel T, Kadic M, Wegener M. Three-dimensional mechanical metamaterials with a twist. Science, 2017, 358(6366), 1072-1074.

[97] Schenk M, Guest S, Mcshane G. Novel stacked folded cores for blast-resistant sandwich beams [J]. International Journal of Solids and Structures, 2014, 51(25): 4196-4214.

[98] Silverberg J L, Evans A A, Mcleod L, et al. Using origami design principles to fold reprogrammable mechanical metamaterials [J]. Science, 2014, 345(6197): 647-650.

[99] Pratapa P P, Liu K, Paulino G H. Geometric mechanics of origami patterns exhibiting Poisson's ratio switch by breaking mountain and valley assignment [J]. Physical Review Letters, 2019, 122(15).

[100] Lv C, Krishnaraju D, Konjevod G, et al. Origami based mechanical metamaterials [J]. Scientific Reports, 2014, 4:5979.

[101] Cheung K C, Tachi T, Calisch S, et al. Origami interleaved tube cellular materials [J]. Smart Materials and Structures, 2014, 23(9): 094012.

[102] Filipov E T, Tachi T, Paulino G H. Origami tubes assembled into stiff, yet reconfigurable structures and metamaterials [J]. Proceedings of the National Academy of Sciences, 2015, 112(40): 12321-12326.

[103] Yasuda H, Yang J. Reentrant origami-based metamaterials with negative Poisson’s ratio and bistability [J]. Physical Review Letters, 2015, 114(18): 185502.

[104] Silverberg J L, Na J, Evans A A, et al. Origami structures with a critical transition to bistability arising from hidden degrees of freedom [J]. Nature Materials, 2015, 14(4): 389-393.

[105] Waitukaitis S, Menaut R, Chen B. G, et al. Origami multistability: From single vertices to metasheets [J]. Physical Review Letters, 2015, 114(5): 055503.

[106] Hanna B H, Lund J M, Lang R J, et al. Waterbomb base: a symmetric singlevertex bistable origami mechanism [J]. Smart Materials and Structures, 2014, 23(9): 094009.

[107] Reis P M, Jiménez F L, Marthelot J. Transforming architectures inspired by origami [J]. Proceedings of the National Academy of Sciences, 2015, 112(40): 12234-12235.

[108] Reis P M, Jiménez F L, Marthelot J. Transforming architectures inspired by origami [J]. Proceedings of the National Academy of Sciences, 2015, 112(40): 12234-12235.

[109] Felton S, Tolley M, Demaine E, Rus D, Wood R. A method for building selffolding machines [J]. Science, 2014, 345(6197): 644-646.

[110] Belke C H, Paik J. Mori: a modular origami robot [J]. IEEE/ASME Transactions on Mechatronics, 2017, 22(5): 2153-2164.

[111] Zhakypov Z, Belke C, Paik J. Tribot: A deployable, self-righting and multi-locomotive origami robot [C]. IEEE International Conference on Intelligent Robots and Systems (IROS), 2017.

[112] Kuribayashi K, Tsuchiya K, You Z, Tomus D, Umemoto M, Ito T, Sasaki M. Self-deployable origami stent grafts as a biomedical application of Ni-rich TiNi shape memory alloy foil [J]. Materials Science and Engineering: A, 2006, 419(1-2): 131-137.

[113] Miyashita S, Guitron S, Ludersdorfer M, Sung C R, Rus D. An untethered miniature origami robot that self-folds, walks, swims, and degrades [C]. Proceedings of the 2015 IEEE International Conference on Robotics and Automation (ICRA), 2015: 1490-1496.

[114] Miyashita S, Guitron S, Yoshida K, Li S, Damian D D, Rus D. Ingestible, controllable, and degradable origami robot for patching stomach wounds [C]. Proceedings of the 2016 IEEE International Conference on Robotics and Automation (ICRA), 2016: 909-916.

[115] Guitron S, Guha A, Li S, Rus D. Autonomous locomotion of a miniature, untethered origami robot using hall effect sensor-based magnetic localization [C]. Proceedings of the 2017 IEEE International Conference on Robotics and Automation (ICRA), 2017: 4807-4813.

[116] Salerno M, Zhang K, Menciassi A, Dai J S. A novel 4-DOF origami grasper with an SMA-actuation system for minimally invasive surgery [J]. IEEE Transactions on Robotics, 2016, 32(3): 484-498.

[117] Johnson M, Chen Y, Hovet S, Xu S, Wood B, Ren H, Tokuda J, Tse Z T H. Fabricating biomedical origami: a state-of-the-art review [J]. International Journal of Computer Assisted Radiology and Surgery, 2017, 12(11): 2023-2032.

[118] Zhang K, Fang Y, Fang H, Dai J S. Geometry and constraint analysis of the three-spherical kinematic chain based parallel mechanism [J]. Journal of Mechanisms and Robotics, 2010, 2(3): 031014.

[119] Zhang K, Dai J S. Reconfiguration of the plane-symmetric double-spherical 6R linkage with bifurcation and trifurcation [J]. Proceedings of the Institution of Mechanical Engineers, Part C: Journal of Mechanical Engineering Science, 2016, 230(3): 473-482.

[120] Feng H. Kinematics of spatial linkages and its applications to rigid origami [D]. Clermont Auvergne, 2018.

[121] Ionescu T G. Terminology for mechanisms and machine science [J]. Mechanism and Machine Theory, 2003, 38(7-10): 597-1112.

[122] Dai J S, Huang Z, Lipkin H. Mobility of overconstrained parallel mechanisms [J]. Journal of Mechanical Design, 2006, 128(1): 220-229.

[123] Chen Y, Baker J. Using a Bennett linkage as a connector between other Bennett loops [J]. Proceedings of the Institution of Mechanical Engineers, Part K: Journal of Multi-body Dynamics, 2005, 219(2): 177-185.

[124] Chen Y. Design of structural mechanisms [D]. Oxford University, UK, 2003.

[125] Yang F F, Li J M, Chen Y, et al. A deployable Bennett network in saddle surface [C]. Proceedings of the 14th IFToMM World Congress, Taiwan: IFToMM, 2015: 428-434.

[126] Kiper G, Söylemez E. Regular polygonal and regular spherical polyhedral linkages comprising Bennett loops [M]//Kecskem T A, M L A. Computational Kinematics. Berlin: Springer, 2009: 249-256.

[127] Goldberg M. New five-bar and six-bar linkages in three dimensions [J]. Transactions of the ASME, 1943, 65: 649-663.

[128] Myard F E. Contribution à la géométrie des systèmes articulés [J]. Bulletin de la Société Mathématique de France, 1931, 59: 183-210.

[129] Baker J E. The Bennett, Goldberg and Myard linkages—in perspective [J]. Mechanism and Machine Theory, 1979, 14(4): 239-253.

[130] Liu S Y, Chen Y. Myard linkage and its mobile assemblies [J]. Mechanism and Machine Theory, 2009, 44(10): 1950-1963.

[131] Qi X Z, Deng Z Q, Ma B Y, et al. Design of large deployable networks constructed by Myard linkages [J]. Key Engineering Materials, 2011, 486: 291-296.

[132] Sarrus P T. Note sur la transformation des mouvements rectilignes alternatifs, en mouvements circulaires, et reciproquement [J]. Académie des Sciences, 1853, 36, 1036-1038

[133] Bennett G T. The parallel motion of sarrut and some allied mechanisms [J]. Science, 1905, 9: 803-810.

[134] Dai J S, Li D, Zhang Q, et al. Mobility analysis of a complex structured ball based on mechanism decomposition and equivalent screw system analysis[J]. Mechanism & Machine Theory, 2004, 39(4):445-458.

[135] Lu S, Zlatanov D, Ding X, et al. Novel deployable mechanisms with decoupled degrees-of-freedom [J]. Journal of Mechanisms & Robotics, 2016, 8(2):021008.

[136] Caro S, Moroz G, Gayral T, Chablat D, Chen C. Singularity analysis of a six DOF parallel manipulator using Grassmann-Cayley algebra and Gröebner bases [C]. Brain, Body and Machine, Springer, Berlin, Heidelberg, 2010: 341-352.

[137] Song C Y, Chen Y, Chen I M. A 6R linkage reconfigurable between the linesymmetric Bricard linkage and the Bennett linkage [J]. Mechanism and Machine Theory, 2013, 70: 278-292.

[138] Wang Y X, Wang Y M. Configuration bifurcations analysis of six DOF symmetrical Stewart parallel mechanisms [J]. Journal of Mechanical Design, 2005, 127(1): 70-77.

[139] Bricard R. Leçons de cinématique [M]. Gauthier-Villars, 1926.

[140] Lee C C. On the generation synthesis of movable octahedral 6R mechanisms [C]. ASME Design Engineering Technical Conferences and Computers in Engineering Conference, Irvine, CA, 1996: 18-22.

[141] Chai W H, Chen Y. The line-symmetric octahedral Bricard linkage and its structural closure [J]. Mechanism and Machine Theory, 2010, 45(5): 772-779.

[142] Baker J E. On Bricard's doubly collapsible octahedron and its planar, spherical and skew counterparts [J]. Journal of the Franklin Institute, 1995, 332(6): 657-679.

[143] Wohlhart K. The two types of the orthogonal Bricard linkage [J]. Mechanism and Machine Theory, 1993, 28(6): 809-817.

[144] Baker J E, Wohlhart K. On the single screw reciprocal to the general linesymmetric six-screw linkage [J]. Mechanism and Machine Theory, 1994, 29(1): 169-175.

[145] Baker J E. The single screw reciprocal to the general plane-symmetric six-screw linkage [J]. Journal for Geometry Graphics, 1997, 1(1): 5-12.

[146] Li Z, Schicho J. A technique for deriving equational conditions on the DenavitHartenberg parameters of 6R linkages that are necessary for movability [J]. Mechanism and Machine Theory, 2015, 94: 1-8.

[147] Deng Z, Huang H, Li B, Liu R. Synthesis of deployable/foldable single loop mechanisms with revolute joints [J]. Journal of Mechanisms and Robotics, 2011, 3(3): 031006.

[148] You Z, Chen Y. Motion structures: deployable structural assemblies of mechanisms [M]. New York: Spon Press, 2014.

[149] Huang H, Deng Z, Li B. Mobile assemblies of large deployable mechanisms [J]. Journal of Space Engineering, 2012, 5(1): 1-14..

[150] Baker J E. Displacement-closure equations of the unspecialised doubleHooke's-joint linkage [J]. Mechanism and Machine Theory, 2002, 37(10): 1127- 1144.

[151] Lough W J, Wainer I W. Chirality in Natural and Applied Science [M]. Blackwell Science, Oxford, 2002.

[152] Lan X, Liu T, Wang Z, et al. DNA-guided plasmonic helix with switchable chirality [J]. Journal of the American Chemical Society, 2018, 140(37), 11763-11770.

[153] Murata K, Aoki M, Suzuki T, et al. Novel helical aggregation modes as detected by circular dichroism and electron microscopic observation [J]. Journal of the American Chemical Society, 1994, 116(15), 6664-6676.

[154] Jong J, Lucas N, Kellogg M, et al. Reversible optical transcription of supramolecular chirality into molecular chirality [J]. Science, 2004, 304(5668), 278-281.

[155] Suda M, Thathong Y, Promarak V, et al. Light-driven molecular switch for reconfigurable spin filters [J]. Nature communications, 2019, 10(1), 2455.

[156] Coombs D, Huber G, Kessler O, et al. Periodic chirality transformations propagating on bacterial flagella [J]. Physical Review Letters, 2002, 89(11), 118102.

[157] Zhao Z, Zhao H, Wang J, et al. Mechanical properties of carbon nanotube ropes with hierarchical helical structures [J]. Journal of the Mechanics and Physics of Solids, 2014, 71, 64-83.

[158] Pokroy B, Kang S, Mahadevan L, et al [J]. Self-organization of a mesoscale bristle into ordered, hierarchical helical assemblies. Science, 2009, 323(5911), 237-240.

中文大摘要

可展结构可以从小尺寸收拢状态展开为大尺寸工作状态。其小尺寸收拢状态为运输和存储提供了便利，大尺寸的工作状态又能保证该结构实现其所需的功能，因此被广泛应用于航空航天（天线、太阳能板等）、建筑（简易临时居所）、医疗（血管支架）以及材料科学（吸能结构）等领域，是近年来的热门研究课题。

球面机构由若干个转动副以及相同数目的杆件组成，其转动副轴线相交于一点。球面机构构成的网格由于具有折展比较大，自由度较少等特点，具有构建可展结构的潜在条件，但是由于球面机构网格一般为过约束系统，在对其参数进行设计时需要进行复杂的计算，因此如何得到基于球面机构的可动网格的设计方法一直是一项挑战。

折纸作为一种传统艺术，融合了数学、建筑、计算机科学、机构学等不同学科的相关理论，刚性折纸作为一种特殊的折纸类型，其变形只产生在折痕处，可视为球面机构的装配体，其中的折痕可以等同于机构的铰链，面板等同于机构的连杆，而多条折痕相交于一点的折纸图案可以看作是一个球面机构，相应地，具有多个顶点的图案可以看做是球面机构的网格。因此，刚性折纸理论为球面机构网格的设计提供了相关理论基础。

刚性折纸可被应用于许多领域。手性对生物的生理特性和药理作用有重要影响，对于手性结构的研究是生物和化学领域研究的新趋势。此外，研究表明不同手性对材料的机械、光学以及电磁特性有着十分重要的影响，因此手性结构对于电磁、光学等超材料的设计和制作有十分重要的参考价值。然而，在人造结构中实现同种材料的可切换和分层手性仍然是一个挑战，折纸技术为手性超材料的设计提供了启发；刚性折纸图案可视为球面机构的装配体，如果将刚性折纸中的平面单元变为其他形式，可以得到新的二维球面机构网格；可折叠管状结构具有大的折展比，展开以及折叠过程简单，对于可展结构的研究具有重要的意义，基于刚性折纸的管状结构具有自由度较少，折展过程容易控制的特点，且在折叠展开过程中其平面单元不会发生塑性变形，可以重复使用，因此在工程领域有广泛的应用；在实际工程应用中，折纸结构材料的厚度在很多情况下无法被忽略，而在材料具有厚度时，采用球面四杆机构构建厚板折纸结构会产生严重的运动干涉，这促使了人们进行厚板折纸技术的研究。

本文基于现代折纸理论，系统地探讨了构建基于球面机构的一维、二维、及三维可动网格的方法，通过分析球面机构网格的运动协调条件，设计了可切换手性的层级螺旋结构、可变形曲面、以及提出了一类新的刚性折纸管状结构以及折纸管状结构的厚板折叠方案。本文的主要内容如下：

本文第一章总结了国内外研究人员的相关科研成果。主要包括机构学基础理论、刚性折纸及其相关理论以及空间过约束机构和其组成的可展结构等内容。

本文第二章基于刚性折纸图案，得到了一维球面机构可动网格：一种可变手性以及具有层级手性的新型螺旋结构。首先，受折纸图案 eggbox 的启发，得到了两种手性折纸单元，根据手性的不同，可以分为左手性单元和右手性单元，并且通过几何计算，得到了该折叠单元各几何参数之间的关系。将上述手性折叠单元通过平面四杆机构进行串联，可以得到不同的结构：通过连接具有相同手性的折叠单元，可以得到左手手性或者右手手性螺旋结构；通过连接不同手性的折纸单元，将会得到非手性螺旋结构，通过连接上述螺旋结构中手性折叠单元的对应点，可以得到一条螺旋线。

其次，进一步研究了手性折叠单元的边长 a、eggbox 折痕间夹角 α 、折纸单元扭角 γ 、折纸单元高度 h 以及折纸单元二面角 ϕ 等几何参数对整个螺旋结构手性的影响。通过几何计算发现，当结构的螺旋角相同时，夹角 α 的值越大，拼接成一个螺旋周期所需的折纸单元数越少；当扭角 γ 一定时，夹角 α 的值越大，得到的螺旋结构整体高度越高，因此，可以通过改变手性折叠单元的几何参数来对螺旋结构的手性进行调节，并且通过实验对上述计算结果进行了验证。

然后，通过机构的运动分叉，实现了上述螺旋结构手性的改变。对于折纸手性折叠单元来说，其运动过程中，某一时刻不同的表面之间会发生物理干涉，从而使得该单元无法继续运动。根据机构学相关理论，在构成螺旋结构的折叠单元中，可以用杆件结构替换折纸结构，从而得到由杆件构成的折叠单元，通过合理设计不同杆件的几何形状，可以避免其在运动过程中的物理干涉，当杆件构成的手性折叠单元运动到原折纸单元发生物理干涉的位置时，可以继续运动，通过机构运动分叉，实现螺旋结构手性的改变。

最后，通过改变手性折叠单元之间的连接方式，得到了具有层级手性的螺旋结构。将连接手性折纸单元的平面四杆机构变为球面四杆机构，可以得到层级手性结构。通过连接该结构中折叠单元的对应点，可以得到主次两条螺旋线，通过计算这两条螺旋线螺旋角、螺距、长度、螺旋半径等几何参数，发现主次两条螺旋线的手性相同，螺旋趋势相反，当次螺旋线螺旋程度最大时，主螺旋线处于解螺旋——即直线状态，这一特性使得层级手性结构具有两个零长度状态。本章的研究为航空航天工程中可变形功能性结构的设计提供了新思路;且由于得到的手性结构具有单自由度，因此可以应用于系统简单的仿生机器人的控制。

本文第三章介绍了球面机构的二维可动网格：一种基于 eggbox 折纸图案的变形曲面。首先，受 eggbox 折纸图案启发，得到了一种新的基于球面四杆机构的可动网格。将上述折纸图案中的平行四边形平面单元沿着一条对角线折叠，可

以得到一个空间四边形，将两个相同的空间四边形进行拼接，得到了一种四面体单元，根据原先的 eggbox 折纸图案中平面单元之间的连接方式，对上述四面体单元进行装配，得到了一种新的可动网格，该网格由球面四杆机构组成，因此只具有一个自由度。

然后，通过向上述球面四杆机构网格中添加平面三角形单元，可以得到一种可变形曲面。添加上述平面三角形单元后，原本球面四杆机构构成的网格变为由球面四杆机构、球面六杆机构以及球面八杆机构共同构成的网格。通过对变形曲面中不同类型的顶点进行机构运动学分析，得到了这些顶点对应的球面机构中相关参数的运动学关系。根据上述关系，通过建立变形曲面的运动传递路径，得到了其运动学输入输出关系，计算表明尽管球面六杆和八杆机构具有多个自由度，变形曲面中不同球面机构间的特殊连接方式使得整个网格只具有一个自由度。

最后，实现了上述变形曲面在给定的抛物面和抛物柱面之间的变形。对于由三角形平面单元构成的变形曲面具有两条形状线，分别为竖直形状线和水平形状线，这两条形状线可以拟合两条曲线，变形曲面的形状可以由这两条曲线决定。因此对变形曲面形状的分析可以简化为对两条形状曲线的分析。由于目标曲面具有二重对称的特性，因此使用六种不同的等腰三角形单元构造变形曲面，从而使其也具有二重对称的特性。根据变形曲面的二重对称性，只需对该曲面的四分之一进行分析。通过在四分之一个变形曲面的两条形状线上建立坐标系，得到了形状线上顶点的坐标。抛物面可以由一条抛物线旋转而成，这条抛物线可以决定抛物面的形状，而抛物柱面可以由一条抛物线沿着一条直线平移而成，该抛物线和直线可以决定一个抛物柱面的形状。在变形曲面的运动过程中，如果某时刻两条形状线与抛物面中的抛物线吻合，而另一时刻分别与抛物柱面中的抛物线和直线相吻合，该变形曲面就可以由抛物面变形为抛物柱面。通过 Matlab 软件对上述过程进行了计算并给出了具体算例。本章研究为设计可变形结构，如可变形天线等提供了理论基础。

本文第四章探究了球面机构的三维可动网格，提出了两种新的刚性折纸管状结构。本章中，提出了两种横截面为非对称规则多边形的刚性折纸管状结构。首先，受 Goldberg 五杆以及六杆机构的启发，通过将已有的刚性折纸管状结构进行拼接，可以得到结合型管状结构。根据上述方法，结合型管状结构具有两种不同的拼接方式：第一种是管状结构之间的“加法”，该方法通过拼接两个管状结构的一条边，然后再去除公共部分，得到的结合型管状结构的横截面为原先两个管状结构横截面之“和”；另一种方法是管状结构之间的“减法”，通过拼接两个管状结构的两条边和一个内角，或者仅拼接两个管状结构的一条边，然后去除二者之间的公共部分，得到的结合型管状结构的横截面为原先两个管状结构横截面的“差”。当满足特定几何条件时，可以得到横截面为奇数边多边形的结合型管

状结构。上述管状结构的“加减运算”可以在三个或三个以上管状结构中进行。通过机构运动学分析，发现结合型管状结构依然具有一个自由度。

然后，通过向已有的管状结构中加入新平面单元，也可以得到错位型管状结构。机构运动学计算表明，向已有的管状结构中加入全等的平行四边形单元，即可得到具有单自由度的错位型折纸管状结构。上述平行四边形单元可以添加在同一管状结构的不同位置，从而得到不同的错位型管状结构。错位型管状结构的横截面可以为空间多边形或者平面多边形。

最后，对两种管状结构进行了更进一步的讨论：通过将相同的单层管状结构沿轴向重复排列，可以得到多层管状结构；通过将弯曲管状结构进行拼接并去除公共部分，可以得到弯曲结合型管状结构。本章内容丰富了刚性折纸管状结构的研究，为其应用进一步提供了理论基础。

本文的第五章提出了构造截面为对称六边形的厚板折纸管状结构的方法。本章研究的管状结构由四折痕顶点构成，根据已有的研究成果，发现可以通过使用 Bennett 机构替换球面四杆机构的方式构造四折痕顶点构成的厚板折纸结构。但是，上述方法不适用于四折痕顶点中四个扇形角不相等且四角之和不等于 360 度的情况，且目前研究人员只得到了构建截面为平行四边形的厚板折纸管状结构的方法。本章研究旨在探究构造厚板折纸管状结构的普适性方法。

首先，提出了构造截面为线对称六边形的厚板折纸管状结构的方法。对于截面为凸六边形的单层折纸管状结构，根据扇形角的不同，其顶点可以分为三类：分别为 Miura-ori 顶点、凸 eggbox-like 顶点以及凹 eggbox-like 顶点。在 Miura-ori 顶点处，将原先零厚度折纸中的球面四杆机构替换为 Bennett 机构；在凸 eggbox-like 顶点处，依然使用球面四杆机构构建其厚板折纸形式；在凹 eggbox-like 顶点处，由于使用球面四杆机构会导致运动干涉，且其扇形角之和不是 360 度，因此通过在其一条谷线折痕处添加两个额外杆件的方法构造其厚板折纸形式。通过对上述顶点的厚板折纸形式进行机构运动分析，发现其与对应的零厚度折纸形式的运动是等价的，因此，通过上述方法构建的截面为线对称凸六边形的厚板折纸管状结构的运动与其零厚度折纸形式等价。

在截面为线对称凹六边形的管状结构中，除了上述三种顶点，还存在另一种 Miura-like 顶点。在该顶点处，通过添加两个额外杆件，以 Bricard 机构构建其厚板形式。Miura-like 顶点的厚板形式的运动与对应的零厚度折纸的运动等价。根据上述方法，可以将零厚度折纸形式中不同类型顶点处的球面四杆机构转换成厚板折纸形式中相应的机构，从而得到截面为线对称六边形的厚板折纸管状结构。

然后，探究了构造截面为面对称六边形的厚板折纸管状结构的方法。在这种管状结构中，顶点依然可以分为上文中提到的四类，根据对称原理，在一个面对称管状结构中，当且仅当其两个 Miura-ori 顶点相同时，该管状结构才能被转换

成厚板形式。通过与前文类似的方法，可以将截面为面对称六边形的管状结构转化成厚板形式。值得注意的是，由于 Miura-like 顶点一条折痕处添加了两个额外杆件，因此当凸 eggbox-like 顶点与之连接时，不能用球面四杆机构构造其厚板折纸形式，对于这种情况，采用 Bricard 机构构造其厚板折纸形式。

最后，对厚板折纸管状结构进行了进一步讨论。单层厚板折纸管状结构沿着轴向重复排列，可以得到多层厚板折纸结构。由于需要添加过多的杆件,为了便于加工，对厚板折纸管状结构进行了简化：当两个凹 eggbox-like 顶点进行连接时，其公共的两根额外杆件可以去除，由原来的两个 Bricard 机构变为一个 Bricard 机构，且运动形式不发生改变。另外通过与构造直管结构相同的方法，还可以得到弯管厚板折纸结构。

本章内容为刚性折纸管状结构的工程应用提供了理论基础。

本文的第六章对全文的内容进行了梳理和归纳并提出了未来的工作。

本文的研究在未来工作方面有以下内容：

（1） 本文提出了一种受 eggbox 折纸图案启发手性结构，这种将折纸图案与新结构结合的方法的应用不仅局限于手性结构中，未来会继续进行基于折纸图案的诸如双稳态结构、超材料等新型结构或者材料的研究。

（2） 本文中提出的构造复合型和转换型折纸管状结构的方法使得在设计折纸机器人、折纸超材料、以及其他可展结构时有更多的备选方案，未来将会继续进行折纸管状结构相关方面的研究。

（3） 本文中提到的厚板折纸管状结构并不包括结合型管状结构和转换型管状结构，构造这些管状结构的厚板结构依然有待发现

（4） 本文提出了构造截面为六边形的折纸管状结构的厚板形式的方法，对于如何得到截面为更加复杂多边形的管状结构，依然有待研究。

关键词：球面四杆机构，可展结构，刚性折纸，厚板折纸

Publications

Papers：

[1] Chen Y., Lv W. et al. An extended family of rigidly foldable origami tubes [J]. Journal of Mechanisms & Robotics, Transactions of the Asme, 2017, 9: 021002 （导师一作）

[2] Chen Y., Lv W., et al. Mobile assemblies of four-spherical-4R-integrated linkages and the associated four-crease-integrated rigid origami patterns [J]. Mechanism and Machine Theory, 2019, 142(12): 103613. （导师一作）

[3] Gattas J. M., Lv W. et al. Rigid-foldable tubular arches [J]. Engineering Structures, 2017, 145: 246-253

[4] Feng H., Lv W., Ma J., et al. Helical structures with switchable and hierarchical chirality [J]. Applied Physics Letters, 2020, 116(19):194102. （共同一作）

Acknowledgements

My deepest gratitude goes first and foremost to Prof. Yan Chen, my supervisor, for her constant encouragement and patient guidance throughout my PhD's study. Her constructive suggestions and valuable guidance towards my work and life have been the driving force to complete my research and life compass to realize my bright future. Furthermore, her patience and generosity with students, her enthusiasm and rigorous attitude with academic research, and her immense knowledge will continue to influence my future work and life.

I would also like to thank Prof. Jiayao Ma and Prof. Lin Yuan for their advices and help on my research, Prof. Zhong You, Prof. Rongjie Kang, Prof. Zhibin Song and Ms. Yunyan Wang for their kind help. Appreciation also goes to Miss Huijuan Feng, Mr. Fufu Yang, Mr. Xiao Zhang, Mr. Peng Liu, Mr. Yuanqing Gu, Mr. Mingyuan Yang, Mr. Rui Peng and Mr. Weiqi Liu. Discussions with them widen my vision and deepen my understanding of the research. Meanwhile, I would like to thank my colleagues in Motion Structure Laboratory.

Scholarship Fund by China Scholarship Council, the financial support by the National Natural Science Foundation of China (Projects 51575377, 51721003, 51825503, 51290293 and 51422506,), by the Ministry of Science and Technology of China (Project 2014DFA70710), and the University PhD Scholarship by Tianjin University are also gratefully acknowledged.

Finally, I would like to express my thanks to my parents, for their encouragement, support and confidence in me. All of them give me courage and belief to overcome any difficulty in my study and life.